

# From “Where” to “What”: Towards Human-Understandable Explanations through Concept Relevance Propagation

Reduan Achtibat<sup>1,\*</sup>      Maximilian Dreyer<sup>1,\*</sup>      Ilona Eisenbraun<sup>1</sup>  
 Sebastian Bosse<sup>1</sup>      Thomas Wiegand<sup>1,2,3</sup>      Wojciech Samek<sup>1,2,3,†</sup>  
 Sebastian Lapuschkin<sup>1,†</sup>

<sup>1</sup> Fraunhofer Heinrich-Hertz-Institute, 10587 Berlin, Germany

<sup>2</sup> Technische Universität Berlin, 10587 Berlin, Germany

<sup>3</sup> BIFOLD – Berlin Institute for the Foundations of Learning and Data, 10587 Berlin, Germany

\* contributed equally

† corresponding authors: {sebastian.lapuschkin,wojciech.samek}@hhi.fraunhofer.de

## Abstract

The emerging field of eXplainable Artificial Intelligence (XAI) aims to bring transparency to today’s powerful but opaque deep learning models. While local XAI methods explain individual predictions in form of attribution maps, thereby identifying *where* important features occur (but not providing information about what they represent), global explanation techniques visualize *what* concepts a model has generally learned to encode. Both types of methods thus only provide partial insights and leave the burden of interpreting the model’s reasoning to the user. Only few contemporary techniques aim at combining the principles behind both local and global XAI for obtaining more informative explanations. Those methods, however, are often limited to specific model architectures or impose additional requirements on training regimes or data and label availability, which renders the post-hoc application to arbitrarily pre-trained models practically impossible. In this work we introduce the Concept Relevance Propagation (CRP) approach, which combines the local and global perspectives of XAI and thus allows answering both the “where” and “what” questions for individual predictions, without additional constraints imposed. We further introduce the principle of Relevance Maximization for finding representative examples of encoded concepts based on their *usefulness* to the model. We thereby lift the dependency on the common practice of Activation Maximization and its limitations. We demonstrate the capabilities of our methods in various settings, showcasing that Concept Relevance Propagation and Relevance Maximization lead to more human interpretable explanations and provide deep insights into the model’s representations and reasoning through concept atlases, concept composition analyses, and quantitative investigations of concept subspaces and their role in fine-grained decision making.

## 1 Introduction

Considerable advances have been made in the field of Machine Learning (ML), with especially Deep Neural Networks (DNNs) [71] achieving impressive performances on a multitude of domains. Examples range from image classification [65, 32], perceptual assessment of images [22, 21] and the diagnosis of medical conditions [59, 4, 117], to understanding chemical many body systems [116, 139], playing video games on a competitive level [57, 136], predicting the weather [121, 51], the spread of infectious diseases [120, 8], or finding improved solutions in protein structure prediction [119].

On the one hand, the widespread success of DNNs in the sciences and the ample availability of public and proprietary data for training models drives the application of Machine Learning (ML) in the industries, such as in various aspects of augmented medical diagnoses [23, 49] or autonomous driving [73, 54]. Conversely, the desire for implementation in practical settings has highlighted a fundamental problem of highly complex and non-linear DNNs, which act as opaque black-boxes

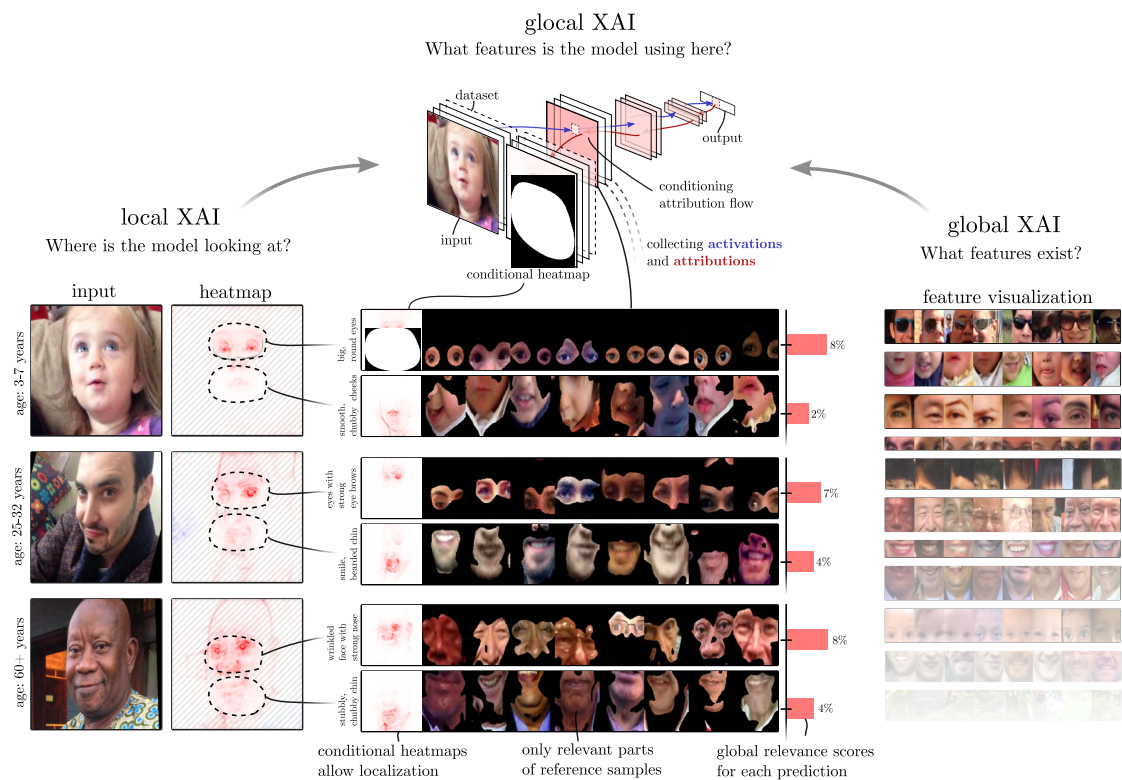


Figure 1: Glocal XAI can tell which features exist and how they are used for predictions by unifying local and global XAI. (*Left*): Local explanations visualize which input pixels are relevant for the prediction. Here, the model focuses on the eye region for all three predictions. However, what features in particular the model has recognized in those regions remains open for interpretation by the user. (*Right*): By finding reference images that maximally represent particular (groups of) neurons, global XAI methods give insight into the concepts generally encoded by the model. However, global methods alone do not inform which concepts are recognized, used and combined by the model in per-sample inference. (*Center*): Glocal XAI can identify the relevant neurons for a particular prediction (property of local XAI) and then visualize the concepts these neurons encode (property of global XAI). Further, by using concept-conditional explanations as a filter mask, the concepts' defining parts can be highlighted in the reference images, which largely increases interpretability and clarity. Here, the topmost sample has been predicted into age group (3-7) due to the sample's large irides and round eyes, while the middle sample is predicted as (25-32), as more of the sclera is visible and eyebrows are more apparent. For the bottom sample, the model has predicted class (60+) based on its recognition of heavy wrinkles around the eyes and on the eyelids, and pronounced tear sacs next to a large knobby nose.

during decision making [109, 112]: The reasoning behind their decisions is generally not obvious, and as such, they are simply not trustworthy enough, as their decisions may be (and often are) biased towards unintended or undesired features, as shown in, e.g., [127, 69, 114, 6]. This in turn hampers the transferability of ML models to many application domains of interest, e.g., due to the risks involved in high-stakes decision making [142, 109], or the requirements set in governmental regulatory frameworks [45, 131] and guidelines brought forward [31].

**eXplainable Artificial Intelligence** In order to alleviate this issue, the field of eXplainable Artificial Intelligence (XAI) has recently gained focus, which aims to open the black box of deep learning models in order to increase trust, verifiability and accountability in the context of Machine Learning. In fact, multitudes of XAI-methods have been developed that are able to visualize interpretable “explanations” of a model’s decision process, approaching the subject from different angles, e.g., based on gradients [86, 129], as modified backpropagation processes [11, 126, 122, 89], by probing the model’s reaction to changes in the input [147, 105] or visualizing stimuli specific neurons react strongly to [36, 94].

The field can roughly be divided into *local XAI* and *global XAI*. Methods from local XAI commonly compute attribution maps in input space, illuminating the input-output relationship of a prediction, given a model and a particular predicted-upon data sample. Visualizable attribution maps typically highlight input regions or features which carry some form of importance to the prediction process (i.e., with respect to a specific sample), depending on the particular XAI approach in use. Local attribution maps primarily work as markers for important or unimportant input regions and often are — without access to the corresponding data sample, and requiring a certain level of expert domain knowledge — of only limited informativity on their own, as Figure 1 illustrates.

Furthermore, attribution maps generated with local XAI approaches can generally be understood as a superposition of many different model-internal decision sub-processes (e.g., see [61]), working through different transformations of the same input features and culminating to the final prediction. Many intricacies are lost with local XAI approaches producing only a singular attribution map (visualization) in the input space per prediction outcome. The result might be unclear, imprecise or even ambiguous explanations. Assuming for example an image classification setting and an attribution map corresponding to the task, highlighting a particular image region, it might be clear *where* (in terms of input dimensions) important information can be found, but not *what* this information is, i.e., what characteristics of the raw input features the model has extracted and used during inference, or whether this information is a singular characteristic or a (locally) overlapping plurality thereof. This introduces many degrees of freedom to the interpretation of attribution maps generated by local XAI, rendering a precise understanding of the models’ *internal reasoning* a difficult task.

Global XAI on the other hand attempts to address the very issue of understanding the *what* question, i.e., which features or concepts have been learned by a model, or play an important role in a model’s reasoning in general. Some approaches from the domain of Feature Visualization, for example, synthesize example data in order to reveal the concept a particular neuron activates for [36, 130, 78, 87, 94], but do not inform which concept is used in a particular classification or how it can be linked to a particular output. From these approaches, we can at most obtain a global understanding of all possible features the model can use, but how these features interact with each other given some specific data sample, and how the model infers a decision cannot be understood. Other branches of global XAI propose methods, e.g., to test a model’s sensitivity to a priori known, expected or pre-categorized stimuli [60, 103, 15, 16]. These approaches however require labelled data, thus limiting, and standing in contrast to, the exploratory potential of local XAI.

Some recent works have begun to bridge the gap between local and global XAI by, for example, drawing weight-based graphs that show how features interact in a global, yet class-specific scale (which can be derived from labelled data), but without the capability to deliver explanations for individual data samples [53, 75]. Others plead for creating inherently explainable models in hope of replacing black box models [109]. These methods, however, either require specialized architectures, data and labels, or training regimes (or a combination thereof) [27, 28] and do not support the still widely used off-the-mill end-to-end trained DNN models with their extended explanation capabilities. An in-depth discussion of related work can be found in Appendix A.1.

In this work, we connect lines of local and global XAI research by introducing Concept Relevance Propagation (CRP), a next-generation XAI technique that explains individual predictions in terms of localized and human-understandable concepts. Other than the related state-of-the-art, CRP answers both the “where” and “what” questions, thereby providing deep insights into the model’s reasoning process. As a post-hoc XAI method, CRP can be applied to (almost) any ML model with no extra requirements on the data, model or training process. We demonstrate on multiple datasets, model architectures and application domains, that CRP-based analyses allow one to (1) gain insights into the representation and composition of concepts in the model as well as quantitatively investigate their role in prediction, (2) identify and counteract Clever Hans filters [69] focusing on spurious correlations in the data, and (3) analyze whole concept subspaces and their contributions to fine-grained decision making. Analogously to Activation Maximization [90], we also propose the Relevance Maximization (RelMax) approach, which uses CRP in order to search for the most relevant samples in the training dataset, and show its advantages when “explaining by example”. In summary, by lifting XAI to the concept level, CRP opens up a new way to analyze, debug and interact with a ML model, which can be particularly beneficial for safety-critical applications and ML-supported investigations in the sciences.

## 2 Methods

In our work we contribute technically by leveraging and extending the capabilities of the Layer-wise Relevance Propagation (LRP) framework [11]. After reiterating the general technical approach behind LRP in Section 2.1, we discuss and alleviate the method’s limitations with the introduction of Concept Relevance Propagation in Section 2.2. Section 2.3 follows with our propositions towards the understanding of latent representations themselves in extension to Section 2.2, including a brief overview of and comparisons to related approaches.

### 2.1 Layer-wise Relevance Propagation revisited

LRP [11] is a white-box attribution method grounded on the principles of flow conservation and proportional decomposition. Its application is aligned to the layered structure of machine learning models. Assuming a model with  $L$  layers

$$f(\mathbf{x}) = f_L \circ \dots \circ f_1(\mathbf{x}) , \quad (1)$$

LRP follows the flow of activations and pre-activations computed during the forward pass through the model in opposite direction, from the final layer  $f_L$  back to the input mapping  $f_1$ .

Let us consider some (internal) layer or mapping function  $f_*(\cdot)$  in the model. Within such a layer, LRP assumes the computation of pre-activations  $z_{ij}$ , mapping inputs  $i$  to outputs  $j$ , which are then aggregated as  $z_j$  at  $j$ , e.g., by summation. Commonly, in neural network architectures, such a computation is given with

$$z_{ij} = a_i w_{ij} \quad (2)$$

$$z_j = \sum_i z_{ij} \quad (3)$$

$$a_j = \sigma(z_j) , \quad (4)$$

where  $a_i$  are the input activations passed from the previous layer and  $w_{ij}$  are the layer’s learned weight parameters, mapping inputs  $i$  to layer outputs  $j$ . Note that the aggregation by summation to  $z_j$  can be generalized, e.g., to also support max-pooling by formulating the sum as a  $p$ -means pooling operation [11]. Finally,  $\sigma$  constitutes a (component-wise) non-linearity producing input activation for the succeeding layer(s).

In order to be able to perform its relevance backward pass, LRP assumes the relevance score of a layer output  $j$  as given as  $R_j$ . The algorithm usually starts by using any (singular) model output of interest as an initial relevance quantity. In its most basic form, the method then distributes the quantity  $R_j$  towards the neuron’s input as

$$R_{i \leftarrow j} = \frac{z_{ij}}{z_j} R_j , \quad (5)$$

i.e., proportionally wrt. the relative contribution of  $z_{ij}$  to  $z_j$ . Lower neuron relevance is obtained by simply aggregating all incoming relevance messages  $R_{i\leftarrow j}$  without loss:

$$R_i = \sum_j R_{i\leftarrow j} \quad (6)$$

This proportionality simultaneously ensures a conservation of relevance during decomposition as well as between adjacent layers, i.e.,

$$\sum_i R_i = \sum_i \sum_j R_{i\leftarrow j} = \sum_j \sum_i \frac{z_{ij}}{z_j} R_j = \sum_j R_j . \quad (7)$$

Note, that above formalism, at the scope of a layer, introduces the variables  $i$  and  $j$  as the inputs and outputs of the whole layer mapping, and assumes  $z_{ij} = 0$  for unconnected pairs of  $i$  and  $j$ , as it is the case in single applications of filters in, e.g., convolutional layers. For component-wise non-linearities  $\sigma$  in Equation (4), commonly implemented by, e.g., the tanh or ReLU functions which (by LRP) typically are treated as a separate layer instances, this results in  $z_{ij} = \delta_{ij} z_j$  (with  $\delta_{ij}$  being the Kronecker-Delta representing the input-output connectivity between all  $i$  and  $j$ ) and consequently in an identity backward pass through  $\sigma$ . This principle of attribution computation by relevance decomposition can be implemented and executed efficiently as a modification of gradient backpropagation [82], cf., e.g. [3, 5].

In order to ensure robust decompositions and thus stable heatmaps and explanations, several purposed LRP rules have been proposed in literature (see [82, 112] for an overview), for which Equations (5) and (6) serve as a conceptual basis. Recent works further recommend a composite strategy, mapping different rules to different parts of a neural network [82, 64, 112], which qualitatively and quantitatively improves attribution maps for the intent of explaining prediction outcomes. In the following analysis, different composite strategies are therefore used following recent recommendations from literature. See Appendix A.3 for the technical details regarding the computation of LRP attributions used in this work.

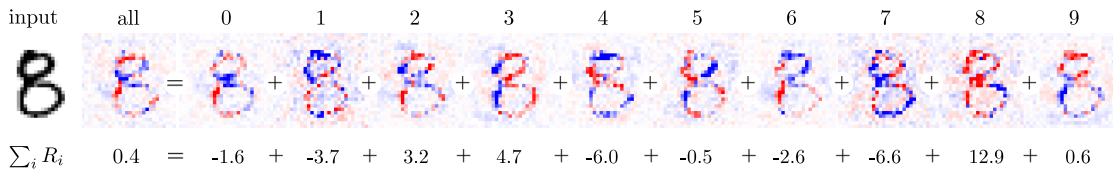
## 2.2 Disentangling Explanations with Concept Relevance Propagation

Layer-wise Relevance Propagation, like other backpropagation-based methods (e.g., [147, 126, 122]), computes attribution scores for all hidden units of a neural network model in order to allot a score to the model input. While in some recent works those hidden layer attribution scores have been used as a (not further semantically interpreted) means to improve deep models [81, 144, 128, 18], or as proxy representations of explanations for the identification of systematic Clever Hans behavior [6], they are usually disregarded as a “by-product” for obtaining per-sample explanations in input space. The reason is fairly simple: End-to-end learned representations of data in latent space are usually difficult (or impossible) to interpret, other than the samples in input space, e.g., images. Using attribution scores for rating the importance of individual yet undecipherable features and their activations does not provide any further insight about the model’s inference process. We further discuss this problem, and propose a solution to this un-interpretability of latent representations in Section 2.3.

Let us for now assume that we *do* have an understanding of the distinct roles of latent filters and neurons in end-to-end learned DNNs. Then, another problem emerges for interpreting model decisions in input space, rooted in the mathematics of modified backpropagation approaches. As Equation (7) summarizes for intermediate layers, LRP (and related approaches) propagates quantities from all layer outputs  $j$  simultaneously to all layer inputs  $i$ . This leads at a layer input to a weighted superposition of attribution maps received from all upper layer representations, where detailed information about the individual roles of interacting latent representations is lost. What remains is a coarse map identifying the (general) significance of an input feature (e.g., a pixel) to the preceding inference step.

A notable difference to this superimposing backpropagation procedure *within* the model is the initialization of the backpropagation process, where usually only one network output, of which the meaning (e.g., representation of categorical membership) generally *is* known, is selected for providing an initial relevance attribution quantity, and all others are masked by zeroes. This guarantees

**a** class-conditional heatmaps for more specific explanations



**b** limited explanatory value of traditional heatmaps

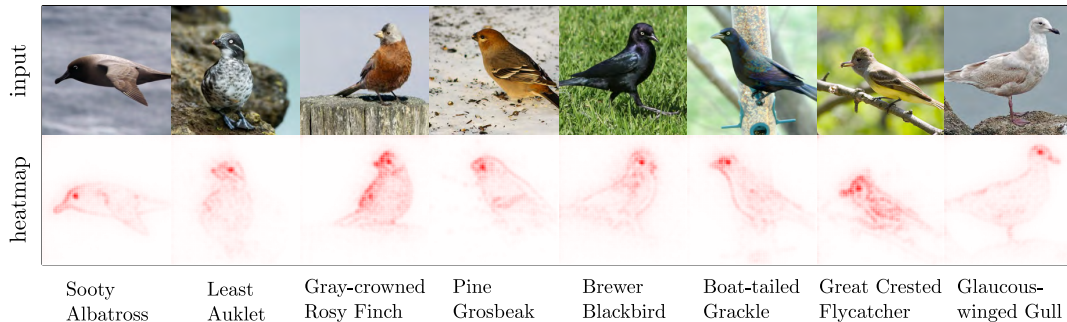


Figure 2: **a)** Class-conditional heatmap example for MNIST using LRP: Selecting *one* specific output class (see numbers above) for the heatmap calculation leads to explanations conveying precise meaning, namely *which features in their given state support (red) or contradict (blue) the class output*, compared to choosing *all* output classes at once, where, e.g., the meaning of the class-specific sign of the attribution is lost. For LRP, the heatmap computed for the whole output at once is a superposition of all class-specific heatmaps. A reference colormap for heatmaps shown in this paper is given in Appendix A.3.1. **b)** In some cases, traditional heatmaps can still be rather uninformative despite being class-specific, as is shown for bird species classification examples. Here, heatmaps only hint at the location of relevant body parts, without specifying the (different) concepts, such as e.g. species-specific beak shapes, being recognized and considered by the model.

that an explanation heatmap represents the significance of (input) features to only the model output of choice. Let us call this heatmap representation a *class- or output-conditional* relevance map  $R(\mathbf{x}|y)$  specific to a network output  $y$  and a given sample  $\mathbf{x}$ . Would one backpropagate all network outputs simultaneously, as it is demonstrated in Figure 2 (a), class-specificity would be lost, and again only information about “some” not further specified feature importance could be obtainable. Still, even class-specific attribution maps can be uninformative, as shown in Figure 2 (b). Here, attributions tend to mark the same body parts for all bird species, as a result of attribution scores specific to latent concepts superposed in input space. In all explanations, we see that the, e.g. the bird’s head seems to be of importance. We do not know, however, whether the animal’s eyes or beak carry some individual characteristic recognized and utilized by the model.

In the following, we propose strategies for disentangling attribution scores for latent representations, in order to increase the semantic fidelity of explaining heatmaps via Concept Relevance Propagation. We introduced the notion of a class- or output-conditional relevance quantity  $R(\mathbf{x}|y)$  for describing the use of knowledge about the meaning of particular neural network neurons and filters and their represented concepts — here the categories represented by the neurons at the model output. The key idea for obtaining  $R(\mathbf{x}|y)$  is the masking of unwanted network outputs  $-y$  prior to the backpropagation process via a multiplication with zeroes: Perpetuating the notation introduced in the previous Section 2.1, obtaining the attribution scores  $R_i^1(\mathbf{x}|y)$  for input units  $i$  corresponding to the individual components, features or dimensions  $x_i$  of input sample  $\mathbf{x}$  at layer  $l = 1$  and model output category  $y$  is achievable by initializing the layer-wise backpropagation process with the initial relevance quantity  $R_j^L(\mathbf{x}|y) = \delta_{jy} f_j^L(\mathbf{x})$ , with  $f_j^L(\mathbf{x})$  being the model output of the  $j$ -th neuron at output layer  $L$ . Using the Kronecker-Delta  $\delta_{jy}$ , only the output of the neuron corresponding to the output category  $y$  is propagated in the backward pass.

Let us uphold our assumption of knowledge about the concepts encoded by each filter or neuron

within a DNN. We generalize the principle of masking or selecting the model output for a particular outcome to be explained by introducing the variable  $\theta$  describing a set of conditions  $c_l$  bound to representations of concepts and applying to layers  $l$ . Multiple such conditions in combination might extend over multiple layers of a network. Note that we use natural numbers as identifying indicators for neural network filters (or elements in general) in compliance to the Kronecker Delta. Here,  $\theta$  then allows for a (multi-) concept-conditional computation of relevance attributions  $R(\mathbf{x}|\theta)$ .

We therefore extend the relevance decomposition formula in Equation (5), following the potential for a “filtering” functionality briefly discussed in [84] to

$$R_{i \leftarrow j}^{(l-1,l)}(\mathbf{x}|\theta \cup \theta_l) = \frac{z_{ij}}{z_j} \cdot \sum_{c_l \in \theta_l} \delta_{j c_l} \cdot R_j^l(\mathbf{x}|\theta) \quad (8)$$

where  $\delta_{j c_l}$  “selects” the relevance quantity  $R_j^l$  of layer  $l$  and neuron  $j$  for further propagation, if  $j$  meets the condition(s)  $c_l$  tied to concepts we are interested in. Note that for layers  $l'$  without explicitly selected conditions, our notation assumes *all* conditions applicable in that layer to be valid, i.e., if  $\theta_{l'} = \emptyset$  is an empty set, we define  $\forall j \exists! c_{l'} \in \theta_{l'} : c_{l'} = j$  and therefore  $\forall j \sum_{c_{l'} \in \theta_{l'}} \delta_{j c_{l'}} = 1$ . Thus, without conditions, attribution flow is not constrained, as no masking is applied. Furthermore, due to our approach based on binary masking, which controls the flow of backpropagated quantities through the model, this assumption illustrates that a combination of conditions *within* a layer  $l$  behaves similarly to a logical OR ( $\vee$ ) operator, and combinations of conditions *across* layers behave similar to logical AND ( $\wedge$ ) operators.

### 2.2.1 Possible Analyses with CRP

The most basic form of relevance disentanglement is the masking of neural network outputs for procuring class-specific heatmaps, as is shown in Figure 2. Here, heatmaps gain (more) detailed meaning by specifying a class output for attribution distribution, answering the question which features are relevant for predicting (against) a chosen class. Backpropagation-based XAI methods also assign attribution scores to neurons of intermediate layers, and thus further reveal the relevance of hidden neurons for a prediction.

Regarding DNNs, these hidden neurons can represent human-understandable concepts. It has been shown that the meaning of filters in a neural network is hierarchically organized within its sequence of layered representations, meaning that an abstract latent representation within the model is based on (weighted) combinations of simpler concepts in lower layers [147, 15, 53]. Such concepts can be allocated to individual neurons or groups of neurons, e.g., a filter or filters of a convolutional layer of a DNN. By introducing (multi-) conditional CRP, i.e., via a masking of hidden neurons, the relevance contribution of individual concepts used by a neural network can be, in principle, disentangled and individually investigated as well. This expands the information horizon to questions such as how relevant a particular concept is for the prediction, or which features are relevant for a specific concept. Following the LRP methodology, an adaptation of the CRP approach beyond CNN, e.g., to recurrent [9] or graph [113] neural networks, is possible.

**Global Concept Importance** The possibility to isolate and identify the global (in the context of a sample processed by the model<sup>1</sup>) importance of concepts with CRP is illustrated in Figure 3, and presumes the ability to meaningfully group the neurons of a hidden (e.g., convolutional) layer as per their function. While this will in practice be an arguably difficult task semantically (which will be explored in Section 4.4), we can exploit prior knowledge about the structure of the data and the architecture of the model at hand:

In the example shown in Figure 3, we use a feed-forward Convolutional Neural Network (CNN) based on the VGG-16 [123] model trained for object recognition on image data, which typically consists of blocks of convolutional and fully connected layers. The 2D-convolutional layers of the model consist of multiple learned filters sliding over the two spatial axes of the output activation of the previous layer (and transitively, over the input image), measuring the presence of specific structures in input space. Specifically, the tensor of output activations in a convolutional layer  $l$  is

<sup>1</sup>Not to be confused with the aspect of globality in “global XAI” (e.g., [15, 60, 53]), which describes insights about representations learned by the model in general, over whole datasets.

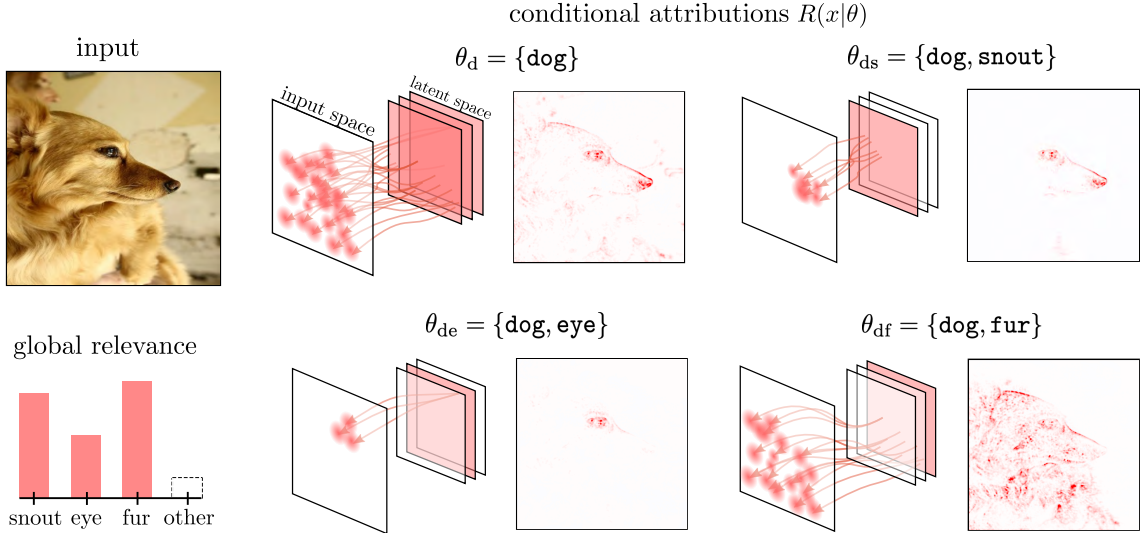


Figure 3: Explanation disentanglement via Concept Relevance Propagation: Target concept “dog” is described by a combination of lower-level concepts such as “snout”, “eye” and “fur”. CRP heatmaps regarding individual concepts, and their contribution to the prediction of “dog”, can be generated by applying masks to filter-channels in the backward pass. Global (in the context of an input sample) relevance of a concept wrt. to the explained prediction can thus not only be measured in latent space, but also precisely visualized, localized and measured in input space. The concept-conditional computation of  $R(\mathbf{x}|\theta_{df})$  reveals the relatively high importance of the spatially distributed “fur” feature for the prediction of “dog”, compared to the feature “eye”. The attribution of  $R(\mathbf{x}|\theta_{df})$  in the input space visualization of  $R(\mathbf{x}|\theta_d)$  (which was computed jointly over all concepts), however, is dominated by  $R(\mathbf{x}|\theta_{de})$  and  $R(\mathbf{x}|\theta_{ds})$  which both concentrate more strongly on smaller image regions and attribute both to the dog’s eye. Here, the visualization of  $R(\mathbf{x}|\theta_d)$  alone does not represent the relative importance of the concepts’ contributions to the “dog” outcome.

of shape  $(h_l, w_l, n_l)$ , where  $n_l$  is the number of filters applied to each of the possible  $h_l \times w_l$  vertical and horizontal positions in the input tensor, depending on filter size and stride. Since convolutional layers share the same set of weights among all applications along the spatial axes, and thus measure the same features, it can be assumed that each of the  $n_l$  output channels (or coactive group of output channels) encodes one particular concept. Note, that for fully connected layers, each output neuron receives inputs from *all* preceding input neurons. Thus, each output neuron (or coactive group of output neurons) can be regarded as the encoding of a concept. Consequently, the concept-conditional masking of the attribution backpropagation introduced in Equation (8) can be applied as-is to the concepts encoded via fully connected layers. For convolutional layers, we group the output neurons  $j$  into spatial and channel axes, and apply the masking to the channel axis only for the selection of concepts for backpropagation:

$$R_{i \leftarrow (p,q,j)}^{(l-1,l)}(\mathbf{x}|\theta \cup \theta_l) = \frac{z_{i(p,q,j)}}{z_{(p,q,j)}} \cdot \sum_{c_l \in \theta_l} \delta_{j c_l} \cdot R_{(p,q,j)}^l(\mathbf{x}|\theta) \quad (9)$$

Here, the tuple  $(p, q, j)$  uniquely addresses an output voxel of the activation tensor  $z_{(p,q,j)}$  computed during the forward pass through  $l$ , with  $p$  indicating the first and  $q$  the second spatial axis of the tensor, and  $j$  the channel- or (as per our assumptions) the concept-axis. Note that this notion of neuron groups based on prior knowledge about the data and model architecture can trivially be adapted to other cases, such as models using 1D-convolutions to process time series data (see Section 3.5), etc.

Our knowledge about the structure of the data and the architecture of the model allows the attribution-based selection of specific filters along the channel axis of a hidden convolutional layer, which can be identified with concepts such as “snout”, “eye” and “fur”. Here, we are then able to compare attribution maps wrt. class “dog” by selecting the respective model output at final



layer  $L$  to, e.g., the attributions for “dog  $\wedge$  fur” by additionally selecting channels responsible for fur pattern, animal snout or eye-like features encoded in a lower layer  $l$ . Specifically, in Figure 3 we choose  $\theta_d = \{L : \{\mathbf{dog}\}\}$ ,  $\theta_{df} = \{l : \{\mathbf{fur}\}, L : \{\mathbf{dog}\}\}$ ,  $\theta_{ds} = \{l : \{\mathbf{snout}\}, L : \{\mathbf{dog}\}\}$  and  $\theta_{de} = \{l : \{\mathbf{eye}\}, L : \{\mathbf{dog}\}\}$ , for the explanations of “dog”, “dog  $\wedge$  fur”, “dog  $\wedge$  snout” and “dog  $\wedge$  eye”, respectively. To uphold readability, however, we will define the following equivalent shorthand notation of  $\theta_{df} = \{\mathbf{dog}, \mathbf{fur}\}$  throughout the rest of the paper at our convenience. Therefore, the unique placement of concept-encoding feature descriptors within the model and the application of conditions at the correct location is assumed.

At this point, the relevance  $R^l(\mathbf{x}|\theta_c)$  of a concept (combination)  $c$  can be calculated by summation of relevances  $R_i^l(\mathbf{x}|\theta_c)$  in a given layer, e.g., at or below the lowest layer  $l$  where a part of the concept (combination) is expressed in latent space, as

$$R^l(\mathbf{x}|\theta_c) = \sum_i R_i^l(\mathbf{x}|\theta_c) , \quad (10)$$

or any other lower layer (e.g., the input space) to which the masking of the relevance flow wrt.  $c$  has taken full effect. Here, the conservation laws of CRP inherited from LRP (cf. Equation (7)) ensure that the amount of relevance  $R^l(\mathbf{x}|\theta_c)$  corresponds to the importance a concept combination selected via  $\theta_c$  has had to inference. The relevance scores assigned to specific concepts then give insight into the decision process of the model: Regarding a particular prediction, relevance scores aggregated for each concept illuminate which concept is used by the model during inference and how much it contributes to the prediction outcome.

Given the example shown in Figure 3, we can see that the concept “fur” is more important for the prediction of class “dog” than for example the concept “eye”, which is not apparent from the heatmap visualization of  $R(\mathbf{x}|\theta_d)$  alone. Here, the importance of “eye” is more explicit, despite its comparatively lower measured relevance sum, as this lower total quantity of relevance concentrates on a considerably smaller set of pixels (cf.  $R(\mathbf{x}|\theta_{de})$  vs.  $R(\mathbf{x}|\theta_{df})$ ), increasing the per-pixel relevance magnitude reflecting in visualized heatmap color space in bright red color.

**Local Concept Importance** Visualizations of concept-conditional relevance in heatmaps show *where* concepts contributing to a chosen network output are localized and recognized by the model in the input space. Typically, as discussed in Section 2.2, an explanation heatmap regarding a singular specific output class is described by a combination of interactions of individual concepts. The bar chart in the bottom left of Figure 3 illustrates how class-conditional attribution maps (here, for class “dog”) can be separated into the individual contributions of learned concepts using further refinement of the attribution backpropagation wrt. conceptual conditioning, on a global scale in context of the given sample.

At this point, given  $R_i^l(\mathbf{x}|\theta_c)$ , conceptual disentanglement allows measuring the individual importance of the in  $\theta_c$  selected concepts  $c$  on a local scale, i.e., over a subset  $\mathcal{I}$  of neurons  $i$  in layer  $l$ . Specifically, relevance scores  $R_i^l(\mathbf{x}|\theta_c)$  in, e.g., input space, can be aggregated meaningfully over image regions for the concept  $c$  to a localized relevance score

$$R_{\mathcal{I}}^l(\mathbf{x}|\theta_c) = \sum_{i \in \mathcal{I}} R_i^l(\mathbf{x}|\theta_c) \quad (11)$$

measuring the importance of a concept to the prediction on a set of given input features, e.g., pixels. Extending the notation introduced in Equation (9), for a convolutional layer with  $J$  channels, local relevance aggregation along the spatial axis is given by

$$R_{\mathcal{I}}^l(\mathbf{x}|\theta_c) = \sum_{(p,q) \in \mathcal{I}} \sum_{j=1}^J R_{(p,q,j)}^l(\mathbf{x}|\theta_c) , \quad (12)$$

aggregating over all positions  $(p, q)$  defined in the set  $\mathcal{I}$ .

For methods adhering to a conservation property such as CRP, this property permits the comparison of multiple local image regions  $\mathcal{I}$  and/or sets of concepts  $c$  in terms of (relative) importance of learned latent concepts, as illustrated in Figure 4. In the given example we compute relevance scores according to  $\theta_{ds}$ ,  $\theta_{de}$ ,  $\theta_{df}$ , et cetera, individually in input space. Then we aggregate

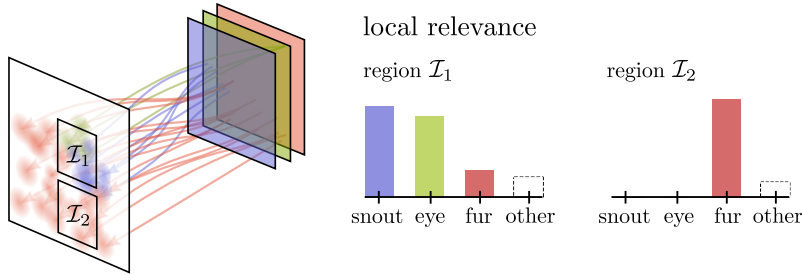


Figure 4: Concept Relevance Propagation, in combination with local aggregation of relevance scores  $R(\mathbf{x}|\theta)$  over regions  $\mathcal{I}_1$  and  $\mathcal{I}_2$ , based on the example given in Figure 3. Specifically, we compute  $R_i^l(\mathbf{x}|\theta_{ds})$ ,  $R_i^l(\mathbf{x}|\theta_{de})$ ,  $R_i^l(\mathbf{x}|\theta_{df})$  and others in order to assess their local contribution to the prediction outcome for class “dog”, and the origin of their contributions among image regions  $\mathcal{I}_1$  and  $\mathcal{I}_2$ .

the resulting attribution maps according to Equation (11) over two input regions  $\mathcal{I}_1$  and  $\mathcal{I}_2$  in order to locally measure the relative importance of by the model perceived concepts.

In Section 3.3 we combine the capabilities of localized CRP with our contributions from Section 2.3.3 to visualize a “Concept Atlas” which demonstrates which concepts models perceive and use locally for their decision making process.

**Hierarchical Composition of Relevant Concepts** Let us assume we have identified a particularly relevant concept  $c$  located in layer  $l$  via the computation of concept-conditional relevance attributions, resulting in a relevance quantity  $R_{(p,q,j)}^l(\mathbf{x}|\theta_c)$ . Let us further assume that we are interested in the composition of concept  $c$  in terms of sub-concepts in preceding network layers, as used by the model for the purpose of inferring the explained outcome. Leveraging CRP, we are able to go beyond the capabilities of related work [53, 75], which often is limited to the identification of per-model (i.e., static) or per-class interactions of concepts via the analysis of weights and/or activations. Specifically, using CRP, we can compute interactions of concepts encoded by the predictor  $f$  in context of the prediction of a particular sample  $\mathbf{x}$ , via the corresponding model outcome  $f(\mathbf{x})$  (as well as the conditions  $\theta_c$ ).

Let us further uphold the assumption that our model is a convolutional DNN for image categorization, i.e., the activation and attribution tensors we have access to have three axes. This assumption can of course be adapted to any other structuring of layer activations. Analogously to the tuple  $(p, q, j)$  indexing the spatial and channel axes of the upstream activations and relevance tensors at layer  $l$ , we introduce the tuple  $(u, v, i)$  applying to downstream tensors at preceding layer  $l - 1$ , with the spatial coordinates  $u$  and  $v$ , as well as the channel coordinate  $i$  addressing the different features/concepts encoded by the model. We can now further extend Equation (9) to

$$R_{(u,v,i)\leftarrow(p,q,k)}^{(l-1,l)}(\mathbf{x}|\theta_c) = \frac{z^{(u,v,i)(p,q,k)}}{z_{(p,q,k)}} R_{(p,q,k)}^l(\mathbf{x}|\theta_c), \quad (13)$$

where  $R_{(p,q,k)}^l(\mathbf{x}|\theta_c)$  is the already masked upstream relevance for concept  $c$  at layer  $l$  (and above), i.e., all channels  $j$  of layer  $l$  are masked except channel  $k$ . Further, the resulting  $R_{(u,v,i)\leftarrow(p,q,j)}^{(l,l+1)}(\mathbf{x}|\theta_c)$  represents the flow of downstream relevance messages from all upstream voxels  $(p, q, j)$  to downstream voxels  $(u, v, i)$ . In order to find the most relevant lower layer concepts in layer  $l - 1$  given our specific sample  $\mathbf{x}$  and conditions  $\theta_c$ , we can simply aggregate the downstream relevance into per-channel/concept relevances at layer  $l - 1$  over the spatial coordinates  $u$  and  $v$ :

$$R_i^{l-1}(\mathbf{x}|\theta_c) = \sum_{u,v} \sum_{p,q,j} R_{(u,v,i)\leftarrow(p,q,j)}^{(l-1,l)}(\mathbf{x}|\theta_c) \quad (14)$$

Optionally, the spatial coordinates  $(p, q)$  or  $(u, v)$  can trivially be selected over regions  $\mathcal{I}$  as in Equation (12), should a more localized analysis of layer- and concept interaction be desired.

Figure 5 visualizes the approach taken in Equations (13) and (14). The property of proportionality ensures that the relative importance of each  $R_i^{l-1}(\mathbf{x}|\theta_c)$  for concept  $c$  in layer  $l$  is represented.

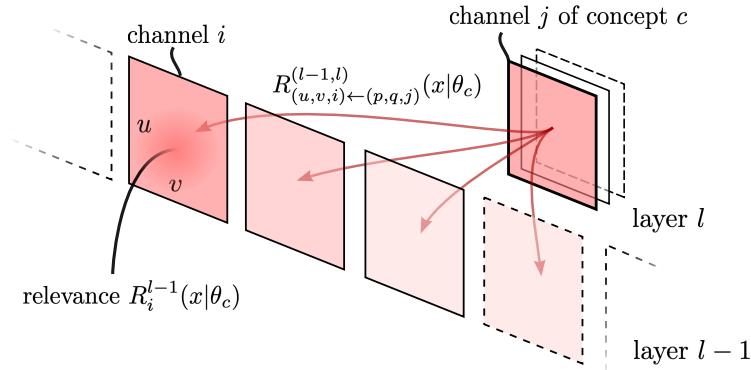


Figure 5: Given a particularly interesting concept  $c$  encoded by channels  $j$  in layer  $l$ , as well as  $R_i^l(\mathbf{x}|\theta_c)$ , adequately aggregated relevance quantities computed during a CRP backward pass can be utilized to identify how  $R_j^l(\mathbf{x}|\theta_c)$  distributes across lower layer channels (here shown side-by-side in an exploded view) representing concepts, as  $R_i^{l-1}(\mathbf{x}|\theta_c)$ . The identification of the most influential concepts in layer  $l-1$  contributing to concept  $c$  in layer  $l$  wrt. an explanation computed regarding  $\theta_c$  is then just a matter of ranking  $R_i^{l-1}(\mathbf{x}|\theta_c)$ , e.g., by (signed) magnitude.

The properties of conservativity and conditionality ensure that the here measurable interactions between concepts in adjacent layers are specific to the data sample  $\mathbf{x}$ , the respective model outcome  $f(\mathbf{x})$  as well as the conditions  $\theta_c$  set for the computation of relevance.

The composition of  $c$  in  $l$  is given by the most relevant lower layer concepts  $b$  in layer  $l-1$  and can then (simply) be obtained by sorting, e.g., via

$$\mathcal{B} = \{b_1, \dots, b_n\} = \text{argsort}_i^{\text{desc}} R_i^{l-1}(\mathbf{x}|\theta_c) \quad (15)$$

for selecting the concepts supporting  $c$  the most, in context of the sample  $\mathbf{x}$  and the desired explanation specified via  $\theta_c$ . Sorting ascendingly would return the least supporting and potentially contradicting concepts in context of  $\mathbf{x}$  instead.

Subsequently, we define  $\mathcal{B}_k$  as the set containing the  $k$  most (least) relevant concepts  $b_i$ . Specifically,  $\mathcal{B}_k$  is defined as

$$\mathcal{B}_k = \{b_1, \dots, b_k\} \subseteq \mathcal{B} \quad (16)$$

In Section 3.4, we use this information together with our contributions from Section 2.3.3 to visualize an ontology-like semantic composition of concepts from sub-concepts specific to individual predictions.

## 2.3 Understanding Concepts in Latent Representations

In the previous section, we have introduced CRP, assuming that neurons can be identified with specific concepts, which are used by a neural network in the prediction process. In fact, several works in the field of Feature Visualization [36, 130, 147, 78, 87, 94] have shown different functions of individual neurons using visualizations in the input space.

The emergence of human-understandable concepts in neurons of a DNN has been observed in several works [148, 94, 102, 16, 24, 44], although the networks were not explicitly trained to use them. While lower-layer neurons encode features like textures and edges, higher-layer neurons have been observed to conceptualize notions from simple objects to abstract emotions [148, 94]. Even the existence of multimodal neurons was reported, that respond to a concept regardless of whether it is shown as a photograph, cartoon or written in textual form [44].

While the gradual formation of abstract concepts is widely known, it is surprising to see that a non-negligible amount of neurons encode features, that resemble the way humans categorize the world. Our work joins a whole series of papers showing that single neurons not only encode invariant concepts useful for solving the task, but that these can also be understood by humans and thus enable interpretability of a DNN’s reasoning. Nevertheless, assigning meaning to individual units is often subjective and depends on the human observer. Further, generative representations

might not be necessarily human-interpretable. Thus, misinterpretation or misunderstanding of the inner functioning of a chosen model is possible.

In the following, we therefore discuss current feature visualization techniques and present novel methods to improve concept identification and understanding.

### 2.3.1 Generative Approaches to Understanding Latent Features

A large part of feature visualization techniques rely on Activation Maximization (ActMax), where in its simplest form, input images are sought that give rise to the highest activation value of a specific unit. In general, ActMax can be seen as an optimization problem, i.e., maximizing a neuron’s activation, which can be solved using Gradient Ascent (GA).

Let  $z_i^l(\mathbf{W}, \mathbf{x})$  be the activation of neuron  $i$  in layer  $l$ . Here,  $\mathbf{W}$  denotes the parameters of a neural network and  $\mathbf{x}$  denotes the input being an element of the input space  $\mathcal{X}$ . Then formally, we seek to find the input  $\mathbf{x}^*$  leading to a maximal activation:

$$\mathbf{x}^* = \operatorname{argmax}_{\mathbf{x} \in \mathcal{X}} z_i^l(\mathbf{W}, \mathbf{x}). \quad (17)$$

While conceptually simple, preventing the emergence of adversarial examples became a main research endeavor. Several priors were proposed to guide optimization into realistic looking images, e.g., Transformation Robustness [87], Frequency Penalization [78], Preconditioning [94], and learning a natural prior from data distribution [90].

Despite progress made, the generation of high-resolution and natural images from deep networks remains challenging. User studies [20] also found, that synthetic images tend to be abstract and more difficult for people to interpret than real example images. Therefore, without limitation of generalization, we will focus on data-based approaches in the following Sections.

### 2.3.2 Activation-based Reference Sample Selection

Alternatively to generative sample synthesis, other works [143, 28] propose to select reference samples from existing data for feature visualization and analysis. In the literature, the selection of reference samples for a chosen concept  $c$  manifested in a neuron (group) is often based on the strength of activation induced by a sample. Here, in principle, samples leading to a strong activation of the corresponding neuron (group) are assumed to likely incorporate the concept  $c$  of interest. For data-based reference sample selection, the input space is restricted to elements of a particular dataset  $\mathcal{X}_d \subset \mathcal{X}$ . Thus, we seek to find data samples  $\mathbf{x}$  of a finite set  $\mathcal{X}_d$  that result in the highest activation values for a specific unit. Without limitation of generality, the dataset is in the following assumed to consist of images. However, the same principles apply to time series data, tabular data or any other arbitrary data format for feed-forward neural networks<sup>2</sup>.

As discussed in Section 2.2.1, all neurons of a convolutional layer’s channel of a DNN can be identified with the same concept due to the learned filters’ (assumed) spatial invariance. Thus, in literature [28], entire filters instead of single neurons are investigated for convolutional layers. Here, in principle, different maximization targets  $\mathcal{T}(\mathbf{x})$  can be specified, that define a “maximum” channel activation.

One particular choice of  $\mathcal{T}(\mathbf{x})$  is to identify samples  $\mathbf{x}^* \in \mathcal{X}_d$ , which *maximize the sum* over all channel activations, i.e.,

$$\mathcal{T}_{\text{sum}}^{\text{act}}(\mathbf{x}) = \sum_i z_i(\mathbf{x}) \quad (18)$$

resulting in samples  $\mathbf{x}_{\text{sum}}^{\text{act}}$  which are likely to show a channel’s concept in multiple input features, as the entire channel is maximized. However, while targeting all channel neurons, reference samples including both concept-supporting and contradicting features might result in a low score  $\mathcal{T}_{\text{sum}}^{\text{act}}$ , as negative activations are taken into account by the sum. Alternatively, a non-linearity can be applied additionally, e.g., ReLU, focusing only on positive activations.

<sup>2</sup>The same analysis for Recurrent Neural Networks is more challenging as time dependency must be taken into account.

A different choice is to define maximally activating samples by looking at the *maximum channel activation*, i.e.,

$$\mathcal{T}_{\max}^{\text{act}}(\mathbf{x}) = \max_i z_i(\mathbf{x}) \quad (19)$$

leading to samples  $\mathbf{x}_{\max}^{\text{act}}$  with a more localized and strongly activating set of input features characterizing a channel’s concept. These samples  $\mathbf{x}_{\max}^{\text{act}}$  are more difficult to interpret, as only a small region of a sample might contain the concept. Thus, concepts might be more difficult to grasp for the human observer.

Chen et al. [28] have observed, that  $\mathcal{T}_{\text{sum}}^{\text{act}}$  is better suited to find samples for lower-level concepts, and  $\mathcal{T}_{\max}^{\text{act}}$  for higher-level concepts. Thus, they propose to use a max-pooling operation followed by summation for the maximization target representing a mixture out of both  $\mathcal{T}_{\text{sum}}^{\text{act}}$  and  $\mathcal{T}_{\max}^{\text{act}}$ . However, we argue that  $\mathcal{T}_{\max}^{\text{act}}$  could also be utilized by handling the problem of localization with sub-sample-selection and conceptual heatmaps presented in the following sections.

In order to collect multiple reference images describing a concept, the dataset  $\mathcal{X}_d$  consisting of  $n$  samples is first sorted in descending order according to the maximization target  $\mathcal{T}(\mathbf{x})$ , i.e.

$$\mathcal{X}^* = \{\mathbf{x}_1^*, \dots, \mathbf{x}_n^*\} = \underset{\mathbf{x} \in \mathcal{X}_d}{\text{argsort}}^{\text{desc}} \mathcal{T}(\mathbf{x}). \quad (20)$$

Subsequently, we define  $\mathcal{X}_k^*$  as the set containing the  $k$  most maximizing samples  $\mathbf{x}^*$ . Specifically,  $\mathcal{X}_k^*$  is defined as

$$\mathcal{X}_k^* = \{\mathbf{x}_1^*, \dots, \mathbf{x}_k^*\} \subseteq \mathcal{X}^* \quad (21)$$

In the following, we denote the set of reference images obtained by taking the summation of activation as  $\mathcal{X}_{\text{sum}}^{\text{act}}$  and the set obtained by taking the maximal value of activation as  $\mathcal{X}_{\max}^{\text{act}}$ . From Equations (18) and (19) it then generally follows, that

$$\mathcal{X}_{\text{sum}}^{\text{act}} \neq \mathcal{X}_{\max}^{\text{act}}. \quad (22)$$

Due to the different maximization targets  $\mathcal{T}_*^{\text{act}}(\mathbf{x})$  an experimental comparison between both variants and our relevance-based reference sample selection approach (presented in the next section) motivated by [28], can be found in Section 3.1.

### 2.3.3 Introducing Relevance-based Reference Sample Selection

The hierarchical structure in DNNs encourages concepts in higher layers to be invariant to transformations in the input domain. This leads to the emergence of multifaceted features that respond to different manifestations<sup>3</sup> of a concept: For instance, a neuron that encodes for “apples” might activate for different colors (green, yellow, red) or other shapes (cut in half, with or without peel). See Figure 9 in Section 3 for a visual example. Likewise, the emergence of polysemantic neurons was reported, that fire for different concepts [94, 16, 24, 44].

Multifaceted neurons [91] are particularly challenging to illustrate, as (potentially conflicting) different facets cannot be easily visualized in a single image. Gradient based methods either illustrate all facets at once, resulting in unintelligible images, or reveal only one facet, ignoring other important ones [91, 44]. When using real images instead, the sheer volume of images makes it difficult to filter out facets. Thus, typically only the  $k$  most important samples are displayed.

To enforce more variety in reference samples for ActMax, the authors of [91] introduce the Multifaceted Feature Visualization algorithm, which projects the latent representation into a 2D embedding using t-SNE and applies  $k$ -means to extract clusters of reference images. Other works initialize gradient ascent with random seeds [36], or regularize the optimization process with cosine similarity to enforce more variety [94]. Although these techniques enhance sample variety and increase understanding, it is still an open question, which manifestations are preferred by the network in practice. In theory, many facets can activate a neuron, however, only few manifestations might be significantly used for a neural network’s predictions. Simply because an image leads to

<sup>3</sup>One definition of a concept is the abstraction obtained by generalization from particulars [125]. For example, the concept “roundness” can be explained by reference images of a clock or a ball. It is then the task of the human observer to abstract the universal concept from several reference images. In the following, we will use “manifestation” or “facet” also as synonyms for particular.

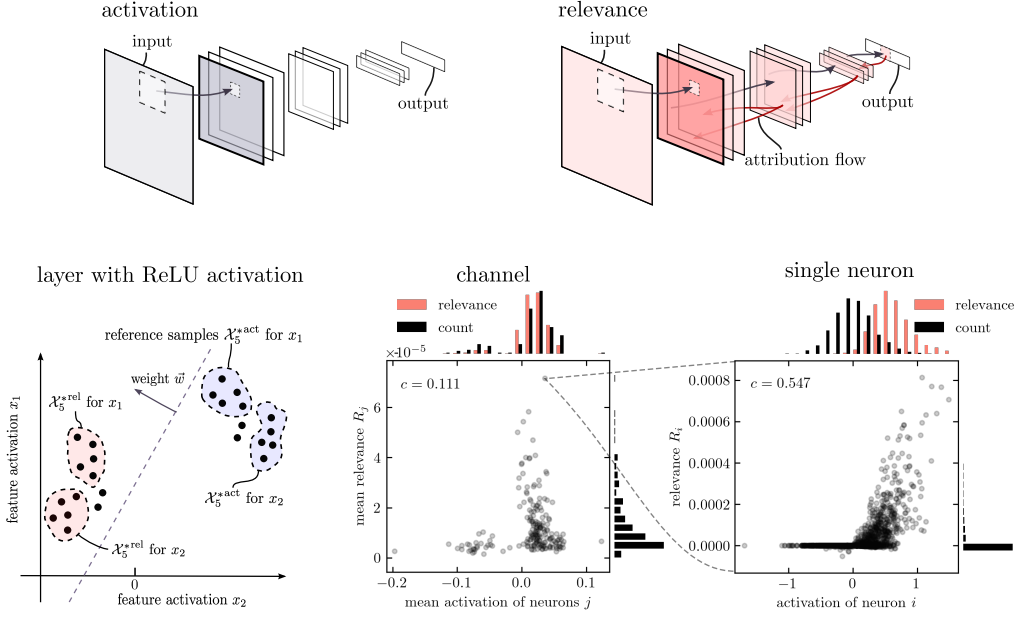


Figure 6: (*Top left*): Activation scores only measure the stimulation of a latent filter without considering the *role* of that filter during inference. (*Top right*): Relevance scores are contextual to distinct model outputs and describe how features are used in a DNN’s prediction of, e.g., a specific class. (*Bottom*): Assume we wish to find representative examples for features  $x_1$  and  $x_2$ . Even though a sample leads to a high activation score in a given layer and neuron/channel — here  $x_1$  and  $x_2$  — it does not necessarily result in high relevance or contribution to inference: On the left, the feature transformation  $\vec{w}$  of a linear layer with inputs  $x_1$  and  $x_2$ , which is followed by a ReLU non-linearity, is shown. Here, samples from the blue cluster of feature activations lead to high activation values for both features  $x_1$  and  $x_2$ , and would be selected by ActMax, but receive zero relevance, as they lead to an inactive neuron output after the ReLU, and are thus of no value to following layers. That is, even though the given samples activate features  $x_1$  and  $x_2$  maximally strong, they can not contribute meaningfully to the prediction process through the context determined by  $\vec{w}$ , and samples selected as representative via activation might not be representative to the overall decision process of the model. Representative examples selected based on relevance, however, are guaranteed to play an important role in the model’s decision process. To the (*center*) and (*right*) respectively, correlation analyses are shown for an intermediate ResNet layer’s channel and neuron. Neurons that are on average highly activated are not, in general, also highly relevant, as a correlation coefficient of  $c = 0.111$  shows, since a *specific* combination of activation magnitudes is important for neurons to be representative in a larger model context.

high activation does not mean that the image is representative of the neuron’s function in a larger inference context. Adversarial examples are a prime example of this.

In this sense, we take up the authors’ remark in [94]: “*The truth is that we have almost no clue how to select meaningful directions [of activations], or whether there even exist particularly meaningful directions.*” and introduce the method of Relevance Maximization (RelMax) as a complement to Activation Maximization. Regarding RelMax, we do not search for images that produce a maximal activation response. Instead, we ask: *How, and for which samples, does the model use the neuron in practice?*

Thus, in order to select the most relevant samples, we define maximization targets  $\mathcal{T}_*^{\text{rel}}(\mathbf{x})$  by using the relevance  $R_i(\mathbf{x}|\theta)$  of neuron  $i$  for a given prediction, instead of its activation value  $z_i$ . Specifically, the maximization targets are given as

$$\mathcal{T}_{\text{sum}}^{\text{rel}}(\mathbf{x}) = \sum_i R_i(\mathbf{x}|\theta) \quad \text{and} \quad \mathcal{T}_{\text{max}}^{\text{rel}}(\mathbf{x}) = \max_i R_i(\mathbf{x}|\theta). \quad (23)$$

It is to note, that the activation-based maximization targets are only specific to the sample (and

filter). Class-specificity may only be obtained in data-collection-based approaches, given sufficient label information, by pre-selecting samples from classes of interest [53].

Utilizing relevance scores  $R_i(\mathbf{x}|\theta)$  instead, the maximization target is class- (true, predicted or arbitrarily chosen, depending on  $\theta$ ), model-, and potentially concept-specific (depending on  $\theta$ ), as illustrated in Figure 6. The resulting set of reference samples thus includes only samples which depict facets of a concept that are *actually useful* for the model for inference. In Section 3.2 we will show how conditioning the relevance computation to different classes provides more clarity about a concept’s functioning.

How different resulting reference sets  $\mathcal{X}_k^{\text{act}}$  and  $\mathcal{X}_k^{\text{rel}}$  can occur, is depicted in Figure 6 (*bottom left*). Here, a hypothetical transformation within a linear layer  $l$  followed by a ReLU non-linearity in a two-dimensional activation space is shown. Two clusters of points are projected to different sides of the hyperplane described by the weighted normal vector  $\vec{w} = (w_1, w_2)$  with  $w_1 > 0$ ,  $w_2 < 0$  and bias term  $b$ . The output  $y$  is thus given by  $y = \text{ReLU}(w_1x_1 + w_2x_2 + b)$ , leading to relevances for features  $x_i$  of

$$R_i^l = \begin{cases} \frac{w_i x_i}{w_1 x_1 + w_2 x_2 + b} R^{l+1} & \text{if } y > 0 \\ 0 & \text{else.} \end{cases} \quad (24)$$

Here, inactive neurons (with  $y = 0$ ) cannot be attributed with relevance scores  $R \neq 0$ . Whereas samples from the blue clusters lead to a high activation for both features  $x_1$  and  $x_2$ , they are not relevant (or used) by the model in the following computation, as they lead to an output of zero. Note, that due to the ReLU non-linearity, negative outputs are set to zero. Samples from the red cluster result in smaller activations, but are actually depicting concepts, which can be used in the remaining prediction steps as they cause the output neuron represented by  $\vec{w}$  to activate. Experiments showing the differences in reference sample sets are located in Section 3.1.

Relevance attributions depend on the activations  $x_i$ , as Equation (24) illustrates. However, attributions are not strictly correlated to activations, because they also depend on the downstream relevances propagated from higher layers affected by feature interactions at the current and following layers. In Figure 6 (*bottom center and right*), correlation analyses are shown for an intermediate ResNet layer. In the left of both panels, mean activations and relevances are shown for all neurons of a CNN channel. Here it is shown, that neurons that are on average highly activated are not, in general, also highly relevant, as a correlation coefficient of  $c = 0.111$  demonstrates. The right plot depicts activation and relevance values of a strongly activating neuron. As has been discussed previously, samples leading to a high feature activation do not necessarily also result in high feature relevance. Here, a correlation coefficient of  $c = 0.547$  supports however, that relevance is dependent on activation.

To summarize, reference samples from ActMax-sorting illustrate feature interactions that lead to a high excitation value, and thereby important (to higher layers) but yet weaker activating concepts may not be taken into account. Relevance Maximization takes all higher layer activation distributions into account and is consequently a middle way between assigning semantics only to orthogonal activation basis vectors (i.e., single neurons) or a combination of them, by focussing on activations which see further use in a larger inference context.

### 2.3.4 Zooming into the Reference Sample by Using Receptive Field Information

Related work (e.g., [28]) visualizes whole data samples based on activations of (parts of) latent representations. However, depending on the maximization target, concepts of interest might take up only a small part of the input sample. Further, selected samples might include *multiple* concepts, hampering the process of identifying the *right* concept. One step towards better concept localization in input samples is to visualize the input of receptive field of a maximally activated or relevant neuron, as is also discussed in [143]. Concept localization and identification is made easier due to the masking of all other (possibly distracting) concepts outside the receptive field. Moreover, the receptive field represents an upper bound to the true scale of the concept of interest.

Specifically, the receptive field of a neuron is the portion of the input space, that can contribute to the neuron’s activation, which is determined by the neuron’s connectivity to lower layers. Since each neuron in a channel can be assumed to encode features representing the same concept, the

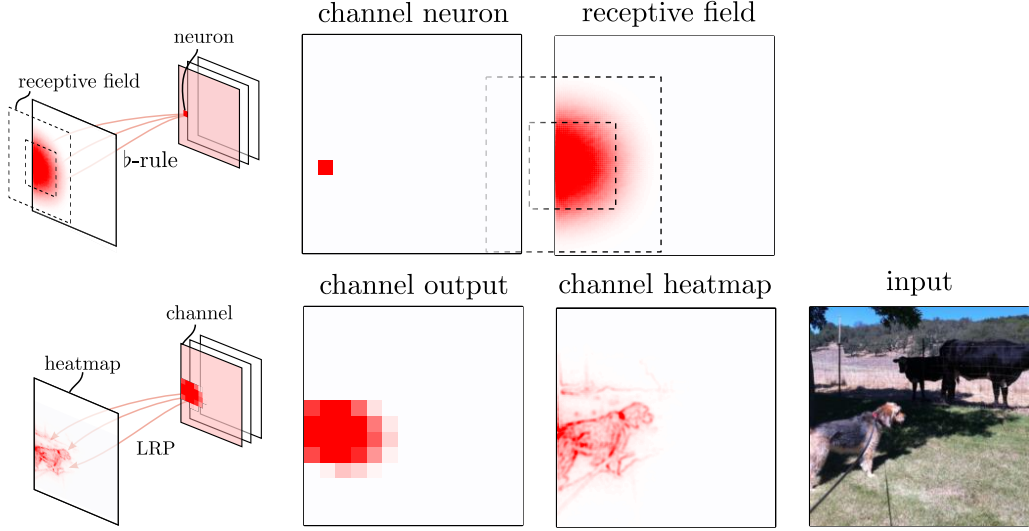


Figure 7: (Top) CRP readily offers receptive field calculation using the LRP  $\flat$ -rule starting at the neuron of interest. (Bottom) CRP can further be used to improve resolution of activation maps for (convolutional) filters by beginning relevance propagation at the actual channel activations.

receptive field of a singular neuron can be used to identify the input area responsible for the excitation and thus the scale limit of the by the filter/neuron learned concept.

As receptive field computations for DNNs are not straight forward, libraries specialized on this task, such as [7], have been developed. In the following, we present a trivial alternative for receptive field computation using the  $\flat$ -rule<sup>4</sup> of LRP. By choosing one specific neuron activation as the starting point for relevance decomposition in the backward pass, we can apply the LRP  $\flat$ -rule to calculate the receptive field of the particular neuron in intermediate layers until the input layer is reached (see Figure 7).

Using the  $\flat$ -rule, relevance of upper-level neuron  $j$  is equally distributed to all contributing lower-level neurons, i.e., for all connected neuron pairs, we set  $\forall i, j z_{ij} = 1$  in Equation (5), resulting in  $z_j = \sum_i z_{ij} = \sum_i 1$ , thus disregarding any influence of learned weights or input features. Layer after layer, any neuron that contributed computationally by being (transitively) connected to the neuron starting the backpropagation, receives attribution scores  $> 0$ . The more often an input neuron contributes, the higher the attribution score it receives.

In general, at a layer  $l$ , the set  $\mathcal{I}_{\text{rec}}$  of neurons<sup>5</sup> inside the receptive field of neuron  $j$  located in layer  $l' > l$  is given as

$$\mathcal{I}_{\text{rec}(j \in l')}^l = \{i \in l \mid R_i^l(\mathbf{x} | \theta_{j \in l'}) \neq 0\}, \text{ with } \theta_{j \in l'} = \{l' : \{j\}\}. \quad (25)$$

Here, the condition  $\theta_{j \in l'} = \{l' : \{j\}\}$  ensures the LRP initialization at layer  $l'$  with neuron  $j$ , i.e.,  $R_k^{l'}(\mathbf{x}) = \delta_{kj}$ . It is to note, that this method can also be applied to non-image data.

Having calculated the set  $\mathcal{I}_{\text{rec}(j \in l')}^1$  of input features inside the receptive field of neuron  $j$ , the input sample can be cropped to incorporate solely the pixels inside  $\mathcal{I}_{\text{rec}(j \in l')}^1$ , e.g., by fitting a bounding box around the “blob” of attribution scores exceeding a given threshold. As is illustrated in Figure 7 (top), the size of the receptive field might differ for neurons at different spatial positions inside a convolutional layer’s channel. In this particular case, a channel neuron’s receptive field close to the (input-dependent) spatial channel edge results in a rectangular receptive field shape in pixel space, which becomes more squared, if positioned closer to the channel’s spatial center. Application of convolutions with input padding (e.g., with zeros) during the forward pass are leading to the effect in this case, due to filters placed partially “outside” the input-connected spatial extent of the channel. Therefore, neurons close to the spatial edge of a channel filter can result in a receptive field which extends into the padded areas. (The resulting differences in receptive field sizes (wrt.

<sup>4</sup>read: “flat”-rule [68, 64]

<sup>5</sup>or pixels in  $l = 1$



the possible maximum) can be handled by, e.g., padding with a contrastive or transparent color, if a uniform size is favored.)

In summary, the selection of subsamples from only a filter’s or neuron’s receptive field can help with the identification and localization of the core manifestation of the encoded concept. For the purpose of receptive field computation, we use efficient tools already available in the LRP toolset. The effects of our technique are visualized in Figure 8 and further extended in the following Section 2.3.5.

### 2.3.5 Explaining Exemplary Explanations with CRP

Receptive fields of neurons in later stages of a network can cover larger input regions, or even the whole input, as is the case for dense layer neurons. Thus, encoded concepts can be much smaller than a receptive field, creating the need for further localization (i.e., within the receptive field).

For convolutional layers, an intuitive way to localize important regions is up-sampling of channel activations, as is done with Network Dissection [16]. This is sensible, as convolutions are always applied locally in the spatial dimension and thus, layer after layer, activations tend to stay in the same spatial position. However, this approach lacks precision, as up-sampling introduces blurriness [149], and is further limited to convolutional layers.

Application of LRP and in extension CRP allows to go beyond channel up-sampling by precisely resolving important input features and further being applicable to dense layer neurons as well. Specifically, CRP can be utilized to calculate heatmaps for any concept of interest and thus aid in concept localization. Therefore, two cases can be distinguished: (1) If one is interested in which input feature of a given data sample a specific filter is activated regardless of any class, then LRP is initialized starting at the filter output of choice, backpropagating with the actual activations, i.e., the score output by the observed latent concept detector. This yields an indication of where the concept is localized in the input space. (2) Alternatively, relevance can be conditioned to a specific class output. Then, the heatmap depicts, where the concept is used in the prediction of a chosen class. The precise localization of relevant input features for the activation of DNN channels is shown in Figure 7 (*bottom*).

Here, the activations of channel  $c$  in layer  $l$  during the prediction of the input  $\mathbf{x}$  are collected. Thereafter, the heatmap computation is initialized with the activations  $z_{(p,q,j)}^l$ , i.e.,  $R_{(p,q,j)}^l(\mathbf{x}|\theta) = z_{(p,q,j)}^l \delta_{jc}$  for all channels  $j$  and spatial coordinates  $p$  and  $q$ . Analogously, initialization for dense neurons is given as  $R_j^l(\mathbf{x}|\theta) = z_j^l \delta_{jc}$  for all neurons  $j$ . Using CRP, we can thus visualize, where a concept activates in high-precision independent of the layer architecture. This way, we are not limited to convolutional layers, but applications to fully connected layers (and others) commonly built into Multilayer Perceptron (MLP) and Recurrent Neural Network (RNN) models [10] are conceivable as well. Further, by defining additional conditions, information can be extracted at a higher degree of detail. For example, beginning relevance decomposition at a specific class output  $y$ , we can localize where a concept of channel  $c$  (in layer  $l$ ) is used for the prediction of class  $y$ . This follows the approach presented in Section 2.2 with relevance propagation using the condition  $\theta_{cy} = \{l : \{\text{neurons } j \text{ of channel } c\}, L : \{y\}\}$ .

In Figure 8, we see, how concept/channel-wise CRP heatmaps can aid in the process of concept localization and understanding. In the set of full-size reference samples shown in the top row, it is not obvious to identify the common concept. While using receptive field information to crop out the crucial part of the reference images (*2nd row*), using the CRP heatmaps (*3rd row*), additionally highlights the presence of orange/red next to white/gray colored parts of the samples as the definite key component of the concept reference samples have been identified and presented for. In order to further improve concept localization and readability, the reference images can be masked using heatmap information, by removing distracting background objects. To achieve this, a Gaussian filter can be utilized to smooth the heatmap in the first step. In the second step, a threshold can be chosen below which image parts are masked with black color (or any other suitable background of choice), as shown in the last row of Figure 8.

Naturally, in the given full-sized example images alone in Figure 8, a human observer may involuntarily focus on the striking red dot on the bird’s breast (4th reference example in top row of Figure 8) or the top half of the “Pepsi” logo (3rd reference example) and be distracted from the

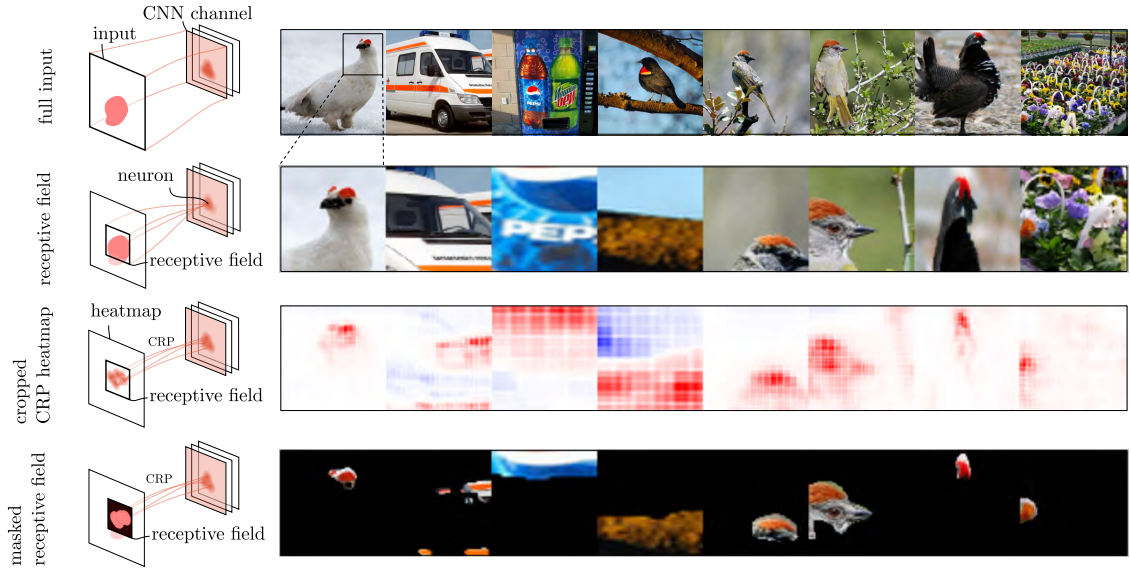


Figure 8: Improving concept visualization and localization using reference samples. (*Top row*): Full sized reference samples in  $\mathcal{X}_8^{\text{act}}$  leading to the largest activation values for a channel of interest. (*2nd row*): The same reference samples cropped to the receptive field of the most activating neuron. (*3rd row*): CRP heatmap wrt. the filter output of the cropped reference samples. (*Bottom row*): Cropped reference samples masked wrt. CRP heatmap and a threshold of 40 % of the maximal heatmap value. The concept encoded by a filter can be much smaller than an input image. Cropping the input image to the receptive field of the most activating neuron does increase the focus on the most defining sub-image matching the observed filter’s receptive field. A combination with a CRP backward pass of the reference sample’s filter activation can further highlight the core concept. Optionally, distracting image information of which the relevance attribution falls below a given threshold and may be masked out, leaving only the concept-defining parts of the cropped samples for observation. Understanding the function of a filter thus becomes considerably easier in comparison to only using whole reference example images. Further examples can be found in Figures A.3 in Appendix A.4.

actual concept summarized by the presented examples<sup>6</sup>. A cropping of the most activating part of the sample, followed by relevance map computation however reveals that in fact the model uses the analyzed filter to focus on the brown-orange part of the branch and the red-white transition in the presented examples. A similar observation can be made for the field of flowers shown in the rightmost reference example. The sample represents a combination of orange and white color next to each other, which is not apparent from looking at the full sized input image in the top row. By first cropping the local image patch yielding the highest latent channel activation, and then explaining the observed filter’s reaction to the cropped reference sample via LRP it becomes clear that the model is stimulated by a singular blossom near the bottom left corner of the image and ignores all others. These examples show that human perception can be misguided when only observing whole images for the purpose of understanding latent representations of ML predictors.

### 3 Experiments I : Explaining Concepts with Examples

The visual and qualitative support for understanding predictions provided through relevance-based global explanations are shown in this section. In particular we first contrast our relevance-based reference example selections to activation-based reference example selection on popular real world image datasets in Section 3.1. We then follow up by establishing how concept understanding can be improved by focusing onto the common denominator of presented reference samples via class-conditionally selecting relevance examples and extending reference dataset variety in Section 3.2.

<sup>6</sup>the authors certainly did and were

Sections 3.3 and 3.4 then leverage the tools established in Section 2.2.1 for building localizing concept maps and identifying conceptual compositions along the sequence of neural network layers by tracking the backward flow of relevance in fine granularity.

We conclude with Section 3.5 by demonstrating that our concept-based approach to explaining neural networks predictions can be applied to arbitrary data, not only images, at hand of an experiment on time series data.

### 3.1 Activation- vs Relevance-based Sample Selection

The criteria after which reference samples are chosen impact the resulting sample sets for concept identification.

We have stated that relevance-based reference samples show how concepts are *used* in practice. Activation-based samples, on the other hand, illustrate the strongest (potentially adversarial) manifestations along the direction or dimension describing a concept in latent space. In general, both sample sets can overlap, as relevance and activation correlate to some extent (see Figure 6). However, this is in general not the case, causing the respective sets of reference samples to (potentially highly) differ. Thus, it is a sensible option to observe both relevance and activation-based reference sample sets complementarily, as they can provide different perspectives on the function of an analyzed neuron or filter, as can be understood from the case studies below. However, the potentially adversarial nature of activation-based reference sample selection needs to be considered carefully, as will be discussed in context of the second case study and Figure 10.

In order to illustrate the differences in samples sets selection that can occur, we present and discuss the following small case studies.

**Case Study 1: Higher-Level Concepts** Two examples of reference sets for higher-level concepts extracted from two upper convolutional layers of a pre-trained VGG-16 network (See Appendix A.2 are shown in Figure 9. Here, scatter plots show different examples positioned in  $\mathbb{R}^2$  according to their relevance attributions and layer activations of the sample sets  $\mathcal{X}_{8\text{sum}}^{\star\text{rel}}$  (red shaded) and  $\mathcal{X}_{8\text{sum}}^{\star\text{act}}$  (blue shaded).

In the left plot, we identified a polysemantic channel in layer `features.26` of a VGG-16 model, that encodes for cars and coarse patterns. Activation-based samples present cars of intense color and vegetables where a coarse pattern is dominant. Specifically, 8 out of the 10 classes for which the neuron activates strongest on average are “car”-specific<sup>7</sup>. The two other classes are “banana” and “artichokes”. Reference images obtained via RelMax-sorting tell a different story: Whereas vehicles seem to be important on one hand, the top three classes in terms of relevance attributed to the channel are, on the other hand: “alligator”, “limousine” and “crocodile”. These three classes are all having in common a gray color — contrary to the colorful images from ActMax-sorting. Further, the coarse pattern detector is by the model mainly utilized to classify reptiles instead of fruits. In hindsight, the bananas and artichokes obtained via Activation Maximization structurally match the scale pattern of reptiles, however the color saturation “overshoots”. In fact, for sample  $x_{1\text{sum}}^{\star\text{rel}}$  (“alligator” class) the second most relevant filter in layer `features.26` is indeed this unit accounting for 5.1% of total absolute relevance. Analyzing the sample  $x_{1\text{sum}}^{\star\text{act}}$  (“ambulance” class), the filter ranks only at position 27 accounting for 0.8% of total absolute relevance, thus, having no significant contribution to the decision process, as the perturbation experiment in Section 4.1 demonstrates. This exemplifies that a maximally strong activating filter cannot be equated with its usefulness for classification.

The right plot of Figure 9 shows the reference sample sets for channel 361 in `features.30` of a VGG-16 model with BatchNorm layers (see Appendix A.2). As ActMax-sorting suggests, the neuron’s function consists of the detection of thin white lines, since spider webs or whiskers are visible in the images. On the other hand, samples drawn to maximize relevance mostly depict written characters. Thus, activation indicates which general pattern a filter activates whereas relevance clarifies its specific usage. In this particular case, RelMax-sorting has revealed a Clever Hans [69] feature, which extends to several classes of the ImageNet dataset, as further analysis in Section 4.3 will verify.

<sup>7</sup>classes: “ambulance”, “minibus”, “trolleybus”, “police van”, “minivan”, “beach wagon”, “fire truck” and “pickup”

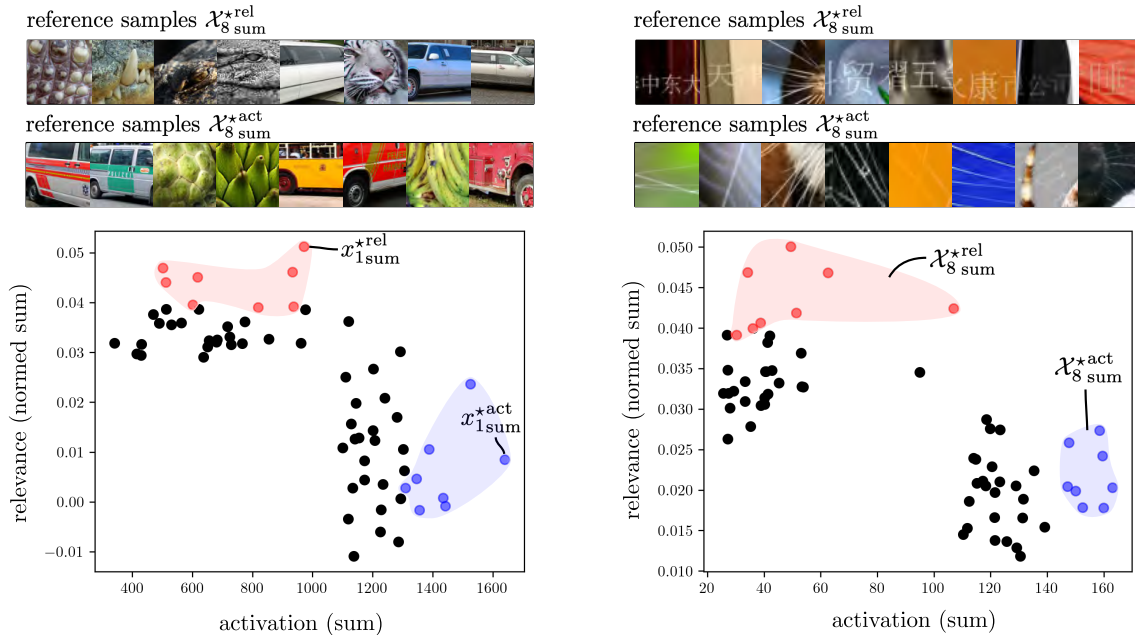


Figure 9: Relevance-based reference samples illustrate how concepts are *used* in a global inference context of the model, activation-based samples show the strongest manifestations along the direction or dimension describing a concept in latent space. Both methods can produce different reference samples for the same filter. (*Bottom*): Each scatter plot shows two sets of 32 samples maximizing the RelMax or ActMax objective along two axes measuring their summed activation and normalized relevance values (see Appendix A.3 for details). (*Top*): The respective reference examples for  $\mathcal{X}_{8 \text{ sum}}^{* \text{rel}}$  (shaded red in scatter plots) and  $\mathcal{X}_{8 \text{ sum}}^{* \text{act}}$  (shaded blue). (*Left*): A particular channel (VGG-16, `features.26`, filter index 350) encodes for a polysemantic concept including cars and coarse patterns. Activation-based samples present cars of intense color and vegetables where the coarse pattern is dominant. The relevance-based reference samples however expose, that strong color values are not as important, and the concept seems to be centered around texture and the color gray. Further, the coarse pattern detector is mainly utilized by the model to classify alligators instead of fruits. (*Right*): For another channel and model (VGG-16 with BatchNorm layers, `features.30`, filter index 361), activation-based reference samples show thin white stripes. The stripe concept however is used to detect white letters, as relevance-based samples suggest.

**Case Study 2: Lower-Level Concepts** Differences in relevance and activation-based reference samples can also occur for lower-level concepts, as is shown in Figure 10. In this case, two filters, i.e., channels 55 and 38 located in the first layer `conv1` of a ResNet34 model trained on the Caltech-UCSD Birds 200 dataset, activate strongly for green colored inputs. However, channel 55 is relevant for yellow color detection, as is visible in the relevance-based reference sample set. For a particular sample consisting of green and yellow colored parts, activation maps show, that both channels activate strongly for “green”. However, the difference in function becomes apparent by investigating the channel-conditional relevance heatmaps. Here, the maximum value of relevance can be assigned to a green patch for channel 38 and to a yellow patch for channel 55.

Additionally, when investigating the kernel weights of the filters (see bottom of Figure 10). we see that both filters favor green inputs, represented in large weights for the green channel. Whereas channel 38 additionally strongly suppresses red colored inputs (the opposite of cyan in RGB color space), channel 55 suppresses blue color (the opposite of yellow, RGB value of yellow is (225, 255, 0)). Thus, both filters activate most strongly for green color, but channel 55 also activates strongly for yellow color — compared to channel 38 — yet inputs extremely strong in the green spectrum without red color influence can cause the activations of channel 55 to saturate, obfuscating the true purpose of the channel’s filter kernels. This is also supported by heatmaps in the very right part of Figure 10, showing which  $(7 \times 7)$ -sized input of uniform color varying in the red and green channels and matching the receptive field of the neurons of the first layer leads to the highest

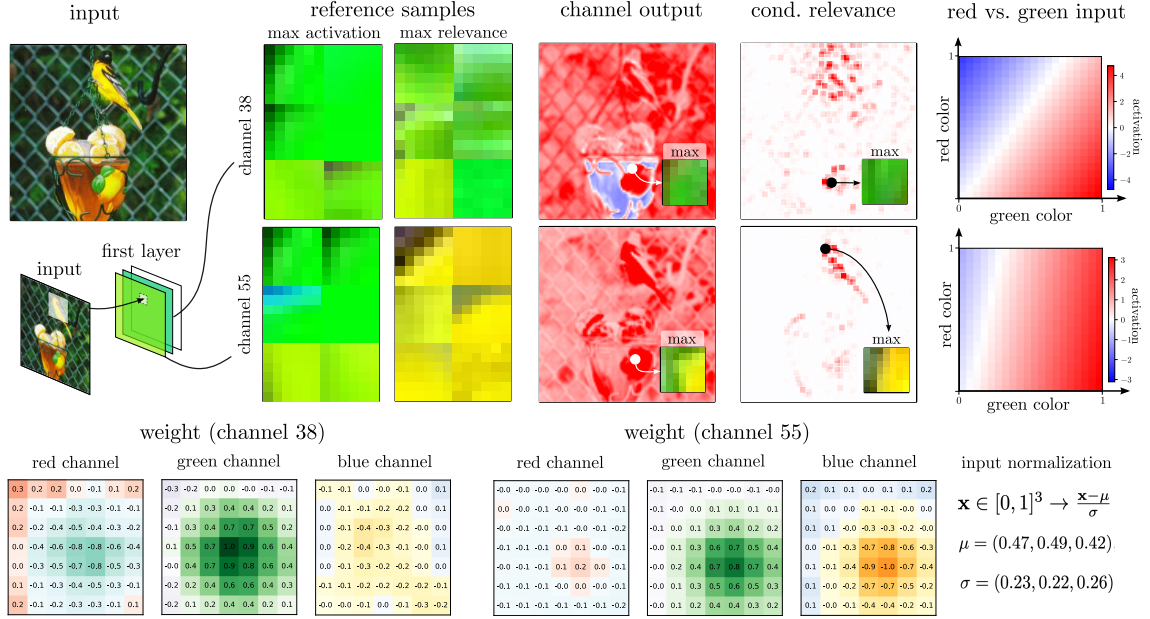


Figure 10: Difference in relevance and activation-based reference samples for low-level color concepts in the first layer of a ResNet architecture for bird classification. Two filters (55 and 38) activate strongly for green colored inputs, as activation-based reference samples and channel output maps indicate. However, one channel (55) is relevant for yellow color detection, as is visible in the relevance-based reference sample set and conditional heatmap that points to the yellow feathers of the bird. Thus, both channels activate for green color, but are used differently by the model. In the bottom, the weight values of each filter are further given, indicating which input tensors lead to a strong activation. This is also illustrated in heatmaps showing the activation values induced by red, green or a mixed-colored inputs. It is to note, that RGB inputs are first preprocessed to be in  $[0, 1]^3$  by division with value 255 and thereafter normalized with mean  $(0.47, 0.49, 0.42)$  and standard deviation  $(0.23, 0.22, 0.26)$ . Yellow in raw RGB space is  $(225, 255, 0)$ .

activation values. Strengthening red color in the input suppresses activation strongly for channel 38, whereas activation for channel 55 barely decreases.

**Case Study 3: Maximization Target Sensitivity** The previous two case studies illustrated general differences in activation and relevance-based reference sample selection. In the following, motivated by an experiment from Chen et al. [28], the influence of the maximization target, e.g., summation over the channel values or taking the maximum, on the sample sets is investigated. First, two examples are shown, and subsequently the general behavior is analyzed.

For the first example, reference sample sets  $\mathcal{X}_8^*$  for RelMax and ActMax are shown in Figure 11 (top) for different maximization targets, illustrating the concept of channel 323 in layer **features.28** of a VGG-16 network trained on ImageNet. Here, all reference sets contain images of a maritime theme except from the set  $\mathcal{X}_8^{\text{act}}$ , which mostly includes images of dog legs with long fur. A global analysis shows, that the channel’s concept is most relevant on average for the classes “reef coral”, “cramp fish”, “scuba diver”, “sea snake” and “tiger shark”. Thus,  $\mathcal{X}_8^{\text{act}}$  spuriously presents potentially misleading examples for the channel’s encoded concept.

The second example is shown in Figure 11 (bottom), depicting reference sample sets for filter channel 126 in **features.26** of the same VGG-16 network. Here, all sample sets contain images of bow or neck ties except from the set  $\mathcal{X}_8^{\text{act}}$ , which includes images depicting round shapes and orange color. Globally most relevant classes on average for this filter are “bow-tie”, “neck brace”, “suit”, “military uniform”, “academic robe” and “grenadier guards” (known from Buckingham Palace). This time,  $\mathcal{X}_8^{\text{act}}$  does not lead to clear visualizations of the concept and its examples do not align well to the contexts of the class labels for which the model is using the channel.

This observation is due to two effects: First, RelMax considers only a limited subset of samples,

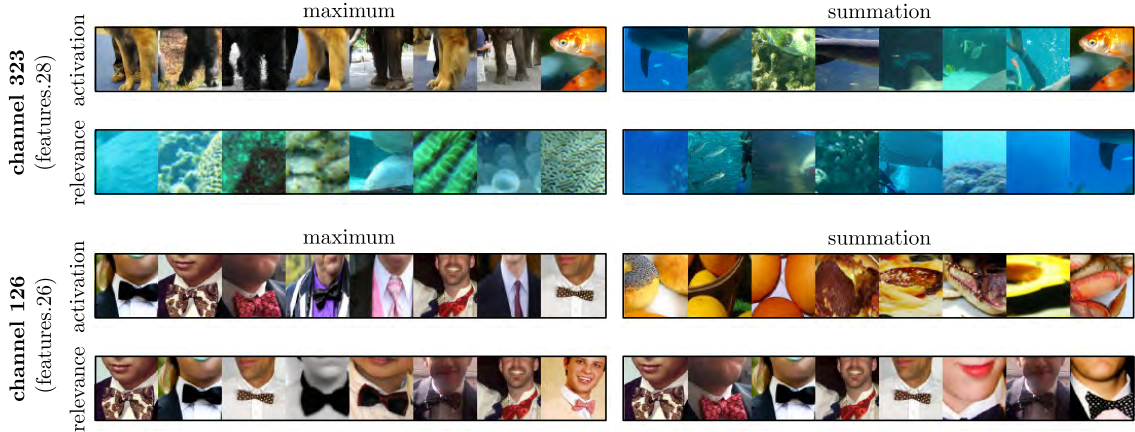


Figure 11: Reference images (cropped wrt. the receptive field of the most active/relevant neuron inside channel, see Section 2.3.4) collected using Activation Maximization and Relevance Maximization via summation, or taking the maximum, within a convolutional channel. Whereas relevance-based reference samples show similar themes, activation-based reference samples are more sensitive to the chosen maximization target. (*Top*): All reference sets contain images of a maritime theme except from  $\mathcal{X}_{s_{\max}}^{*\text{act}}$ , which mostly includes images of dog legs with long fur. (*Bottom*): All reference sets contain images of bow or neck ties except from  $\mathcal{X}_{s_{\text{sum}}}^{*\text{act}}$ , which mostly includes images of rounded shapes and orange color. See Appendix A.5 for more examples.

for which the filter was *actually helpful* for classification. Secondly, summation indirectly favors samples where the activation/relevance is spatially spread out inside the channel, as for example in images showing multiple instances of a concept, or a texture covering large parts of the input. When taking the maximum value instead of sum-aggregating, this is not the case. Since each neuron in a convolutional layer performs the same convolution operation, spatially widespread activation within the channel suggests that the pattern, for which the kernel encodes for, occurs repeatedly in the input. On the contrary, if a filter encodes for a spatially confined concept, e.g., such as a bow-tie in Figure 11 (*bottom*), then the resulting channel activation is also locally restricted (cf. Figure A.11 in the Appendix). Confusion occurs, when the concept’s size of the filter does not match the computation operation, especially when no images exist that contain multiple of these small-scale concepts. In Figure A.11 (*top*) in the Appendix,  $\mathcal{X}_{k_{\max}}^{*\text{act}}$  results in spurious edge case samples that cause spatially confined activation, although the kernel actually encodes for water texture, which is usually widespread. The opposite is the case in Figure A.11 (*bottom*) for  $\mathcal{X}_{k_{\text{sum}}}^{*\text{act}}$ . These examples illustrate, that it is generally not trivial to choose the correct calculation method for activation since a concept’s size is not known beforehand. Relevance, on the other hand, seems to be more robust against different computation modalities. An additional example can be found in the Appendix A.5.1.

Since the ranked example images have the purpose to represent *semantic* concepts, it is difficult to make a clear *quantitative* evaluation about which calculation method provides better explainability. One way to quantify the robustness of the explanations, however, is to calculate the intersection between the sets of reference images generated via summation within the convolutional channel or taking the maximum, and ActMax compared to RelMax. The greater the overlap, the more similar are the image sets. The results of the computation of the mean set similarity in layer `features.0` until `features.28` in VGG-16 are depicted in Figure 12, demonstrating that RelMax-based example sets are in general less sensitive to the choice of summation or maximization (Figure 12 (*left*)) and thus more robust, as they represent examples which are actually used by the model in a larger context. We additionally can observe that under summation, ActMax and RelMax example sets are considerably more similar than when comparing example sets which maximize their respective criterion. We attribute this to the stabilizing effect to relevance and summation computations. However, there is still a considerable difference between the respective example sets as shown by the low set intersection of less than 0.3.

Neurons in lower layers typically have a very narrow receptive field. For instance, a neuron

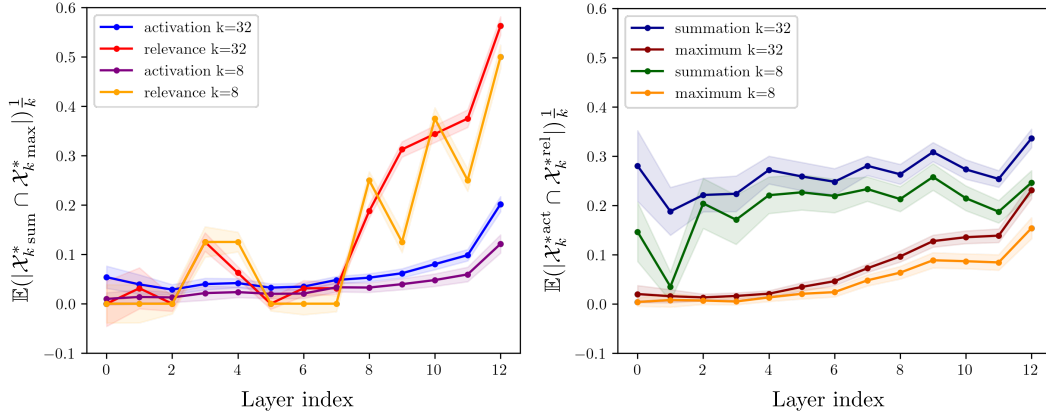


Figure 12: Mean set similarity of each filter channel per convolution layer in a VGG-16 model pretrained on ImageNet with  $k = 32$  and  $k = 8$ . The standard error of mean is overlaid with a confidence interval of 99.7 %. The layer index 0 on the x-axis corresponds to layer `features.0` and index 12 to `features.28`, since we only compare for convolutional layers with weight kernels (and ignore, e.g., pooling layers). (*Left*): Comparing the computation modality, channel-summation vs. taking the channel maximum. The plot shows that the selection of relevance-based examples is more robust wrt. the choice of maximization vs. summation of values. The low similarity in earlier layers (0-7) is due to these layer’s small receptive fields and consequently low probability of selecting same example subsets from the high number of small cropped sub-images, and not properties of Activation Maximization or Relevance Maximization. (*Right*): Fixing the choice of channel value summation or maximization as a criterion for selecting examples, we here compare ActMax to RelMax sample sets. Under summation, relevance-based and activation-based sample sets are more similar, i.e., as ActMax example sets become more robust and stable. However, there are still notable differences between the general strategies ActMax and RelMax.

may encode for “red stripes”. This concept is in almost all images present. As a consequence, the probability of finding an intersection of  $\mathcal{X}_{k \text{ sum}}^{* \text{ act}} \cap \mathcal{X}_{k \text{ max}}^{* \text{ act}}$  converges to zero due to the increased number of prospective candidate samples and low numbers of  $k$ , although, e.g., all images may show red stripes. This is due to the high number of images and the low probability of taking the same subset. This problem does not occur in higher layers. Here, for instance, a neuron encodes for “trumpets”. The number of images depicting trumpets is much smaller than images containing red stripes. If both variants illustrate “trumpets”, then an intersection between  $\mathcal{X}_{k \text{ max}}^{* \text{ act}} \cap \mathcal{X}_{k \text{ sum}}^{* \text{ act}}$  is more likely, as only a small subset of images contains this higher level concept. If both variants encode for different features, then the intersection should be empty. Finally, this computation is in all cases only an approximation.

The results suggest, that reference image sets obtained via Relevance Maximization are more robust than images obtained through Activation Maximization.

### 3.2 Handling High and Low Sample Set Variety

In general, reference samples are collected by measuring activations or attributions during model predictions sample by sample. The higher the variety in the data samples, the more abstractly can the concept be described eventually. A high feature variety is especially crucial for datasets such as, e.g., the Caltech-UCSD Birds 200 dataset with samples mostly consisting of birds. However, if reference sample variety is too high, it can also become difficult to extract the common concept. Further, for polysemantic neurons (i.e., neurons addressing multiple concepts), numerous reference samples might only describe one particular concept/facet, thus missing the other concepts. In order to find the sweet spot between too many and too few potential reference samples, two approaches are presented in the following. The first approach conditions the relevance-based reference sample set towards specific output classes in order to decrease reference set variety within each set, and at the same time better contextualize and organize the selected examples to increase interpretability.

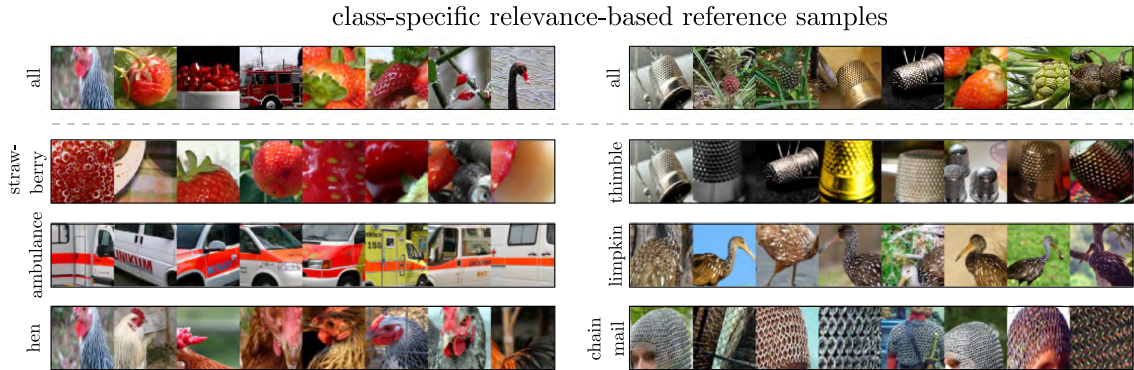


Figure 13: Relevance-based reference samples can be filtered by assessing the relevance of a concept wrt. target classes  $y$  of interest, by adequately setting Concept Relevance Propagation conditions  $\theta_y$ . (Left column:) VGG-16, filter 457 of `features.28`. (Right column:) VGG-16, filter 209 of `features.28`. (1st row): Without specifying any further conditions, reference sample sets contain the maximally relevant samples for the observed concept selected from samples of all classes and relevance scores computed for the samples’ ground truth labels. (2nd to last row): Reference example sets of the top-3 classes (sorted in descending order) for which the analyzed concept is most relevant on average. Conditioned to a specific target class, reference sample sets contain only maximally relevant samples for the concept as used in context of the class of interest. Additional results can be found in Appendix A.5.2.

The second approach briefly discusses how the reference dataset can be extended in order to increase the sample set variety, which might be of use when all originally identified most relevant examples are near identical and no (singular) common factor among the samples can be easily identified.

**Class-Conditional Reference Sample Selection** Activation-based reference sample selection for a neuron of interest only depends on the input sample and the (partially executed) forward pass until the layer of interest. While a per-class selection of activation-based reference examples is possible, this usually requires a class-specific pre-selection of the data samples under ground truth label availability [93, 53]. However, assigning a high neuron activation to a ground truth label is only sensible, if one can assume, that merely features regarding the chosen label exist in the input sample. In this case, one implicitly makes the claim, that the high activation value corresponds to a high relevance regarding the chosen class. The neuron can however respond to a different class or might be opposed to the true class, as previously discussed in Section 2.3.3.

On the other hand, using relevance-based attributions instead of activations, a pre-selection based on ground truth labels is also possible. However, in the absence of data labels, it is also feasible to condition reference samples on a class of interest by simply measuring its attribution scores from computing CRP scores wrt. the model output category of interest, regardless of the predicted label (cf. Section 2.3.3, Figure 6). Retrieving relevance-based reference samples for a particular concept, yet conditioned to different output classes of a model, will yield different class (or in extension condition  $\theta$ )-specific perspectives on the concept, i.e., how it is *actually used* by the model in context of different prediction targets. Consequently, output categories (classes) of a model can be ranked by how much they make use of the observed concept, and class-conditioned reference examples can be obtained by appropriately configuring  $\theta$  for CRP. See Appendix A.3 for details on initializing and computing of relevance.

Figure 13 (1st row) shows the top-8  $\mathcal{X}_{k \text{ sum}}^{* \text{rel}}$  reference examples for convolutional filters in `features.28` of a VGG-16 network ranked wrt. the relevance attributions obtained by computing CRP for each of the sample’s respective ground truth class. (2nd to last row) Reference examples for the respective filters are selected based class-conditional relevance scores computed for *all* samples, for each of the top-3 classes the observed filter has contributed most strongly to on average. We can observe that while in the first row all sorts of objects can appear among the selected examples which express a manifestation of a shared concept, the class variety may distract from



the identification of the core of the visualized concept. By selecting the available reference samples with regard to the classes being influenced the most from the observed concept filter, we can neatly select and organize the examples in different “perspectives” of the model.

In the left column, filter 457 is analyzed. While the first row with examples, drawn based on relevance from the product space of all samples and classes, already suggests that the color red is important, the second to the last row reveal that classes “strawberry”, “ambulance” and “hen” most prominently make use of this filter during inference, and that here, among the examples chosen based on class-conditional relevance all share red colored features such as berries, stripes or caruncles. Similarly for filter 209 analyzed in the right column, the set of examples with highly diverse class memberships is presented in context of the top-3 benefitting classes “thimble”, “limpkin” and “chain armor”. Observing all class-conditioned examples together, it immediately becomes clear that the analyzed filter encodes for a concept of regular dot-like textures.

The increase in clarity from conditionally retrieved reference examples can naturally be combined with the computation of per-example heatmap explanations, as is described in Section 2.3.5 for an exponentiated effect. Additional results for various models, and datasets, can be found in Appendix A.5.2.

**Reference Dataset Extension** To visualize concepts with reference samples, a first step is to use reference samples from the dataset used for training and validation. This set might be however limited in the manifested variety of concepts. Further, reference samples might share multiple similar concepts, making it hard to find the true common theme throughout these samples. At this point, a dataset extension can be sensible, as is shown in Figure 14. Here, two channels (10 and 130) of intermediate layer `3.0.conv2` of a ResNet34 model trained on the Caltech-UCSD Birds 200 dataset (see Appendix A.2) are investigated. As is visible in the extracted reference samples, higher-level concepts often depict whole birds having multiple common concepts. The identification of the key concept might be ambiguous in such a case, or the data might be difficult to interpret for a layman and, in this case, a non-ornithologist. Extending the reference sample set with images from ImageNet results in a higher variety of reference samples, making it easier to identify and interpret the common concepts individually. The extension then yields an alternative and additional view point on the concepts, by extending the search for concept representations in an out-of (yet related) domain dataset. Specifically, with the extended reference sample set, filter 130 can be assigned to a “dots”-texture ( $\sim 3$ px diameter). Further, channel 10 is used for “red spot” detection, as is also highlighted using channel-conditional heatmaps for the samples. It is to note, that XAI-analysis can be done on arbitrary datasets and thus mitigates potential data privacy issues affecting the applicability of our explanation approach.

### 3.3 Concept Atlas and Understanding Spatial Concept Composition

Attribution maps are ambiguous in the sense that they only show where the model is extracting useful information and not which concepts are being used. Using bird species classification as an example, input images will generally show various birds that differ in form, texture and color. Heatmaps then usually point to the head or the upper body irrespective of the bird explained, and are in this way almost identical, and not informative (see Figure 2b). At this point, in order to obtain added value from the explanation — beyond e.g., “This bird is a Red Flicker, because *just look at the whole d\*\*\*n bird!*” — and potentially derive knowledge from the model’s reasoning, it is important to know whether a particular color, texture, body part shape or relative position of the body parts led to a decision. Using traditional attribution mapping approaches, it can often only be speculated, which concepts are relevant. By visualizing intermediate neuron heatmaps via CRP, we can assist in concept understanding by localizing individual concepts in heatmaps, as well as reference samples can verify that sensible features have been learned.

Per-channel heatmaps computed through CRP describe in input space, which input features were relevant for the channel and its concept during prediction in context of an explained model output, and where those concepts are located in pixel space. We can now combine multiple concept-specific attributions in order to visualize them together in form of a “concept atlas”, motivated by the idea of an Activation Atlas from [25]. As is shown in Figure 15, the concept atlas then visualizes in input space, which concepts were most relevant (and here, second most relevant

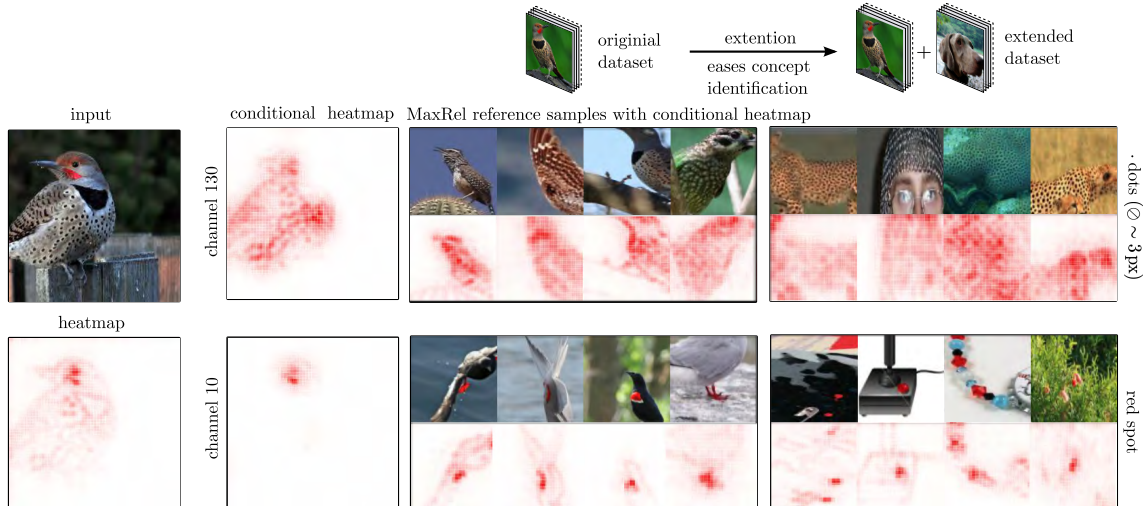


Figure 14: Extending the initial reference sample set, e.g., test and training data, with data from a different data domain can make concept understanding easier. A sample set extension yields an alternative and additional view point on the concepts. For the prediction of a “Northern Flicker”, two relevant channels (10 and 130) of `layer 3.0.bn2` (Resnet34 model) and their RelMax-based reference samples from the original Caltech-UCSD Birds 200 dataset (*left*) and with ImageNet extended dataset (*right*) are shown. It might be challenging to comprehend the concept of filters based on the original dataset alone, as image set variety may be limited: Often, birds from the same species with multiple common concepts are shown. However, with the extended reference sample set, filter 10 and 130 can more easily be assigned to “dots” ( $\odot \sim 3\text{px}$ ) and “red spot”, respectively, as only the relevant concept is shared across reference examples. It is to note, that XAI-analysis can be done on arbitrary datasets to increase potential data privacy, e.g. should the use of the original data be prohibited.

in specific input image regions. Choosing superpixels as regions of interest, we can aggregate the channel-conditional relevances per superpixel into regional relevance scores, as discussed in Section 2.2.1. Specifically, given superpixel  $k$  described by the index set  $\mathcal{I}_k$  selecting some input features, we aggregate the conditional relevance scores  $R_i^1(\mathbf{x}|\theta_c)$  for channel  $c$  and obtain  $R_{\mathcal{I}_k}^1(\mathbf{x}|\theta_c)$ , which assesses the importance of concept  $c$  in superpixel  $\mathcal{I}_k$ . All the resulting scores  $R_{\mathcal{I}_k}^1(\mathbf{x}|\theta_c)$  applying to region  $k$  can then be sorted in descending fashion for each superpixel in order to get a sorted set  $\mathcal{B}_k$

$$\mathcal{B}_k = \text{argsort}_c^{\text{desc}} R_{\mathcal{I}_k}^1(\mathbf{x}|\theta_c), \quad (26)$$

determining a regional ranking of concepts and respective importance, which can be used to construct the concept atlas. Regarding concept atlas construction, as shown in Figure 15, each channel can, e.g., be assigned a specific color for visualization purposes. Each super-pixel  $k$  is then filled with the color of the most relevant concept given by  $\mathcal{B}_k$ . The second(/third/fourth/etc.) most relevant concept defines the color of the texture/overlay (dots in our case).

So far, all super-pixels might result in a colored patch. In order to avoid distractions due to irrelevant (colored) super-pixels, we only consider super-pixels, which contain a significant portion of relevant pixels. Specifically, the threshold is chosen to be one tenth of the maximal relevance density, as described in Appendix A.4 in more detail. In the Appendix, an alternative way for constructing concept atlases using single pixels instead of super-pixels is also discussed. Here, the first and second-largest relevance scores over the channels is computed for individual pixels. The resulting regions can thereafter be color coded according to the largest and second-largest channel importance.

In Figure 15, channel heatmaps help to localize relevant regions in input space, and at the same time reveal *what* the model has picked up in those regions. Here, the concepts we identified as “red spot” and “black eyes” can be assigned to the head of the Northern Flicker bird. On the other hand, both “dots” concepts affecting the prediction can be assigned to the body/torso

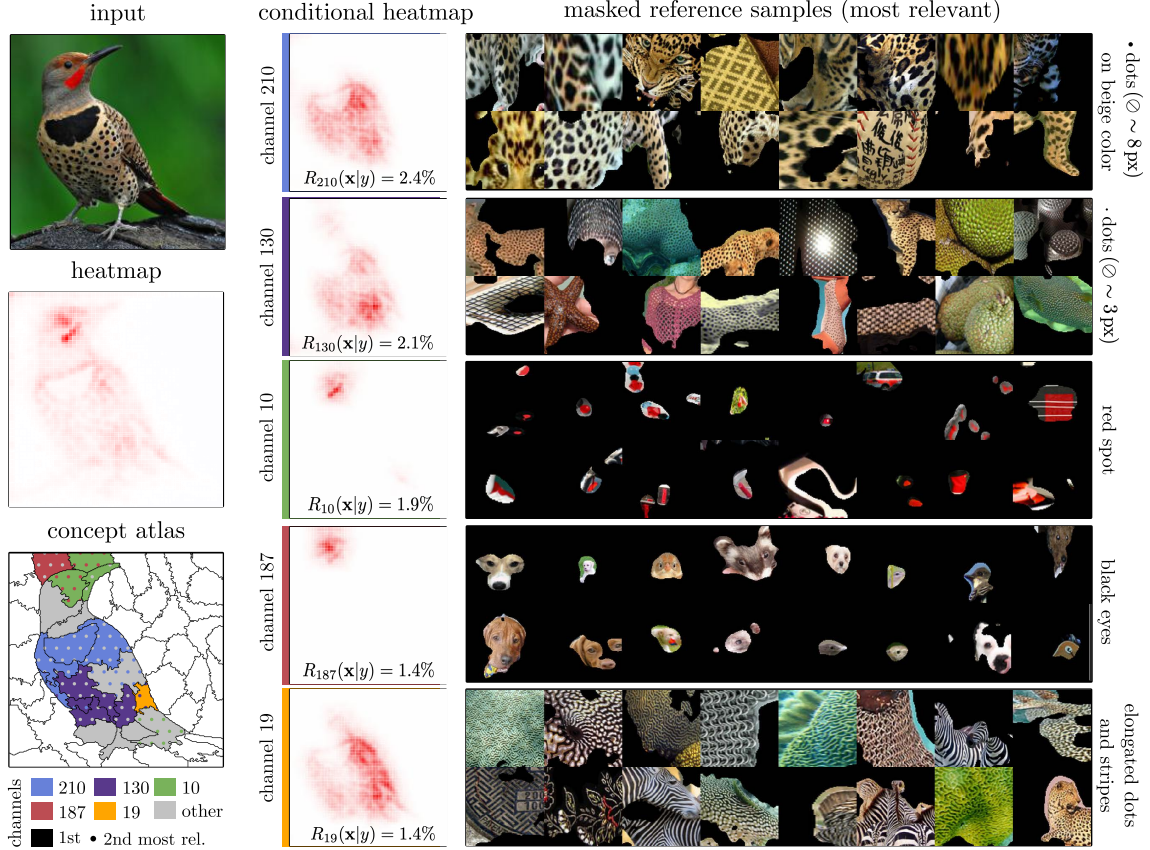


Figure 15: Channel-conditional heatmaps help to localize and understand channel concepts. CRP relevances can further be used to construct a concept atlas, visualizing which concepts dominate in specific regions in the input image defined by super-pixels. For the prediction of a “Northern Flicker” using a Resnet34 model trained on the birds dataset, the most relevant channels in layer `layer3.0.conv2` can be identified with concepts “dots” (channel 210 and 130), “red spot” (10), “black eyes” (187) and “stripes-like” (19). More examples can be found in Appendix A.4.

and “elongated dots and stripes” concept to the bird’s wings. The Concept Atlas further eases to comprehend where in input space which concept dominates. Here, the concept atlas also indicates a stripe of red color in the tail feathers of the bird, by the “red spot” concept being most relevant in this region.

Generally, the meaningful aggregation of relevances allows locally investigating and comparing the most relevant channels or concepts inside different chosen image regions. These regions might depict completely unrelated visual features individually, as is shown in Figure 16. While concept atlases explain the model’s reasoning in a top-down manner, i.e., via the identification and localization of relevant concepts, localized analyses can serve a complementary purpose: By specifying input regions of interest, we can ask the model which particular features it has been influenced by within a constrained set of input dimensions.

Here, the top-3 most relevant channels for two superpixels in the sorted set  $\mathcal{B}_k$  are visualized for a local analysis. In this example, a stork from the ImageNet dataset is classified using a ResNet34 model. One superpixel contains the stork’s beak, the other superpixel the stork’s right wing. Regarding the beak in  $\mathcal{I}_1$ , the top-3 most relevant channels located in layer `layer3.0.conv2` focus on color (“orange”, “red” and “yellow”). Regarding the wing in  $\mathcal{I}_2$  on the other hand, the most relevant channels focus on textures, such as “diverging stripes”, “lined” or “dark curves”.

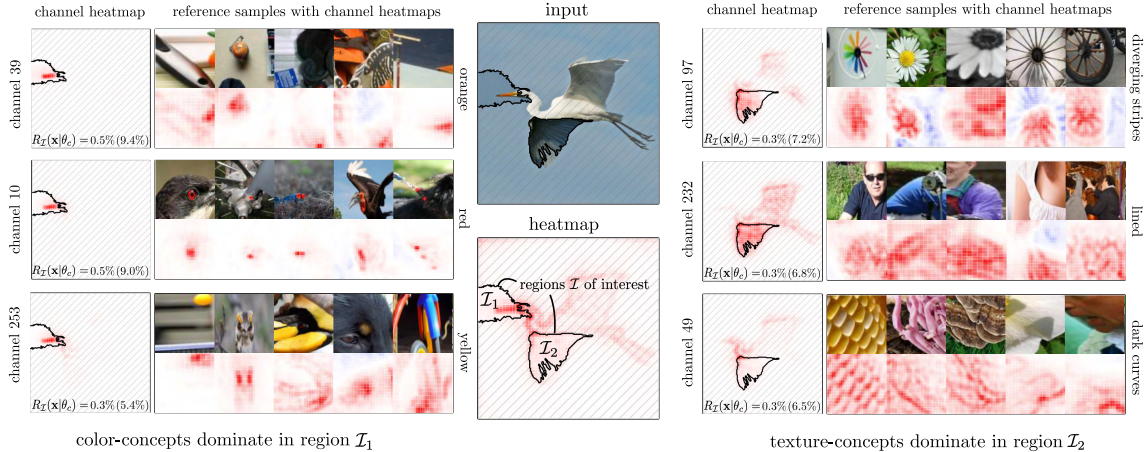


Figure 16: Relevance aggregation inside superpixels allows investigating the locally most relevant channels for chosen regions of interest  $\mathcal{I}_k$ . The top-3 most relevant channels for the prediction of class “stork” regarding two superpixels are shown with channel heatmaps and reference samples. (*Left*): Region  $\mathcal{I}_1$  covers the stork’s beak. Here, color-concepts, such as “orange”, “red” and “yellow” are most relevant. For each channel, the relevance relative to the global relevance as well as superpixel relevance (in parentheses) is given. (*Right*): Region  $\mathcal{I}_2$  covers the stork’s right wing. Here, texture-concepts, such as “diverging stripes”, “lined” and “contrastive curve/bend” are most relevant. More examples can be found in Appendix A.4.

### 3.4 Understanding Hierarchical Concept Composition

With the selection of a specific neuron or concept, Concept Relevance Propagation allows to investigate, how relevance flows from and through the chosen network unit to lower-level neurons and concepts, as is discussed in Section 2.2.1. This gives information about which lower-level concepts carry importance for the concept of interest and how it is composed of more elementary conceptual building blocks, which may further improve the understanding of the investigated concept and model as a whole. In Figure 17, we visualize and analyze the backward flow of relevance scores. The graph-like visualization reveals how concepts in higher layers are composed of lower layer concepts. Here, we show the top-2 concepts influencing our concept of choice, the “animal on branch” concept encoded in `features.28` of a VGG-16 model trained on ImageNet. Edges in red color indicate the flow of relevance wrt. to the particular sample from class “Bee Eater” shown to the very right between the visualized filters with corresponding examples and (multi)-conditional heatmaps. The width of each red edge describes the relative strength of contribution of lower layer concepts to their upper layer neighbors.

The conditional relevance  $R^l(\mathbf{x}|\theta = \{l : \{c_0\}\})$  for a concept  $c_0$  (“animal on branch” in Figure 17) in layer  $l$  can be propagated layer by layer until the input space is reached. At each lower-level layer, the computed attribution scores of neurons and filters then describe their respective relevance to the concept  $c_0$  for the prediction on  $\mathbf{x}$ . Now, the top  $k$  filters at each layer can be illustrated. While this approach depicts the layer-wise contribution to concept  $c_0$ , no disentanglement in lower layers is achieved as the relevance in layers lower than  $l - 1$  is sum-aggregated together and no accurate hierarchical flow of relevance is obtained, which, however, is possible in principle via the evaluation of multiple backward passes specifically conditioned to lower-layer concepts. Precisely, it is not possible to obtain the sole contribution of a concept  $c_i$  in layer  $l - 2$  to a concept in layer  $l - 1$  in a single backward pass.

To disentangle the attribution graph, we expand on  $\theta$  and mask each of the top  $k$  filters in the previous layer independently with an additional backward pass. At layer  $l$  we set  $\theta = \{l : \{c_0\}\}$  and compute an attribution until layer  $l - 1$ . At  $l - 1$  we iterate over the  $k$  most important units and set  $\theta = \{l : \{c_0\}, l - 1 : \{c_1\}, \dots, l - 1 : \{c_k\}\}$ . We repeat the steps outlined above for each layer. This way, each lower level concept can be broken down independently and an accurate hierarchical representation achieved.

To illustrate the resulting graph, we visualized an attribution flow for filter 102 in layer

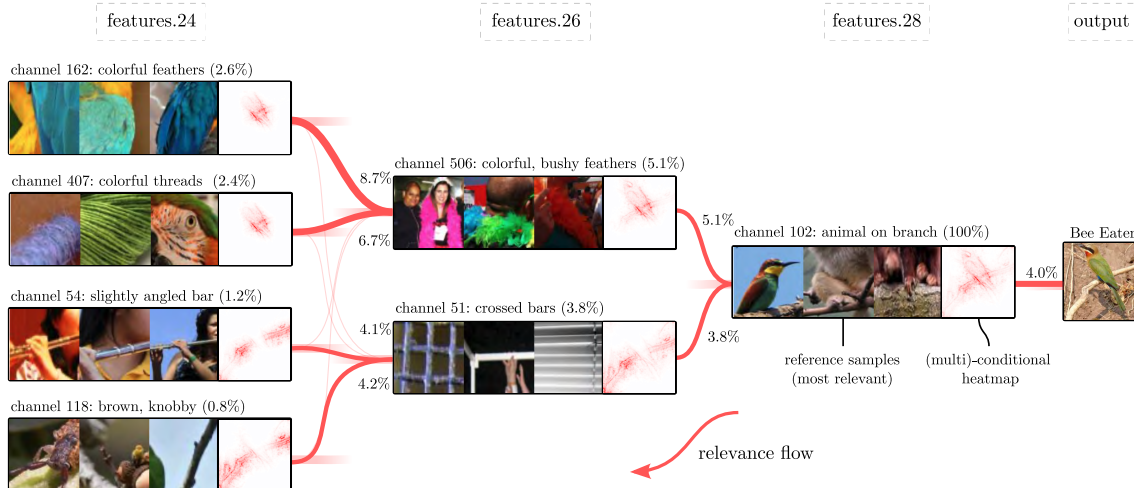


Figure 17: Attribution Graphs can be used to visualize relevant concepts in lower layers for a concept of interest regarding a particular prediction outcome, and thus improves concept understanding. Shown are relevant (sub)-concepts in `features.24` and `features.26` for concept “animal on branch” in `features.28` of a VGG-16 model trained on ImageNet for the prediction of class “Bee Eater”. The relevance flow is highlighted in red, with the relative percentage of relevance given that flows to the lower-level concept. For each concept, the channel is given with the relative overall relevance score (wrt. channel 102 in `features.28`) in parentheses. Following the relevance flow, concept “animal on branch” is dependent on concepts describing the branch (e.g., “slightly angled bar” and “brown, knobby”) and colorful plumage (e.g., “colorful feathers” and “colorful threads”). Another example is shown in Appendix A.4.

`features.28` of a VGG-16 model trained on ImageNet given an example image  $\mathbf{x}$  showing an instance from the “Bee Eater” class. The filter is specialized in detecting animals sitting on tree branches. This example shows that different paths in the network potentially activate the filter. In the case of the upper bird, concepts that encode feathers and horizontal structures are responsible for the activation of filter 102 in the observed layer. Here, path-specific conditional heatmaps illustrate how the sub-concepts either target the branch or the bird’s plumage. In summary, we are able to visualize how abstract concepts arise from low-level patterns, and how they are composed specifically to the prediction for which the flow of relevance has been computed for.

### 3.5 Concept Analysis on Time Series Data

The application of XAI is not constrained to the image domain and has, in the past, seen utilization in numerous other data domains [112]. For instance, DNNs are trained to predict chemical properties on molecular fingerprints, encoding the atomic substructure, in order to develop new drugs [99]. Further, vectorized geospatial fields are investigated for the identification of climate patterns in the geosciences [132] and finally, but not exhaustively, attributions on regression models guide human intuition in finding new mathematical theorems [34]. In all these settings, as long as the data domain can be meaningfully visualized in an interpretable way, obtaining concept-based explanations with CRP is possible.

Here, we present a use-case, on how CRP can be utilized in a CNN model trained on Electrocardiography (ECG) arrhythmia data to verify the concepts used during inference and to open up the door to potential use-cases for scientific discovery in the future.

A decisive factor for interpretability is choosing the right representation for the input domain. For example in gender classification on voice recordings a frequency representation is more advantageous in terms of XAI interpretability since here, pitches are easier to distinguish for the naked eye [17], than in time domain. For ECG data, the traditional time series representation is much more comprehensible for physicians, because they are familiar with this visualization on which characteristic markers have been defined in literature [77]. The original training data is provided

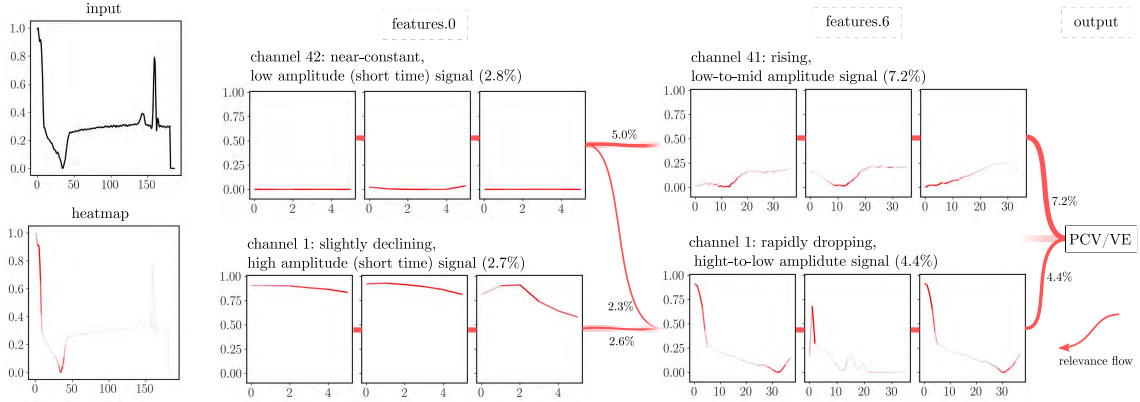


Figure 18: Glocal analysis of ECG time series data. The heatmap of the signal indicates, that the strong decline in the beginning and slight rebound in signal thereafter are the main elements the model is focusing on. Investigating individual layers with their channels, specific relevant units can be identified with concepts corresponding either to the strong drop or rebound. Specifically, in the lower layer `features.0` channel 42 encodes for low signal amplitudes, whereas channel 1 represents high amplitude signals. Further, each channel is relevant for channels with concepts “low, rising signal” (41) and “highly peaking signal” (1) in the higher level layer `features.6`. The concept composition is illustrated by the relevance flow in the form of an attribution graph.

by PhysioNet MIT-BIH Arrhythmia [85] and consists of ECG recordings from 47 different subjects, where each beat was annotated by at least two cardiologists. The work [58] reordered the dataset by isolating the ECG lead II data, splitting and padding beats into a fixed size of 150 at a sampling rate of 125 Hz and finally grouping all annotations into five different categories in accordance with the *Association for the Advancement of Medical Instrumentation* (AAMI) EC57 standard [41].

We train a model containing multiple layers of 1D-convolutional and densely connected layers. Details on the architecture and training procedure can be found in Appendix A.2. Assuming concepts are confined to single channels, we visualize again only single filters using RelMax. The attribution maps are projected to the input data domain and visualized as line plots. Similar to the image domain setting in Section 2.3.4, we infer the receptive field at the hidden layers in order to identify and crop the most representative signal patterns for individual filters. In the future, this visual representation could be augmented by symbolic regression or other more precise mathematical descriptors of the concepts such as the Romhilt-Estes score system [37].

The input sequence in Figure 18 depicts the end of a premature ventricular contraction (PVC) or ventricular escape beat that was successfully detected by the model. A PVC is characterized by a wide QRS complex accompanied by a left bundle-branch block pattern. In this case, a tall R wave and negative S wave, respectively, a high amplitude value followed by a valley is indicative [48, 2]. Investigating the concepts most relevant for classification, we perform two local analyses on two regions of interest. We can see that the filters used by the model correspond to the input pattern at the chosen region. The attribution graph, depicting the relevance flow from higher layer concepts in layer `features.6` to lower level concepts in layer `features.0`, illustrates how filter 1 is composed of two concepts corresponding at one hand to the upper decline and secondly to the low voltage valley. Channel 41 in `features.6`, responsible for detecting a high amplitude followed by a valley, is most relevant for the PVC category on average, indicating that the model correctly identified the distinctiveness of a PVC<sup>8</sup>. In the same way, XAI has the potential to be used for scientific discovery, e.g., for revealing previously unknown characteristics of known phenomena [34, 99, 132]. However, the filter corresponds only to 4.4 % of total absolute relevance representing a fraction of the decision process. In summary, we demonstrated the applicability to data in non-image-domains and we have taken the first steps towards testing models for plausibility and scientific discovery. Nevertheless, the concept representation should be optimized even further in future.

<sup>8</sup>Time dependency between beats plays also a role that is not apparent from the shown visualization.

## 4 Experiments II: Clever Hans Detection and Quantitative Results

In the previous section, we have qualitatively demonstrated the capabilities of our method for explaining machine learning predictions not only in terms of involved concepts, but also how those predictions can be broken down into corresponding concept-specific explanations again, and how this information may be visualized for exploring machine learning models and datasets. In the following, we will move forward by showcasing how our achieved level of explainability may be used to interact with the model, e.g., by second-guessing its decision based on the features it has used, as revealed by Concept Relevance Propagation and its example-based explanations. First, starting with Section 4.1 we give an answer to the question of *how many* concepts need to be observed and understood in order to comprehend a particular model decision given the hundreds of filters potentially encoding unique abstractions<sup>9</sup>. This set of relevant concepts then allows for, e.g., entering a dialogue with the predictor and for asking “what-if” questions regarding its decision-making strategies. In Section 4.2, we then investigate how a model trained on the ISIC 2019 skin lesion analysis dataset [30, 29, 133] reacts to the presence of clinically irrelevant concepts which have been discovered to be learned. In Section 4.3 we show how our method can be used to first discover spuriously interesting (Clever Hans) concepts learned by the model, and then perform an explainability-based image retrieval in order to identify multiple classes affected by the same image artifact semantically, which however should be unrelated to the target labels. Finally, in Section 4.4 we analyze the latent representations of relevance-based reference example sets and thus are able to identify sets of filters correlating in terms of activation, but differ in relevance for the purpose of encoding detailed differences between conceptually related ImageNet classes.

### 4.1 Quantifying the Foundation of Decision Making

In the previous sections, we have so far shown only a very limited amount of the most relevant concepts and examples as identified via relevance scores. For one, this is due to the static nature of this manuscript and its associated limitations<sup>10</sup>. More importantly, with the usually high number of layers within an analyzed network and the hundreds of filters per layer, an exhaustive presentation of all explainability data per inference might quickly become overburdening to the observer. With those practical limitations in mind, we want to address the question of *how much* explanation is needed in order to sufficiently understand a particular inference of the model.

Recent work on network compression and pruning has shown that contemporary neural network architectures often are highly over-parameterized and a large amount of filters can be removed without noticeable impact on the performance of the model [146, 144, 18]. The explicit representation of prototypes in some neural network architectures [27] has been exploited to remove spurious information from the decision making in a user-interactive fashion [42]. Based on this, we may assume that there exist neurons and filters which encode information irrelevant to a particular inference under analysis. To measure the extent of the (ir)relevance of explained and interpretable network elements, we perform an experiment based on the perturbation of a latent layer’s filters in accordance to their relevance scores, similar to the evaluation based on input perturbation described in [111]. We show that a large part of filters have indeed no impact on individual predictions, and only a small fraction of the available filters per layer do have a significant impact in favor or against the prediction made by the model, which need to be observed in order to understand the model’s reasoning.

Specifically, for a particular prediction we start with the computation of relevance scores, which are assigned to all layers, filters, and neurons of the model. Within a layer to be evaluated, we first rank the filters according to their (spatially sum-aggregated) relevance. Then, according to this ranking, we successively deactivate the filters in descending order (i.e., deactivating the most relevant representations first) by setting their activations to zero, and re-evaluate the model output. Since the initial output logits differ for each data sample, values are measured relative to the initial confidence values of the observed and explained model output. We refer to this process

<sup>9</sup>Fortunately, the answer is “not that many”!

<sup>10</sup>Which arguably could be alleviated with interactive analysis tools, which are, at time of submission, under active development.

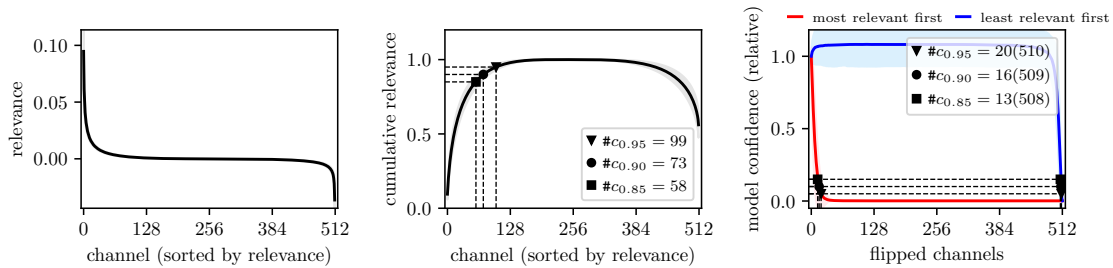


Figure 19: We evaluate the distribution of relevance and relevant filters in `features.28` of a VGG-16 model trained on ImageNet, averaged over 250 randomly drawn example images. Only a fraction of all 512 filter channels is relevant for classification predictions. (*Left*): Relevance (relatively scaled to the sum of positive relevances) is power-law distributed across the channels of the observed layer. (*Center*): Cumulative relevance distribution with markers showing that on average 58, 74 and 100 channels are necessary to explain any prediction up to 85 %, 90 %, or 95 % in terms of cumulated relevance, respectively. (*Right*): The activations of filters with the most positive (red line) and negative (blue line) attributed relevance are deactivated successively and the model is reevaluated. After 14, 16, or 20 filters inactive, the output confidence (normalized to the initial output value) has decreased by 85 %, 90 %, or 95 %. Compared to the number of the for the prediction cumulatively relevant filters, a significantly smaller number of the most relevant filters needs removed in order to change the prediction outcome significantly. In contrast, flipping the least relevant channels first, the model remains confident even if the majority (up to 508, 509 or 510) of filters are removed. Only until the last four, three or two filters are flipped, the model confidence drops below 15 %, 10 % or 5 %, respectively. For all plots, the mean curve is displayed in opaque color and standard error of mean with transparent color. The flipping experiment is restricted to confident predictions (softmax probability above 50 %), so that neurons encode meaningful information. Additional examples for further layers are shown in Appendix A.16.

as “filter flipping” in accordance to the designation of “pixel flipping” from [11]. This procedure measures the impact a set of perturbed filters has on the decision outcome, and whether their relevance-based ranking is indicative of the model’s use of the therein encoded information during inference. The same procedure is repeated with an inverted filter ranking, i.e., perturbing the least relevant filters (potentially being relevant against the initial prediction outcome) first. Note that deactivating filters with negative relevance scores usually increases the prediction confidence, since negative relevance argues against the selected class, and removing them indirectly reinforces evidence for the selected class.

Figure 19 (*left*) shows the distribution of ranked relevance scores per filter (averaged over 250 randomly drawn samples) within `features.28` of a VGG-16 model, and Figure 19 (*center*) the average cumulative sum of relevance over the rankings. Note that relevance scores attributed to filters tend to be power-law distributed, which holds true for both strong positive attributions, and strong negative attributions. This means that (on average) only a minority of filters are involved in per-sample inference, both in support and contradictory to the prediction outcome. In Figure 19 (*center*) we can see that in order to observe 85 %, 90 %, or 95 % of the foundation of the model’s reasoning *speaking for* its prediction outcome (measured in terms of cumulative relevance), the stakeholder has to investigate and understand the concepts of the 58, 74 and 100 most important filters, respectively. Approximately 300 of the 512 filters in layer `features.28` are not involved in predictions on average.

While having to look at “only” approx. 20% (which still are 100) of the layer’s filters to understand 95 % of the most relevant filters might indicate a high stakeholder workload, the results of the filter flipping experiment in Figure 19 (*right*) do showcase that effectively, an even smaller fraction of the most relevant filters is *responsible* for the model’s decision confidence: We measured that in order to decrease the output confidence of the model relatively by 85 %, 90 %, or 95 % it is on average sufficient to deactivate only the 14, 16 or 20 most relevant filters, respectively.

We conclude that it is therefore possible to understand (or at least obtain a thorough overview



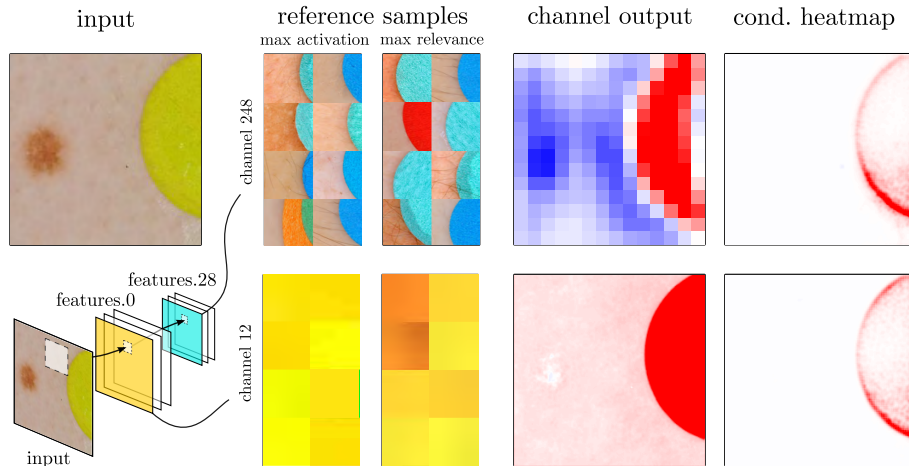


Figure 20: Glocal analysis shows that concepts relevant for “band-aid” are used for lesion classification in the ISIC dataset. Specifically, a higher-level channel (index 248) for “colorful band-aid” in `features.28` (*top*) and a lower-level channel (index 12) for “yellow” (*bottom*) can be identified in `features.0`. The activation maps as well as channel relevance heatmaps of the shown sample support the finding locally. In this particular case, both channels are the most relevant channels of their respective layer.

about) the reasoning of the model in context of a particular sample by considering only a small fraction of all filters, since only the most important filters have a noticeable influence on the outcome. Further, it is to note that for simplicity, we assume in this study, that each filter encodes a learned concept on its own. This assumption will in general not hold, with multiple filters redundantly or in combination encoding highly similar or compound concepts in practice. A meaningful grouping or clustering of filters (see Section 4.4 for an outlook) can therefore further ease the task of interpreting machine learning explanations.

For ResNet-like architectures, it should additionally be taken into account that relevance may be distributed unevenly among layers due to short-cut connections (see Appendix A.6 for further details).

## 4.2 Investigating the Impact of (Clever Hans) Concepts

The methods proposed in this study allow to explore learned concepts and investigate their role in the decision process. Knowing which concepts exist allows to manipulate and test decisions. In the previous section, concepts are suppressed without taking their semantic meaning into account, and by setting whole activation maps to zero. In the following, we first insert and secondly replace distinct concepts in order to manipulate decisions. Specifically, we present two examples for the ISIC lesion classification task [133, 29, 30]. Here, different skin samples are classified into the diagnostic classes of melanoma (MEL), melanocytic nevus (NV), basal cell carcinoma (BCC), actinic keratosis (AK), benign keratosis (BKL), dermatofibroma (DF), vascular lesion (VASC), squamous cell carcinoma (SCC) and unknown (UNK). Using our approach, we are able to identify the filters responsible for encoding colorful band-aids polluting a significant fraction of the available samples [108], which is known to impact the inference of models trained on the dataset [6].

A glocal analysis shows that a VGG-16 model trained on the ISIC dataset has learned to use a band-aid concept for lesion detection. Locally, a higher-level channel (filter index 248 in `features.28`) for “colorful band-aid” and a lower-level channel (filter index 12 in `features.0`) for “yellow” can be identified and associated to the concepts, as is depicted in Figure 20. The channel activation maps, as well as channel relevance heatmaps of the given sample support the finding, by consisting of large values in the spatial region of the band-aid. Further, these channels are most relevant for the decision, suggesting the identification of the source of Clever Hans behavior tied to these filters.

In the first experiment, the Clever Hans — i.e., the “band-aid” — concept, is inserted into 160

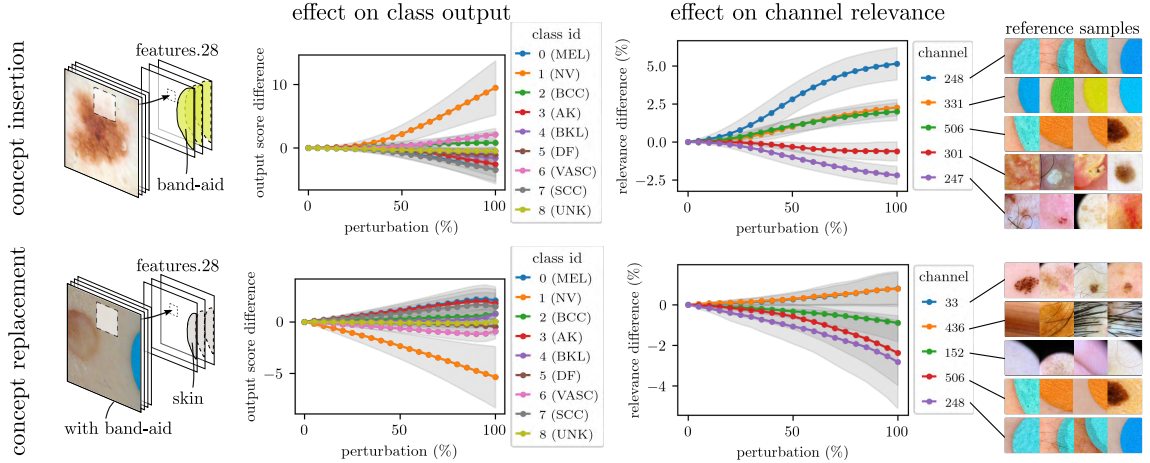


Figure 21: A systematic evaluation of the impact of the “band-aid” concept to model behavior. The band-aid is inserted (*top*) or replaced (*bottom*) in the prediction process at layer `features.28`. The manipulation is performed by linearly alpha-blending the replacement features locally into the target image, and the mean change in class output as well as channel relevance is recorded. While inserting a “band-aid” concept in the latent space, the output score for the benign class 1 (NV) increases most strongly (*top left*). Further, relevance scores for channels supporting band-aid concepts increase (*top right*). The gradual removal of the “band-aid” concept, results in an opposite effect: The output score of class 1 decreases (*bottom left*) and channels supporting “band-aid” are decreasing in relevance as well (*bottom right*). In all plots, the standard deviation is highlighted in gray color.

randomly drawn sample images which do not show band-aids. As shown in Figure 21 (*top*), the “band-aid” expression is inserted in the prediction process via the higher-level layer `features.28` (see Appendix A.7 for further variations of the experiment). To this end, the activation tensors are copied from a sample with a band-aid features to a sample without band-aid features. In order to only copy activations describing the band-aid concept, all activations are masked to overlap with the band-aid in the spatial dimension and then transferred to the target sample.

Specifically, the activations  $\mathbf{Z}_m^l \in \mathbf{R}^{c \times w \times h}$  (located in layer  $l$  consisting of  $c$  channels with spatial dimensions of size  $w$  and  $h$ ) for prediction of sample  $m$  without a band-aid are replaced with activations  $\mathbf{Z}_p^l$  from sample  $p$  with a band-aid as

$$\mathbf{Z}_m^l \rightarrow \mathbf{Z}_m^l \circ \overline{\mathbf{M}}_p + \mathbf{Z}_p^l \circ \mathbf{M}_p \quad (27)$$

with the Hadamard product  $\circ$  and the mask  $\mathbf{M}_p = 1 - \overline{\mathbf{M}}_p$  that spatially localizes the band-aid with values of one and zero else. The manipulation of  $\mathbf{Z}_m^l$  can also be done gradually, controlled with parameter  $\alpha \in [0, 1]$ :

$$\mathbf{Z}_m^l(\alpha) = \mathbf{Z}_m^l + \alpha \mathbf{M}_p \circ (\mathbf{Z}_p^l - \mathbf{Z}_m^l) , \quad (28)$$

where  $\alpha$  controls the degree of localized blending in the band-aid expression. Performing the perturbation linearly, the change in class output as well as relevance for the top-5 strongest changing channels is depicted in Figure 21 (*top*). For each channel, the four most relevant reference samples are shown. As is visible in the plots, a mean increase in output score for class 1 can be seen for band-aid insertion. The output score for class 0 most strongly decreases. This can in fact lead to a change in prediction outcome, as is shown in Appendix Figure A.18. Tracking relevance values of the individual channels shows, that channels with concepts supporting “band-aid” are growing in relevance with increasing perturbation. Specifically, channels with indices 248, 506 and 331 (activating for band-aids) receive more relevance on average when the band-aid concept is added.

In the second example, the “band-aid” concept is replaced in 25 band-aid-containing samples by a “skin” concept from a sample solely depicting skin. The manipulation is again performed in the higher-level layer `features.28`, as shown in Figure 21 (*bottom*). Please refer to Figure A.19



Figure 22: Local analysis on the attribution map reveals several channels (454, 361, 204, 414, 486, 443 and more) in layer `features.30` of a VGG-16 BN model pretrained on ImageNet that encode for a Clever Hans feature exploited by the model to detect the safe class. (*Left*): Input image and heatmap. (*Center*): Reference samples  $\mathcal{X}_s^{*rel}$  for the 6 most relevant channels in the selected region in descending order of their relevance contribution. (*Right*): Relevance contribution of the 20 most relevant filters inside the region. These filters are successively set to zero and the change in prediction confidence of different classes is recorded.

in the Appendix for applications of the process to different layers. Regarding the skin concept, activations are averaged over the spatial dimension for the skin-only input image. Thereafter, these activations replace the latent space features during predictions defined by a mask covering the band-aid.

Specifically, the activations  $\mathbf{Z}_p^l$  for the sample  $p$  with a band-aid are gradually replaced with spatially averaged activations  $\bar{\mathbf{Z}}_s^l$  from a sample  $s$  consisting of skin concept using parameter  $\alpha$  as

$$\mathbf{Z}_p^l(\alpha) = \mathbf{Z}_p^l + \alpha \mathbf{M}_p \circ (\bar{\mathbf{Z}}_s^l - \mathbf{Z}_p^l) \quad (29)$$

where  $\alpha$  controls the degree of blending in the skin expression and mask  $\mathbf{M}_p$  localizing the band-aid spatially with values of ones and zeros else.

As is visible in the plots of Figure 21 (*bottom*), the replacement of the band-aid concept leads to a decrease in prediction output for class 1. This manipulation again can lead to a change in prediction outcome, as is shown in Appendix Figure A.19. A decrease in the score for class 1 is expected, as in the first experiment the opposite happened when concept “band-aid” is inserted.

Investigating the change in relevance of individual channels, we can see, that channels supporting a “band-aid” concept are decreasing in relevance. Channels such as (e.g., 248, 506 and 152), that previously gained relevance when “band-aid” was added, now lose relevance when the band-aid concept is replaced.

### 4.3 Explanation-based Image Retrieval for Clever Hans Assessment Beyond Class Boundaries

In this section, we demonstrate how Concept Relevance Propagation can be leveraged as a Human in the Loop (HITL) solution for dataset analysis. In a first step, we will uncover another Clever Hans (CH) artifact, suppress it by selectively eliminating the most relevant concepts in order to assess its decisiveness for the recognition of the correct class of a particular data sample, similarly as in the previous section. Then, we utilize class-conditional reference sampling (cf. Section 3.2) to perform an inverse search to identify multiple classes making use of the filter encoding associated concept, both in a benign and a Clever Hans sense.

In Figure 22 we analyze a sample of the “safe” class of ImageNet in a pretrained VGG-16 BN model. Initially, we obtain an input attribution map highlighting a centered horizontal band of the image, where a watermark is located. If we take a closer look at layer `features.30` and perform a local analysis (cf. Section 2.2.1) on the watermark, we notice that the five most relevant filters are

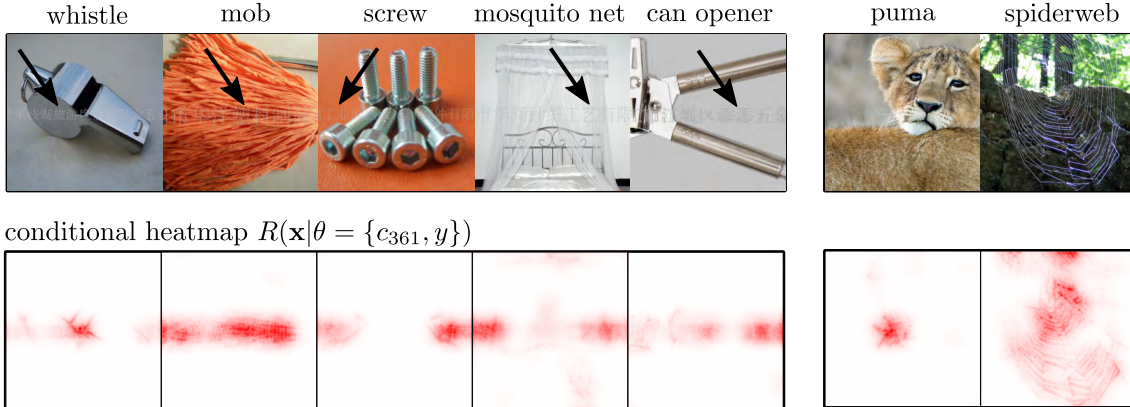


Figure 23: The Clever Hans filter 361 in layer `features.30` of a VGG-16 model with BatchNorm pretrained on ImageNet activates on samples of different classes (most relevant reference samples shown). Here, black arrows point to the location of a CH artifact, i.e., a white, delicate font overlaid on images (best to be seen in a digital format). In the case of class “puma” or “spiderweb”, the channel activates on the puma’s whiskers or the web itself, respectively. Below the reference samples, the CRP heatmaps conditioned on filter 361 illustrate, which part of the attribution map results from filter 361.

454, 361, 203, 414 and 486. Visualizing them using ActMax as illustrated in Appendix A.22, we conclude that they approximately encode for white strokes. Using RelMax instead (as shown in Figure 22, we gain a deeper insight into the model’s preferred usage and discover that the model utilizes the filters to detect white strokes in *written characters*.

To test the robustness of the model against the Clever Hans artifact, we successively set the activation output map of the 20 most relevant filters activating on the watermark to zero. In Figure 22 (right), we record the decline of classification confidence of four classes with the highest prediction confidence for this sample. From the graph, it can be inferred that the Clever Hans filters help the model in prediction, but they are not decisive for correct classification. Thus, the model relies on other potential non-Clever Hans features to detect the safe verifying the correct functioning of the model in cases of samples without watermarks. Another example with strong dependency on Clever Hans artifacts is found in Appendix A.21.

In an inverse search, we can now explore for which samples and classes these filters also generate high relevance. This allows us to understand the behavior of the filter in more detail and to find other possible contaminated classes. In Figure 23 are the seven most relevant classes for filter 361 illustrated. Surprisingly, many classes including “whistle”, “mob”, “screw”, “mosquito net”, “can opener” and “safe” (among others) in the ImageNet Challenge 2014 data are contaminated with similar watermarks encoded via filter 361 of `features.30` which is used for the correct prediction of samples from those classes. To verify our finding, we locate via CRP the source of the filters’ relevance wrt. the true classes in input space, and confirm that these filters indeed activate on the characters. This implies that the model has learned a shared Clever Hans artifact spanning over multiple classes to achieve higher accuracy in classification. The high number of contamination of samples with the identified artifactual feature could be explained by the fact, that watermarks are sometimes difficult to see with the naked eye (location marked with a black arrow) and thus slip any quality ensuring data inspection. The impact of this image characteristic can, however, be clearly marked using the CRP heatmap. Although the filter is mainly used to detect characters, there are also valid use cases for the model, such as for the puma’s whiskers or the spider’s web. This suggests that the complete removal of Clever Hans concepts through pruning may harm the model in its ability to predict other classes which make valid use of the filter, and that a class-specific correction [6] might be more appropriate.

## 4.4 Assessing Concept Similarity in Latent Space

So far in our experiments throughout Section 3 we have treated single filters as functions assumed to (fully) encode learned concepts. Consequently we have visualized examples and quantified effects based on per-filter granularity. While previous work and our own experiments suggest that individual neurons or filters *mostly* encode for a single human comprehensible concepts [148, 94, 102, 16, 24, 44]<sup>11</sup>, it can generally be assumed, that concepts are encoded by sets of filters: The learned weights of potentially multiple filters might correlate and thus redundantly encode the same concept, or the directions described by several filters situated in the same layer might span a concept-defining subspace [135]. Our proposed Concept Relevance Propagation readily supports the definition of concepts as sets of multiple features, as outlined in Section 2.2.

In this section, we now aim to investigate the encodings of filters of a given neural network layer for similarities in terms of activation and use within the model. For this purpose we present a simple but qualitatively effective method for grouping similar concepts in CNN layers: Based on the notation in previous sections,  $\mathcal{X}_{(k,q)}^*$  denotes a set of  $k$  reference images for a channel  $q$  in layer  $l$  and  $\mathbf{z}_q^l(\mathbf{W}, \mathbf{x}_m)$  the ReLU-activated outputs of channel  $q$  in layer  $l$  for a given input sample  $\mathbf{x}_m$  and all required network parameters  $\mathbf{W}$  for its computation. Specifically, for each channel  $q$  and its associated full-sized (i.e. *not* cropped to the channels’ filters’ receptive fields) reference samples  $\mathbf{x}_m \in \mathcal{X}_{40,q_{\text{sum}}}^{\text{rel}}$  we compute  $\mathbf{z}_m^q = \mathbf{z}_q^l(\mathbf{W}, \mathbf{x}_m)$ , as well as  $\mathbf{z}_m^p = \mathbf{z}_p^l(\mathbf{W}, \mathbf{x}_m)$  for all other channels  $p \neq q$ , by executing the forward pass, yielding activation values for all spatial neurons for the channels<sup>12</sup>.

We then define the averaged cosine similarity  $\rho_{qp}$  between two channels  $q$  and  $p$  in same layer  $l$  as

$$\rho_{qp} = \frac{1}{2} \left( \cos(\phi)_{qp} + \cos(\phi)_{pq} \right) \quad (30)$$

$$\text{with} \quad \cos(\phi)_{qp} = \frac{1}{k} \sum_{\mathbf{x}_m \in \mathcal{X}_{(k,q)}^{\text{rel}}} \frac{\mathbf{z}_m^q \cdot \mathbf{z}_m^p}{\|\mathbf{z}_m^q\| \cdot \|\mathbf{z}_m^p\|}. \quad (31)$$

Note that we symmetrize  $\rho_{qp}$  in Equation (30) as the cosine similarities  $\cos(\phi)_{qp}$  and  $\cos(\phi)_{pq}$  are in general not identical, due to the potential dissimilarities in the reference sample sets  $\mathcal{X}_{(k,q)}^*$  and  $\mathcal{X}_{(k,p)}^*$ . Thus,  $\cos(\phi)_{qp}$  measures the cosine similarity between filter  $q$  and filter  $p$  wrt. the reference samples representing filter  $q$ . The from Equation (30) resulting symmetric similarity measures  $\rho_{qp} = \rho_{pq} \in [0, 1]$  can now be clustered, and visualized via a transformation into a distance measure<sup>13</sup>  $d_{qp} = 1 - \rho_{qp}$  serving as an input to t-SNE [134] which clusters similar filters together in, in our case,  $\mathbb{R}^2$ .

Figure 24 shows an analysis result focusing on a cluster around filter  $q = 281$  from `features.40` of a VGG-16 network with BatchNorm layers trained on ImageNet, representing facial features and fur patterns of house cats, with the most similar neighbor in terms of activatory behavior being filter 289, representing zoomed-in representations and facial features of tabby cats. Investigating the other neighboring filter of the cluster by following the spatial embedding and thus roughly their  $\rho$ -similarity to filter 281, we can for one observe clear conceptual similarities of the filters as represented by their  $\mathcal{X}_{8_{\text{sum}}}^{\text{rel}}$  reference sample sets. Furthermore, we can observe a *change* in the nature of represented concepts: While filters 281 and 289 represent cat faces and fur pattern, as well as cat eyes in close-up view, the filters 160, 93 and 16 pick up on the concept of big eyes and respectively seem to represent large-eyed and flat nosed persian cats and pug dogs in frontal view (filter 160), flat-faced animals with large black eyes and brown to white fur patterns (filter 93), and faces of animals of brown to gray fur with small black eyes (filter 15). After a larger step in

<sup>11</sup>The cited literature concludes that the occurrence of poly-semantic units is rare for models trained on ImageNet.

<sup>12</sup>Here,  $k = 40$  is an arbitrary choice, resulting from the common minimal size of available pre-computed reference sample sets for all filters.

<sup>13</sup>Note that normally, the output value of the cosine distance covers the interval  $[-1, 1]$ , where for  $-1$  the two measured vectors are exactly opposite to one another, for  $1$  they are identical and for  $0$  they are orthogonal. In case output channels of dense layers are analyzed, i.e. scalar values, the range of output values reduces to the set  $\{-1, 0, 1\}$ , as both values are either of same or different signs, or at least one of the values is zero. Since we are processing layer activations *after* the ReLU nonlinearities of the layer, which yields only positive values for  $\mathbf{z}_m^q$  and  $\mathbf{z}_m^p$ . This results in  $\rho_{pq} \in [0, 1]$ , and a conversion to a canonical distance measure  $d_{qp} \in [0, 1]$ .

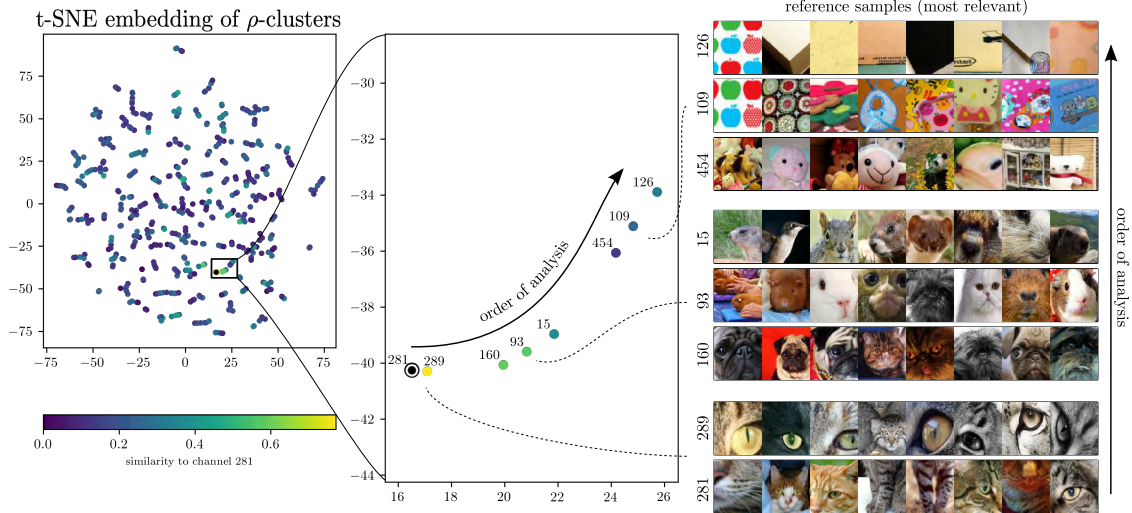


Figure 24: (Left and center): Filter channels from `features.40` of a VGG-16 with BatchNorm, clustered and embedded according to  $\rho$ -similarity. Markers are colored according to their  $\rho$ -similarity to filter 281. (Right): Reference examples are selected based on RelMax summation. Our analysis has identified a cluster of related filters which, when observed according to decreased similarity to filter 281, describes a transition of simplification from cat faces and eyes over other animals with flat faces and dark eyes to simple colored shapes with dots.

embedding space, filters 454, 109 and 126 seem to further simplify the progression of animal face representations to black or large dots on uniformly colored round shapes (filter 454), to colorful shapes of lower complexity with dots (filter 109) to ultimately almost uniformly colored objects (filter 126), seemingly completing a transition to simpler and more abstract concepts starting at filter 281.

We discuss another analysis in Figure 25 focussing on filter  $q = 446$  in `features.40` of the same model, showing various types of typewriter and rectangular laptop keyboard buttons and roofing shingles photographed in oblique perspective, as well as round buttons of typewriters, remote controls for televisions, telephone keys and round turnable dials of various devices and machinery. Other than the concepts discovered in context of Figure 24 and filter 281, the filters around filter 446 seem to cover different aspects of a shared “button” or “small tile” concept. The filters located in this cluster have been identified as similar due to their similar activations over the combined reference sample sets. Assuming redundancy based on the filter channels’ apparently similar activation behavior, the stakeholder could merge or cluster them to one encompassing concept, thereby simplifying interpretation by reducing the number of filters in the model. We therefore further investigate the filters 7, 94, 446 and 357 (all showing buttons or keys) in order to find out whether they encode a concept collaboratively, whether they are partly redundant, or whether the cluster serves some discriminative purpose.

We observe that the filters are most relevant for classes “laptop computer” and “remote control”. Consequently, we compute neuron activations and attribution scores for samples from both classes and observe the attributed relevance to those features when performing CRP wrt. the ground truth class output. See Figure 26 for visualizations. Regardless of whether an instance from class “laptop” or “remote control” is chosen as input, the activation map across the observed channels is similar for each instance. The per-channel CRP attribution map however reveals that while all filters react to similar stimuli in terms of activations, the model seems to use the subtle differences among the observed concepts to distinguish between both classes they are most relevant for: For both class “laptop” and “remote control”, buttons are striking and defining features, and all observed filters activate for button features. However, when computing relevance scores for class “laptop”, the activating filters representing round buttons (filters 7, 94, and 446) dominantly receive negatively signed attribution scores, while filter 357 clearly representing typical keyboard button layouts receives high positive relevance cores. For samples of class “remote control”, the

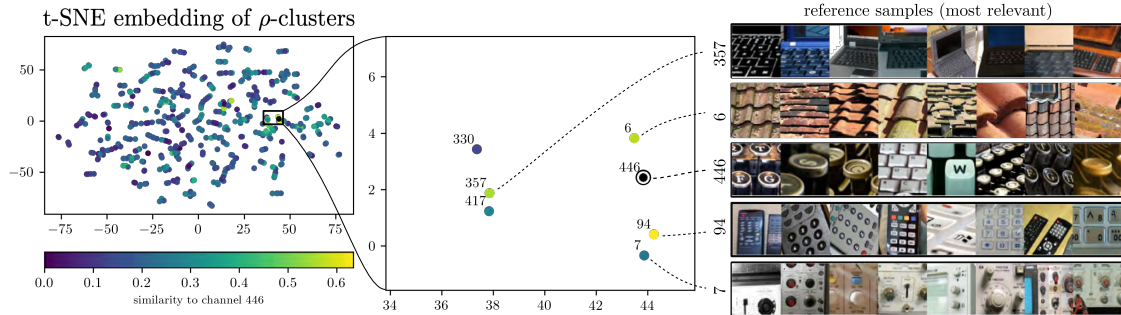


Figure 25: (*Left and center*): Filter channels from `features.40` of a VGG-16 with BatchNorm, clustered and embedded according to  $\rho$ -similarity. Markers are colored according to their  $\rho$ -similarity to filter 446. (*Right*): Reference examples are selected based on RelMax summation. (*Center and Right*): One particular cluster around channel 446 is shown in more detail with five similarly activating channels and their reference images obtained via RelMax. As per the reference images, the over-all concept of the cluster seems to be related to rectangular roofing shingles and keyboard keys, as well as round buttons.

computation of relevance scores wrt. their true class<sup>14</sup> yields almost exactly opposite attributions, indicating that filters encoding round buttons and dials (filters 94 and 7) provide evidence for class “remote control”, while the activation of channel 357 clearly speaks against the analyzed class visible in relevance attribution. In both relevance analyses, however, filter 446 receives weak negative attributions, presumably as it represents a particular expression of both round and angular buttons which fits (or contradicts) neither of the compared classes particularly well. In fact, filter 446 is highly relevant for class “typewriter keyboard” instead.

In conclusion, we report that although several filters may show signs of correlation in terms of output activation, they are not necessarily encoding redundant information or are serving the same purpose. Conversely, using our proposed Concept Relevance Propagation in combination with the Relevance Maximization-based process for selecting reference examples representing seemingly correlating filters, we are able to discover and understand the subtleties a neural network has learned to encode in its latent representations. See Appendix A.9 for additional results in extension to this section.

## 5 Conclusion

In this work we have introduced Concept Relevance Propagation, a post-hoc explanation method, which not only indicates which part of the input is relevant for an individual prediction, but also communicates the meaning of involved latent representations by providing human-understandable examples. Since CRP combines the benefits of the local and global XAI perspective, it computes more detailed and contextualized explanations, considerably extending the state-of-the-art. Among its advantages are the high computational efficiency (order of a backward pass) and the out-of-the-box applicability to (almost) any model without imposing constraints on the training process, the data and label availability, or the model architecture. Furthermore, CRP introduces the idea of conditional backpropagation tied to a single concept or a combination of concepts as encoded by the model, within or across layers. Via this ansatz, the contribution of all neurons’ concepts in a layer can be faithfully attributed, localized in the input space, and finally their interaction can be studied. As shown in this work, such an analysis allows one to disentangle and separately explain the multitude of in-parallel partial forward processes, which transform and combine features and concepts before culminating into a prediction. Finally, with Relevance Maximization we move beyond the decade-old practice of communicating latent features of neural networks based on examples obtained via maximized activation. In particular, we show that the examples which stimulate hidden features maximally are not necessarily useful for the model in an inference context,

<sup>14</sup>or even the computation of CRP for samples from class “laptop” wrt. the class output for “remote control”

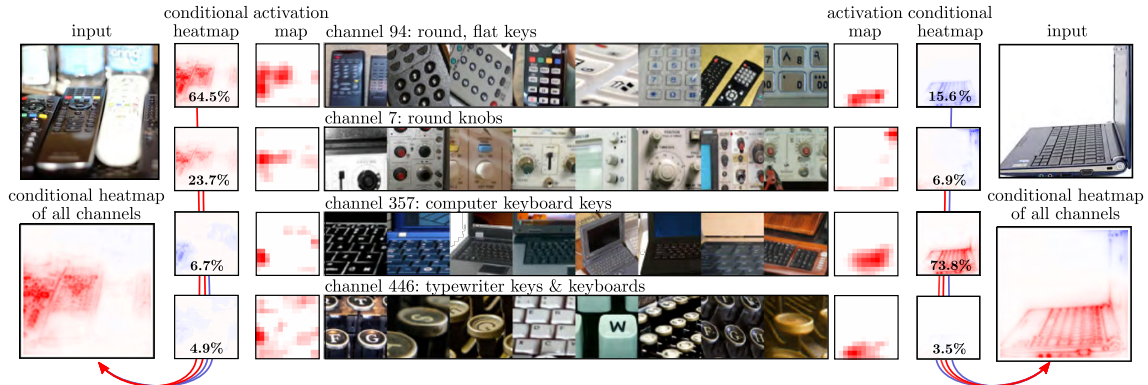


Figure 26: Relevance-based investigation of similarly activating channels identified in context of Figure 25. (*Center*): Reference examples for the analyzed channels 7, 04, 357 and 446 from `features.40` from a VGG-16 with BatchNorm layers. (*Left*): Exemplary input from class “remote control” with per-channel activation maps and respective ground truth conditional relevance maps, as well as their aggregation  $\theta = \{y, c_{94}, c_7, c_{357}, c_{446}\}$  (bottom left). (*Right*): Exemplary input from class “laptop computer” with per-channel activation maps and respective ground truth conditional relevance maps, as well as their aggregation. Conditional relevance attributions  $R(x|\theta)$  are normalized wrt. the common maximum amplitude. Similarly *activating* channels do not necessarily encode redundant information, but might be used by the model for making fine-grained distinctions, which can be observed from the attributed relevance scores.

or representative for the data the model is familiar and confident with. By providing examples based on relevance, however, the user is presented with data with characteristics which actually play an important role in the prediction process. Since the user can select examples wrt. any (i.e., not necessarily the ground truth) output class, our approach constitutes a new tool to systematically investigate latent concepts in neural networks.

Our experiments have qualitatively and quantitatively demonstrated the additional value of the CRP approach for common datasets and end-to-end trained models. Specifically, we showed that reference samples selected with relevance-based criteria, concept heatmaps and atlases, as well as concept composition graphs open up the ability to understand model reasoning on a more abstract and conceptual level. These insights then allowed us to identify Clever Hans concepts, to investigate their impact, and finally to correct for these misbehaviors. Further, using our relevance-based reference sample sets, we were able to identify concept themes spanned by sets of filters in latent space. Although channels of a cluster have a similar function, they seem to be used by the model for fine-grained decisions regarding details in the data, such as the particular type of buttons to partially decide whether an image shows a laptop keyboard, a mechanical typewriter or a TV remote control. Finally, we have demonstrated the usefulness of CRP in non-image data domain, where traditional attribution maps are often difficult to interpret and comprehend by the user. Our experiments on time series data have shown that as long as a visualization of the data can be found, the meaning of latent concepts can be communicated via reference examples.

As CRP is based on the modified backpropagation approach of LRP, an adaptation to other neural-network-like predictors and architectures, such as recurrent [9] or graph [113] neural networks is possible, but might require additional fine-tuning in terms of configuring decomposition rules and parameters [82, 64] to the model, or applying neural network canonization [55, 47, 88].

Overall, we believe that the tools we have proposed in this work, and the resulting increase in semantics and detail to be found in sample-specific neural network explanations, will advance the applicability of post-hoc eXplainable Artificial Intelligence to novel or previously difficult to handle models, problems and data domains.



## References

- [1] Amina Adadi and Mohammed Berrada. Peeking inside the black-box: A survey on explainable artificial intelligence. *IEEE Access*, 6:52138–52160, 2018.
- [2] Baris Akdemir, Hiran Yarmohammadi, M Chadi Alraies, and Wayne O Adkisson. Premature ventricular contractions: Reassure or refer? *Cleveland Clinic journal of medicine*, 83(7):524–530, 2016.
- [3] Maximilian Alber, Sebastian Lapuschkin, Philipp Seegerer, Miriam Hägele, Kristof T. Schütt, Grégoire Montavon, Wojciech Samek, Klaus-Robert Müller, Sven Dähne, and Pieter-Jan Kindermans. iNNvestigate neural networks! *Journal of Machine Learning Research*, 20:93:1–93:8, 2019.
- [4] Farman Ali, Shaker El-Sappagh, SM Riazul Islam, Daehan Kwak, Amjad Ali, Muhammad Imran, and Kyung-Sup Kwak. A smart healthcare monitoring system for heart disease prediction based on ensemble deep learning and feature fusion. *Information Fusion*, 63:208–222, 2020.
- [5] Christopher J. Anders, David Neumann, Wojciech Samek, Klaus-Robert Müller, and Sebastian Lapuschkin. Software for dataset-wide XAI: from local explanations to global insights with Zennit, CoRelAy, and ViRelAy. *arXiv preprint arXiv:2106.13200*, 2021.
- [6] Christopher J. Anders, Leander Weber, David Neumann, Wojciech Samek, Klaus-Robert Müller, and Sebastian Lapuschkin. Finding and removing clever hans: Using explanation methods to debug and improve deep models. *Information Fusion*, 77:261–295, 2022.
- [7] André Araujo, Wade Norris, and Jack Sim. Computing receptive fields of convolutional neural networks. *Distill*, 4(11):e21, 2019.
- [8] Parul Arora, Himanshu Kumar, and Bijaya Ketan Panigrahi. Prediction and analysis of COVID-19 positive cases using deep learning models: A descriptive case study of India. *Chaos, Solitons & Fractals*, 139:110017, 2020.
- [9] Leila Arras, Grégoire Montavon, Klaus-Robert Müller, and Wojciech Samek. Explaining recurrent neural network predictions in sentiment analysis. In *8th EMNLP Workshop on Computational Approaches to Subjectivity, Sentiment and Social Media Analysis (WASSA)*, pages 159–168, 2017.
- [10] Leila Arras, Ahmed Osman, Klaus-Robert Müller, and Wojciech Samek. Evaluating recurrent neural network explanations. In *ACL 2019 Workshop on BlackboxNLP: Analyzing and Interpreting Neural Networks for NLP*, pages 113–126, 2019.
- [11] Sebastian Bach, Alexander Binder, Grégoire Montavon, Frederick Klauschen, Klaus-Robert Müller, and Wojciech Samek. On pixel-wise explanations for non-linear classifier decisions by Layer-Wise Relevance Propagation. *PloS one*, 10(7):e0130140, 2015.
- [12] David Baehrens, Timon Schroeter, Stefan Harmeling, Motoaki Kawanabe, Katja Hansen, and Klaus-Robert Müller. How to explain individual classification decisions. *The Journal of Machine Learning Research*, 11:1803–1831, 2010.
- [13] Dzmitry Bahdanau, Kyunghyun Cho, and Yoshua Bengio. Neural machine translation by jointly learning to align and translate. In *3rd International Conference on Learning Representations (ICLR)*, 2015.
- [14] David Balduzzi, Marcus Frean, Lennox Leary, J. P. Lewis, Kurt Wan-Duo Ma, and Brian McWilliams. The shattered gradients problem: If resnets are the answer, then what is the question? In *34th International Conference on Machine Learning (ICML)*, volume 70, pages 342–350, 2017.

- [15] David Bau, Bolei Zhou, Aditya Khosla, Aude Oliva, and Antonio Torralba. Network dissection: Quantifying interpretability of deep visual representations. In *IEEE International Conference on Computer Vision and Pattern Recognition (CVPR)*, pages 3319–3327, 2017.
- [16] David Bau, Jun-Yan Zhu, Hendrik Strobelt, Àgata Lapedriza, Bolei Zhou, and Antonio Torralba. Understanding the role of individual units in a deep neural network. *Proc. Natl. Acad. Sci. USA*, 117(48):30071–30078, 2020.
- [17] Sören Becker, Marcel Ackermann, Sebastian Lapuschkin, Klaus-Robert Müller, and Wojciech Samek. Interpreting and explaining deep neural networks for classification of audio signals. *arXiv preprint arXiv:1807.03418*, 2018.
- [18] Daniel Becking, Maximilian Dreyer, Wojciech Samek, Karsten Müller, and Sebastian Lapuschkin. ECQ<sup>x</sup>: Explainability-driven quantization for low-bit and sparse DNNs. *arXiv preprint arXiv:2109.04236*, 2021.
- [19] Alexander Binder. Notes on canonization for resnets and densenets. [https://github.com/AlexBinder/LRP\\_Pytorch\\_Resnets\\_Densenet/blob/master/canonization\\_doc.pdf](https://github.com/AlexBinder/LRP_Pytorch_Resnets_Densenet/blob/master/canonization_doc.pdf), 2020.
- [20] Judy Borowski, Roland Simon Zimmermann, Judith Schepers, Robert Geirhos, Thomas SA Wallis, Matthias Bethge, and Wieland Brendel. Exemplary natural images explain CNN activations better than state-of-the-art feature visualization. In *9th International Conference on Learning Representations (ICLR)*, 2020.
- [21] Sebastian Bosse, Sören Becker, Klaus-Robert Müller, Wojciech Samek, and Thomas Wiegand. Estimation of distortion sensitivity for visual quality prediction using a convolutional neural network. *Digital Signal Processing*, 91:54–65, 2019.
- [22] Sebastian Bosse, Dominique Maniry, Klaus-Robert Müller, Thomas Wiegand, and Wojciech Samek. Deep neural networks for no-reference and full-reference image quality assessment. *IEEE Transactions on Image Processing*, 27(1):206–219, 2018.
- [23] Sebastian Bruckert, Bettina Finzel, and Ute Schmid. The next generation of medical decision support: A roadmap toward transparent expert companions. *Frontiers in Artificial Intelligence*, 3:75, 2020.
- [24] Nick Cammarata, Shan Carter, Gabriel Goh, Chris Olah, Michael Petrov, Ludwig Schubert, Chelsea Voss, Ben Egan, and Swee Kiat Lim. Thread: Circuits. *Distill*, 5(3):e24, 2020.
- [25] Shan Carter, Zan Armstrong, Ludwig Schubert, Ian Johnson, and Chris Olah. Activation atlas. *Distill*, 4(3):e15, 2019.
- [26] Gromit Yeuk-Yin Chan, Enrico Bertini, Luis Gustavo Nonato, Brian Barr, and Claudio T Silva. Melody: Generating and visualizing machine learning model summary to understand data and classifiers together. *arXiv preprint arXiv:2007.10614*, 2020.
- [27] Chaofan Chen, Oscar Li, Daniel Tao, Alina Barnett, Cynthia Rudin, and Jonathan K Su. This looks like that: Deep learning for interpretable image recognition. *Advances in Neural Information Processing Systems (NeurIPS)*, 32:8930–8941, 2019.
- [28] Zhi Chen, Yijie Bei, and Cynthia Rudin. Concept whitening for interpretable image recognition. *Nature Machine Intelligence*, 2(12):772–782, 2020.
- [29] Noel CF Codella, David Gutman, M Emre Celebi, Brian Helba, Michael A Marchetti, Stephen W Duszka, Aadi Kalloo, Konstantinos Liopyris, Nabin Mishra, Harald Kittler, et al. Skin lesion analysis toward melanoma detection: A challenge at the 2017 international symposium on biomedical imaging (ISBI), hosted by the international skin imaging collaboration (ISIC). In *IEEE International Symposium on Biomedical Imaging (ISBI)*, pages 168–172, 2018.

- [30] Marc Combalia, Noel CF Codella, Veronica Rotemberg, Brian Helba, Veronica Vilaplana, Ofer Reiter, Cristina Carrera, Alicia Barreiro, Allan C Halpern, Susana Puig, et al. BCN20000: Dermoscopic lesions in the wild. *arXiv preprint arXiv:1908.02288*, 2019.
- [31] Commission to the European Parliament, the Council, the European Economic and Social Committee, and the Committee of the Regions. Communication: Building trust in human centric artificial intelligence. *COM*, 168, 2019.
- [32] Zihang Dai, Hanxiao Liu, Quoc Le, and Mingxing Tan. Coatnet: Marrying convolution and attention for all data sizes. *Advances in Neural Information Processing Systems (NeurIPS)*, 34, 2021.
- [33] Arun Das and Paul Rad. Opportunities and challenges in explainable artificial intelligence: A survey. *arXiv preprint arXiv:2006.11371*, 2020.
- [34] Alex Davies, Petar Veličković, Lars Buesing, Sam Blackwell, Daniel Zheng, Nenad Tomašev, Richard Tanburn, Peter Battaglia, Charles Blundell, András Juhász, et al. Advancing mathematics by guiding human intuition with AI. *Nature*, 600(7887):70–74, 2021.
- [35] Eran Eiding, Roe Enbar, and Tal Hassner. Age and gender estimation of unfiltered faces. *IEEE Transactions on Information Forensics and Security (TIFS)*, 9(12):2170–2179, 2014.
- [36] Dumitru Erhan, Yoshua Bengio, Aaron Courville, and Pascal Vincent. Visualizing higher-layer features of a deep network. *University of Montreal*, 1341(3):1, 2009.
- [37] E Harvey Estes, Zhu-Ming Zhang, Yabing Li, Larisa G Tereschenko, and Elsayed Z Soliman. The Romhilt-Estes left ventricular hypertrophy score and its components predict all-cause mortality in the general population. *American heart journal*, 170(1):104–109, 2015.
- [38] Bettina Finzel, David E Tafler, Stephan Scheele, and Ute Schmid. Explanation as a process: user-centric construction of multi-level and multi-modal explanations. In *German Conference on Artificial Intelligence (Künstliche Intelligenz)*, pages 80–94. Springer, 2021.
- [39] Ruth Fong and Andrea Vedaldi. Net2Vec: Quantifying and explaining how concepts are encoded by filters in deep neural networks. In *IEEE Conference on Computer Vision and Pattern Recognition (CVPR)*, pages 8730–8738, 2018.
- [40] Ruth C Fong and Andrea Vedaldi. Interpretable explanations of black boxes by meaningful perturbation. In *IEEE International Conference on Computer Vision (ICCV)*, pages 3429–3437, 2017.
- [41] Association for the Advancement of Medical Instrumentation and American National Standards Institute. *Testing and Reporting Performance Results of Cardiac Rhythm and ST-segment Measurement Algorithms*. ANSI/AAMI. The Association, 1998.
- [42] Michael Gerstenberger, Sebastian Lapuschkin, Peter Eisert, and Sebastian Bosse. But that’s not why: Inference adjustment by interactive prototype deselection. *arXiv preprint arXiv:2203.10087*, 2022.
- [43] Amirata Ghorbani, James Wexler, James Y Zou, and Been Kim. Towards automatic concept-based explanations. *Advances in Neural Information Processing Systems (NeurIPS)*, 32, 2019.
- [44] Gabriel Goh, Nick Cammarata, Chelsea Voss, Shan Carter, Michael Petrov, Ludwig Schubert, Alec Radford, and Chris Olah. Multimodal neurons in artificial neural networks. *Distill*, 6(3):e30, 2021.
- [45] Bryce Goodman and Seth Flaxman. European union regulations on algorithmic decision-making and a “right to explanation”. *AI magazine*, 38(3):50–57, 2017.

- [46] Riccardo Guidotti, Anna Monreale, Salvatore Ruggieri, Dino Pedreschi, Franco Turini, and Fosca Giannotti. Local rule-based explanations of black box decision systems. *arXiv preprint arXiv:1805.10820*, 2018.
- [47] Mathilde Guillemot, Catherine Heusele, Rodolphe Korichi, Sylvianne Schnebert, and Liming Chen. Breaking batch normalization for better explainability of deep neural networks through Layer-Wise Relevance Propagation. *arXiv preprint arXiv:2002.11018*, 2020.
- [48] Steven A Haist. *Clinician’s Pocket Reference*, page 375. McGraw-Hill, 9 edition, 2002.
- [49] Seung Seog Han, Ilwoo Park, Sung Eun Chang, Woohyung Lim, Myoung Shin Kim, Gyeong Hun Park, Je Byeong Chae, Chang Hun Huh, and Jung-Im Na. Augmented intelligence dermatology: Deep neural networks empower medical professionals in diagnosing skin cancer and predicting treatment options for 134 skin disorders. *Journal of Investigative Dermatology*, 140(9):1753–1761, 2020.
- [50] Kaiming He, Xiangyu Zhang, Shaoqing Ren, and Jian Sun. Deep residual learning for image recognition. In *IEEE Conference on Computer Vision and Pattern Recognition (CVPR)*, pages 770–778, 2016.
- [51] Pradeep Hewage, Marcello Trovati, Ella Pereira, and Ardhendu Behera. Deep learning-based effective fine-grained weather forecasting model. *Pattern Analysis and Applications*, 24(1):343–366, 2021.
- [52] Geoffrey Hinton, Nitish Srivastava, and Kevin Swersky. Neural networks for machine learning lecture 6a overview of mini-batch gradient descent. *Cited on*, 14(8):2, 2012.
- [53] Fred Hohman, Haekyu Park, Caleb Robinson, and Duen Horng Polo Chau. Summit: Scaling deep learning interpretability by visualizing activation and attribution summarizations. *IEEE Transactions on Visualization and Computer Graphics (TVCG)*, 26(1):1096–1106, 2019.
- [54] Xinyu Huang, Xinjing Cheng, Qichuan Geng, Binbin Cao, Dingfu Zhou, Peng Wang, Yuanqing Lin, and Ruigang Yang. The apolloscape dataset for autonomous driving. In *IEEE Conference on Computer Vision and Pattern Recognition (CVPR)*, 2018.
- [55] Lucas Y. W. Hui and Alexander Binder. BatchNorm Decomposition for deep neural network interpretation. In *Advances in Computational Intelligence*, Lecture Notes in Computer Science, pages 280–291. Springer, 2019.
- [56] Andrew Ilyas, Shibani Santurkar, Dimitris Tsipras, Logan Engstrom, Brandon Tran, and Aleksander Madry. Adversarial examples are not bugs, they are features. *Advances in Neural Information Processing Systems (NeurIPS)*, 32, 2019.
- [57] Max Jaderberg, Wojciech M Czarnecki, Iain Dunning, Luke Marris, Guy Lever, Antonio Garcia Castaneda, Charles Beattie, Neil C Rabinowitz, Ari S Morcos, Avraham Ruderman, et al. Human-level performance in 3D multiplayer games with population-based reinforcement learning. *Science*, 364(6443):859–865, 2019.
- [58] Mohammad Kachuee, Shayan Fazeli, and Majid Sarrafzadeh. ECG heartbeat classification: A deep transferable representation. In *IEEE International Conference on Healthcare Informatics (ICHI)*, pages 443–444, 2018.
- [59] Mohammad Ali Kadampur and Sulaiman Al Riyae. Skin cancer detection: Applying a deep learning based model driven architecture in the cloud for classifying dermal cell images. *Informatics in Medicine Unlocked*, 18:100282, 2020.
- [60] Been Kim, Martin Wattenberg, Justin Gilmer, Carrie Cai, James Wexler, Fernanda Viegas, et al. Interpretability beyond feature attribution: Quantitative testing with concept activation vectors (TCAV). In *35th International Conference on Machine Learning (ICML)*, pages 2668–2677, 2018.

- [61] Pieter-Jan Kindermans, Kristof T. Schütt, Maximilian Alber, Klaus-Robert Müller, D. Erhan, Been Kim, and Sven Dähne. Learning how to explain neural networks: PatternNet and PatternAttribution. In *6th International Conference on Learning Representations (ICLR)*, 2018.
- [62] Diederik P. Kingma and Jimmy Ba. Adam: A method for stochastic optimization. In *3rd International Conference on Learning Representations (ICLR)*, 2015.
- [63] Pang Wei Koh, Thao Nguyen, Yew Siang Tang, Stephen Mussmann, Emma Pierson, Been Kim, and Percy Liang. Concept bottleneck models. In *37th International Conference on Machine Learning (ICML)*, pages 5338–5348. PMLR, 2020.
- [64] Maximilian Kohlbrenner, Alexander Bauer, Shinichi Nakajima, Alexander Binder, Wojciech Samek, and Sebastian Lapuschkin. Towards best practice in explaining neural network decisions with LRP. In *2020 International Joint Conference on Neural Networks (IJCNN)*, pages 1–7. IEEE, 2020.
- [65] Alex Krizhevsky, Ilya Sutskever, and Geoffrey E Hinton. ImageNet classification with deep convolutional neural networks. *Communications of the ACM*, 60(6):84–90, 2017.
- [66] Will Landecker, Michael D Thomure, Luís MA Bettencourt, Melanie Mitchell, Garrett T Kenyon, and Steven P Brumby. Interpreting individual classifications of hierarchical networks. In *2013 IEEE symposium on computational intelligence and data mining (CIDM)*, pages 32–38. IEEE, 2013.
- [67] Oran Lang, Yossi Gandelsman, Michal Yarom, Yoav Wald, Gal Elidan, Avinatan Hassidim, William T Freeman, Phillip Isola, Amir Globerson, Michal Irani, et al. Explaining in style: Training a GAN to explain a classifier in StyleSpace. In *IEEE/CVF International Conference on Computer Vision (ICCV)*, pages 693–702, 2021.
- [68] Sebastian Lapuschkin, Alexander Binder, Klaus-Robert Müller, and Wojciech Samek. Understanding and comparing deep neural networks for age and gender classification. In *IEEE International Conference on Computer Vision (ICCV) Workshops*, pages 1629–1638, 2017.
- [69] Sebastian Lapuschkin, Stephan Wäldchen, Alexander Binder, Grégoire Montavon, Wojciech Samek, and Klaus-Robert Müller. Unmasking clever hans predictors and assessing what machines really learn. *Nature Communications*, 10(1):1–8, 2019.
- [70] Hugo Larochelle and Geoffrey E Hinton. Learning to combine foveal glimpses with a third-order boltzmann machine. *Advances in Neural Information Processing Systems (NeurIPS)*, 23:1243–1251, 2010.
- [71] Yann LeCun, Yoshua Bengio, and Geoffrey Hinton. Deep learning. *Nature*, 521(7553):436–444, 2015.
- [72] Yann LeCun, Léon Bottou, Yoshua Bengio, and Patrick Haffner. Gradient-based learning applied to document recognition. *Proceedings IEEE*, 86(11):2278–2324, 1998.
- [73] Jesse Levinson, Jake Askeland, Jan Becker, Jennifer Dolson, David Held, Soeren Kammel, J Zico Kolter, Dirk Langer, Oliver Pink, Vaughan Pratt, et al. Towards fully autonomous driving: Systems and algorithms. In *IEEE Intelligent Vehicles Symposium (IV)*, pages 163–168, 2011.
- [74] Min Lin, Qiang Chen, and Shuicheng Yan. Network in network. *arXiv preprint arXiv:1312.4400*, 2013.
- [75] Mengchen Liu, Jiaxin Shi, Zhen Li, Chongxuan Li, Jun Zhu, and Shixia Liu. Towards better analysis of deep convolutional neural networks. *IEEE Transactions on Visualization and Computer Graphics (TVCG)*, 23(1):91–100, 2016.
- [76] Scott M Lundberg and Su-In Lee. A unified approach to interpreting model predictions. *Advances in Neural Information Processing Systems (NeurIPS)*, 30, 2017.

- [77] Peter W Macfarlane, Adriaan Van Oosterom, Olle Pahlm, Paul Kligfield, Michiel Janse, and John Camm. *Comprehensive electrocardiology*. Springer Science & Business Media, 2010.
- [78] Aravindh Mahendran and Andrea Vedaldi. Understanding deep image representations by inverting them. In *IEEE Conference on Computer Vision and Pattern Recognition (CVPR)*, pages 5188–5196, 2015.
- [79] Leland McInnes, John Healy, and James Melville. Umap: Uniform manifold approximation and projection for dimension reduction. *arXiv preprint arXiv:1802.03426*, 2018.
- [80] Marina Meilă and Jianbo Shi. A random walks view of spectral segmentation. In *International Workshop on Artificial Intelligence and Statistics*, pages 203–208. PMLR, 2001.
- [81] P Molchanov, S Tyree, T Karras, T Aila, and J Kautz. Pruning convolutional neural networks for resource efficient inference. In *5th International Conference on Learning Representations (ICLR)*, 2017.
- [82] Grégoire Montavon, Alexander Binder, Sebastian Lapuschkin, Wojciech Samek, and Klaus-Robert Müller. Layer-Wise Relevance Propagation: An overview. In *Explainable AI: Interpreting, Explaining and Visualizing Deep Learning*, volume 11700 of *Lecture Notes in Computer Science*, pages 193–209. Springer, 2019.
- [83] Grégoire Montavon, Sebastian Lapuschkin, Alexander Binder, Wojciech Samek, and Klaus-Robert Müller. Explaining nonlinear classification decisions with deep taylor decomposition. *Pattern recognition*, 65:211–222, 2017.
- [84] Grégoire Montavon, Wojciech Samek, and Klaus-Robert Müller. Methods for interpreting and understanding deep neural networks. *Digital Signal Processing*, 73:1–15, 2018.
- [85] George B Moody and Roger G Mark. The impact of the MIT-BIH arrhythmia database. *IEEE Engineering in Medicine and Biology Magazine*, 20(3):45–50, 2001.
- [86] Niels JS Morch, Ulrik Kjems, Lars Kai Hansen, Claus Svarer, Ian Law, Benny Lautrup, Steve Strother, and Kelly Rehm. Visualization of neural networks using saliency maps. In *ICNN’95-International Conference on Neural Networks*, volume 4, pages 2085–2090. IEEE, 1995.
- [87] Alexander Mordvintsev, Christopher Olah, and Mike Tyka. Inceptionism: Going deeper into neural networks. *Google AI blog*, 2015.
- [88] Franz Motzkus, Leander Weber, and Sebastian Lapuschkin. Measurably stronger explanation reliability via model canonization. *arXiv preprint arXiv:2202.06621*, 2022.
- [89] W. James Murdoch, Peter J. Liu, and Bin Yu. Beyond word importance: Contextual decomposition to extract interactions from lstms. In *6th International Conference on Learning Representations (ICLR)*, 2018.
- [90] Anh Nguyen, Alexey Dosovitskiy, Jason Yosinski, Thomas Brox, and Jeff Clune. Synthesizing the preferred inputs for neurons in neural networks via deep generator networks. *Advances in Neural Information Processing Systems (NeurIPS)*, 29:3387–3395, 2016.
- [91] Anh Nguyen, Jason Yosinski, and Jeff Clune. Multifaceted feature visualization: Uncovering the different types of features learned by each neuron in deep neural networks. *arXiv preprint arXiv:1602.03616*, 2016.
- [92] Anh Nguyen, Jason Yosinski, and Jeff Clune. Understanding neural networks via feature visualization: A survey. In *Explainable AI: interpreting, explaining and visualizing deep learning*, pages 55–76. Springer, 2019.
- [93] Anna Nguyen, Daniel Hagenmayer, Tobias Weller, and Michael Färber. Explaining convolutional neural networks by tagging filters. *arXiv preprint arXiv:2109.09389*, 2021.

- [94] Chris Olah, Alexander Mordvintsev, and Ludwig Schubert. Feature visualization. *Distill*, 2(11):e7, 2017.
- [95] Chris Olah, Arvind Satyanarayan, Ian Johnson, Shan Carter, Ludwig Schubert, Katherine Ye, and Alexander Mordvintsev. The building blocks of interpretability. *Distill*, 3(3):e10, 2018.
- [96] Adam Paszke, Sam Gross, Francisco Massa, Adam Lerer, James Bradbury, Gregory Chanan, Trevor Killeen, Zeming Lin, Natalia Gimelshein, Luca Antiga, Alban Desmaison, Andreas Kopf, Edward Yang, Zachary DeVito, Martin Raison, Alykhan Tejani, Sasank Chilamkurthy, Benoit Steiner, Lu Fang, Junjie Bai, and Soumith Chintala. Pytorch: An imperative style, high-performance deep learning library. In *Advances in Neural Information Processing Systems 32*, pages 8024–8035. 2019.
- [97] Adam Paszke, Sam Gross, Francisco Massa, Adam Lerer, James Bradbury, Gregory Chanan, Trevor Killeen, Zeming Lin, Natalia Gimelshein, Luca Antiga, et al. PyTorch: An imperative style, high-performance deep learning library. *Advances in Neural Information Processing Systems (NeurIPS)*, 32, 2019.
- [98] Brett Poulin, Roman Eisner, Duane Szafron, Paul Lu, Russell Greiner, David S Wishart, Alona Fyshe, Brandon Pearcy, Cam MacDonell, and John Anvik. Visual explanation of evidence with additive classifiers. In *The National Conference On Artificial Intelligence*, volume 21, page 1822, 2006.
- [99] Kristina Preuer, Günter Klambauer, Friedrich Rippmann, Sepp Hochreiter, and Thomas Unterthiner. Interpretable deep learning in drug discovery. In *Explainable AI: Interpreting, Explaining and Visualizing Deep Learning*, pages 331–345. Springer, 2019.
- [100] Johannes Rabold, Hannah Deininger, Michael Siebers, and Ute Schmid. Enriching visual with verbal explanations for relational concepts—combining lime with aleph. In *Joint European Conference on Machine Learning and Knowledge Discovery in Databases*, pages 180–192. Springer, 2019.
- [101] Johannes Rabold, Gesina Schwalbe, and Ute Schmid. Expressive explanations of dnns by combining concept analysis with ilp. In *German Conference on Artificial Intelligence (Künstliche Intelligenz)*, pages 148–162. Springer, 2020.
- [102] Alec Radford, Rafal Jozefowicz, and Ilya Sutskever. Learning to generate reviews and discovering sentiment. *arXiv preprint arXiv:1704.01444*, 2017.
- [103] Rishi Rajalingham, Elias B Issa, Pouya Bashivan, Kohitij Kar, Kailyn Schmidt, and James J DiCarlo. Large-scale, high-resolution comparison of the core visual object recognition behavior of humans, monkeys, and state-of-the-art deep artificial neural networks. *Journal of Neuroscience*, 38(33):7255–7269, 2018.
- [104] Archit Rathore, Nithin Chalapathi, Sourabh Palande, and Bei Wang. Topoact: Visually exploring the shape of activations in deep learning. In *Computer Graphics Forum*, volume 40, pages 382–397. Wiley Online Library, 2021.
- [105] Marco Tulio Ribeiro, Sameer Singh, and Carlos Guestrin. "Why should I trust you?" Explaining the predictions of any classifier. In *22nd ACM SIGKDD International Conference on Knowledge Discovery and Data Mining*, pages 1135–1144, 2016.
- [106] Marco Tulio Ribeiro, Sameer Singh, and Carlos Guestrin. Anchors: High-precision model-agnostic explanations. In *AAAI Conference on Artificial Intelligence*, volume 32, 2018.
- [107] Andreas Rieckmann, Piotr Dworzynski, Leila Arras, Sebastian Lapuschkin, Wojciech Samek, Onyebuchi A Arah, Naja H Rod, and Claus T Ekstrom. Causes of outcome learning: A causal inference-inspired machine learning approach to disentangling common combinations of potential causes of a health outcome. *International Journal of Epidemiology*, 05 2022. dyac078.

- [108] Laura Rieger, Chandan Singh, W. James Murdoch, and Bin Yu. Interpretations are useful: Penalizing explanations to align neural networks with prior knowledge. In *37th International Conference on Machine Learning (ICML)*, volume 119, pages 8116–8126, 2020.
- [109] Cynthia Rudin. Stop explaining black box machine learning models for high stakes decisions and use interpretable models instead. *Nature Machine Intelligence*, 1(5):206–215, 2019.
- [110] Olga Russakovsky, Jia Deng, Hao Su, Jonathan Krause, Sanjeev Satheesh, Sean Ma, Zhiheng Huang, Andrej Karpathy, Aditya Khosla, Michael Bernstein, et al. ImageNet large scale visual recognition challenge. *International Journal of Computer Vision*, 115(3):211–252, 2015.
- [111] Wojciech Samek, Alexander Binder, Grégoire Montavon, Sebastian Lapuschkin, and Klaus-Robert Müller. Evaluating the visualization of what a deep neural network has learned. *IEEE Transactions on Neural Networks and Learning Systems (TNNLS)*, 28(11):2660–2673, 2017.
- [112] Wojciech Samek, Grégoire Montavon, Sebastian Lapuschkin, Christopher J. Anders, and Klaus-Robert Müller. Explaining deep neural networks and beyond: A review of methods and applications. *Proceedings IEEE*, 109(3):247–278, 2021.
- [113] Thomas Schnake, Oliver Eberle, Jonas Lederer, Shinichi Nakajima, Kristof T. Schütt, Klaus-Robert Müller, and Grégoire Montavon. XAI for graphs: Explaining graph neural network predictions by identifying relevant walks. *arXiv preprint arXiv:2006.03589*, 2020.
- [114] Patrick Schramowski, Wolfgang Stammer, Stefano Teso, Anna Brugger, Franziska Herbert, Xiaoting Shao, Hans-Georg Luigs, Anne-Katrin Mahlein, and Kristian Kersting. Making deep neural networks right for the right scientific reasons by interacting with their explanations. *Nature Machine Intelligence*, 2(8):476–486, 2020.
- [115] Jessica Schrouff, Sebastien Baur, Shaobo Hou, Diana Mincu, Eric Loreaux, Ralph Blanes, James Wexler, Alan Karthikesalingam, and Been Kim. Best of both worlds: local and global explanations with human-understandable concepts. *arXiv preprint arXiv:2106.08641*, 2021.
- [116] Kristof T Schütt, Farhad Arbabzadah, Stefan Chmiela, Klaus R Müller, and Alexandre Tkatchenko. Quantum-chemical insights from deep tensor neural networks. *Nature Communications*, 8(1):1–8, 2017.
- [117] Philipp Seegerer, Alexander Binder, René Saitenmacher, Michael Bockmayr, Maximilian Alber, Philipp Jurmeister, Frederick Klauschen, and Klaus-Robert Müller. Interpretable deep neural network to predict estrogen receptor status from haematoxylin-eosin images. In *Artificial Intelligence and Machine Learning for Digital Pathology*, pages 16–37. Springer, 2020.
- [118] Ramprasaath R Selvaraju, Michael Cogswell, Abhishek Das, Ramakrishna Vedantam, Devi Parikh, and Dhruv Batra. Grad-cam: Visual explanations from deep networks via gradient-based localization. In *IEEE International Conference on Computer Vision (ICCV)*, pages 618–626, 2017.
- [119] Andrew W Senior, Richard Evans, John Jumper, James Kirkpatrick, Laurent Sifre, Tim Green, Chongli Qin, Augustin Židek, Alexander WR Nelson, Alex Bridgland, et al. Improved protein structure prediction using potentials from deep learning. *Nature*, 577(7792):706–710, 2020.
- [120] Farah Shahid, Aneela Zameer, and Muhammad Muneeb. Predictions for COVID-19 with deep learning models of LSTM, GRU and Bi-LSTM. *Chaos, Solitons & Fractals*, 140:110212, 2020.
- [121] Snehlata Shakya, Sanjeev Kumar, and Mayank Goswami. Deep learning algorithm for satellite imaging based cyclone detection. *IEEE Journal of Selected Topics in Applied Earth Observations and Remote Sensing (JSTARS)*, 13:827–839, 2020.



- [122] Avanti Shrikumar, Peyton Greenside, and Anshul Kundaje. Learning important features through propagating activation differences. In *34th International Conference on Machine Learning (ICML)*, volume 70 of *Proceedings of Machine Learning Research*, pages 3145–3153, 2017.
- [123] Karen Simonyan and Andrew Zisserman. Very deep convolutional networks for large-scale image recognition. In *International Conference on Learning Representations (ICLR)*, 2015.
- [124] Daniel Smilkov, Nikhil Thorat, Been Kim, Fernanda Viégas, and Martin Wattenberg. Smoothgrad: removing noise by adding noise. *arXiv preprint arXiv:1706.03825*, 2017.
- [125] Dean R. Spitzer. What is a concept? *Educational Technology*, 15(7):36–39, 1975.
- [126] Jost Tobias Springenberg, Alexey Dosovitskiy, Thomas Brox, and Martin A. Riedmiller. Striving for simplicity: The all convolutional net. In *3rd International Conference on Learning Representations (ICLR)*, 2015.
- [127] Pierre Stock and Moustapha Cisse. Convnets and ImageNet beyond accuracy: Understanding mistakes and uncovering biases. In *European Conference on Computer Vision (ECCV)*, pages 498–512, 2018.
- [128] Jiamei Sun, Sebastian Lapuschkin, Wojciech Samek, and Alexander Binder. Explain and improve: LRP-inference fine-tuning for image captioning models. *Information Fusion*, 77:233–246, 2022.
- [129] Mukund Sundararajan, Ankur Taly, and Qiqi Yan. Axiomatic attribution for deep networks. In *34th International Conference on Machine Learning (ICML)*, pages 3319–3328, 2017.
- [130] Christian Szegedy, Wojciech Zaremba, Ilya Sutskever, Joan Bruna, Dumitru Erhan, Ian J. Goodfellow, and Rob Fergus. Intriguing properties of neural networks. In *2nd International Conference on Learning Representations (ICLR)*, 2014.
- [131] Adam D Thierer, Andrea Castillo O’Sullivan, and Raymond Russell. Artificial intelligence and public policy. *Mercatus Research Paper*, 2017.
- [132] Benjamin A Toms, Elizabeth A Barnes, and Imme Ebert-Uphoff. Physically interpretable neural networks for the geosciences: Applications to earth system variability. *Journal of Advances in Modeling Earth Systems*, 12(9):e2019MS002002, 2020.
- [133] Philipp Tschandl, Cliff Rosendahl, and Harald Kittler. The HAM10000 dataset, a large collection of multi-source dermatoscopic images of common pigmented skin lesions. *Scientific data*, 5(1):1–9, 2018.
- [134] Laurens Van der Maaten and Geoffrey Hinton. Visualizing data using t-sne. *Journal of Machine Learning Research*, 9(11), 2008.
- [135] Johanna Vielhaben, Stefan Blücher, and Nils Strodthoff. Sparse subspace clustering for concept discovery (SSCCD). *arXiv preprint arXiv:2203.06043*, 2022.
- [136] Oriol Vinyals, Igor Babuschkin, Wojciech M Czarnecki, Michaël Mathieu, Andrew Dudzik, Junyoung Chung, David H Choi, Richard Powell, Timo Ewalds, Petko Georgiev, et al. Grandmaster level in StarCraft II using multi-agent reinforcement learning. *Nature*, 575(7782):350–354, 2019.
- [137] Ulrike Von Luxburg. A tutorial on spectral clustering. *Statistics and computing*, 17(4):395–416, 2007.
- [138] Alvin Wan, Lisa Dunlap, Daniel Ho, Jihan Yin, Scott Lee, Henry Jin, Suzanne Petryk, Sarah Adel Bargal, and Joseph E Gonzalez. Nbd: Neural-backed decision trees. *arXiv preprint arXiv:2004.00221*, 2020.

- [139] Yalin Wang, Zhuofu Pan, Xiaofeng Yuan, Chunhua Yang, and Weihua Gui. A novel deep learning based fault diagnosis approach for chemical process with extended deep belief network. *ISA transactions*, 96:457–467, 2020.
- [140] Peter Welinder, Steve Branson, Takeshi Mita, Catherine Wah, Florian Schroff, Serge Belongie, and Pietro Perona. Caltech-UCSD birds 200. 2010.
- [141] Han Xiao, Kashif Rasul, and Roland Vollgraf. Fashion-mnist: A novel image dataset for benchmarking machine learning algorithms. *arXiv preprint arXiv:1708.07747*, 2017.
- [142] Yinchong Yang, Volker Tresp, Marius Wunderle, and Peter A Fasching. Explaining therapy predictions with Layer-Wise Relevance Propagation in neural networks. In *IEEE International Conference on Healthcare Informatics (ICHI)*, pages 152–162, 2018.
- [143] Chih-Kuan Yeh, Been Kim, Sercan Arik, Chun-Liang Li, Tomas Pfister, and Pradeep Ravikumar. On completeness-aware concept-based explanations in deep neural networks. *Advances in Neural Information Processing Systems (NeurIPS)*, 33:20554–20565, 2020.
- [144] Seul-Ki Yeom, Philipp Seegerer, Sebastian Lapuschkin, Alexander Binder, Simon Wiedemann, Klaus-Robert Müller, and Wojciech Samek. Pruning by explaining: A novel criterion for deep neural network pruning. *Pattern Recognition*, 115:107899, 2021.
- [145] Hongxu Yin, Pavlo Molchanov, Jose M Alvarez, Zhizhong Li, Arun Mallya, Derek Hoiem, Niraj K Jha, and Jan Kautz. Dreaming to distill: Data-free knowledge transfer via deepinversion. In *IEEE Conference on Computer Vision and Pattern Recognition (CVPR)*, pages 8715–8724, 2020.
- [146] Ruichi Yu, Ang Li, Chun-Fu Chen, Jui-Hsin Lai, Vlad I Morariu, Xintong Han, Mingfei Gao, Ching-Yung Lin, and Larry S Davis. Nisp: Pruning networks using neuron importance score propagation. In *IEEE Conference on Computer Vision and Pattern Recognition (CVPR)*, pages 9194–9203, 2018.
- [147] Matthew D. Zeiler and Rob Fergus. Visualizing and understanding convolutional networks. In *European Conference on Computer Vision (ECCV)*, volume 8689 of *Lecture Notes in Computer Science*, pages 818–833. Springer, 2014.
- [148] Bolei Zhou, Aditya Khosla, Àgata Lapedriza, Aude Oliva, and Antonio Torralba. Object detectors emerge in deep scene CNNs. In *3rd International Conference on Learning Representations (ICLR)*, 2015.
- [149] Bolei Zhou, Aditya Khosla, Agata Lapedriza, Aude Oliva, and Antonio Torralba. Learning deep features for discriminative localization. In *IEEE Conference on Computer Vision and Pattern Recognition (CVPR)*, pages 2921–2929, 2016.
- [150] Bolei Zhou, Yiyou Sun, David Bau, and Antonio Torralba. Interpretable Basis Decomposition for Visual Explanation. In *Computer Vision – ECCV*, volume 11212 of *Lecture Notes in Computer Science*, pages 122–138. Springer, 2018.
- [151] Luisa M. Zintgraf, Taco S. Cohen, Tameem Adel, and Max Welling. Visualizing deep neural network decisions: Prediction difference analysis. In *5th International Conference on Learning Representations (ICLR)*, 2017.

## A Appendix

In the appendix, additional information, descriptions, experiments and figures are presented. Section A.1 offers a detailed description related work and compares contemporary several XAI techniques. Section A.2 describes the datasets as well as models used in experiments. Section A.3 describes and compares different ways of computing, initializing and comparing attribution/relevance values. Section A.4 provides additional examples for the main paper describing the localization and understanding of concepts. In Section A.5, additional information about the sensitivity of reference sample selection regarding the maximization target is given, as well as further examples for class-conditional reference sample selection. Section A.6 shows the filter-flipping analysis for several additional layers of a VGG-16 network and ResNet34 model. In Section A.7 further details and results regarding the experiments where decisions are manipulated by feature ablation are given. Section A.8 provides additional information for the explanation-based image-retrieval experiments. In Section A.9 further results for the filter cluster analysis experiments are presented.

### A.1 Survey of Related Work

With the increased awareness that ML predictions need to be transparent, numerous approaches to XAI have emerged within the last decade (cf. [112, 33, 92, 1]). In this section, we reiterate specific landmark approaches which have influenced and motivated our own CRP and the extended, exemplary explanation pipeline. As stated in Section 1, the current XAI landscape can roughly be divided into *local* and *global* XAI. However, we are fully aware that a precise categorization is not always possible and the boundaries between have grown fuzzy with the ongoing development of the field, specifically with advances towards *glocal* XAI. Table 1 provides a summary of the related work discussed in Appendices A.1.1 to A.1.3 in terms of requirements and capabilities of recent methods of XAI.

Table 1: A comparison of selected local, global and glocal XAI approaches at a glance, considering the explanatory insight they provide and their specific requirements restricting the application. As explanatory capabilities it is considered whether explanations are class-specific (CS), sample-specific (SS), localized (L) in input space, providing examples (E) for learned latent concepts, or whether they can provide sample-specific feedback regarding latent features (F). The table indicates if an explainer exhibits specific *explanatory capabilities* partially (○) or fully (✓). We assess *specific requirements* in terms of necessity to control the training process training (T), the need for specific data and labels (D&L) (or just labels) for the method to be applicable, and the restriction to a certain architecture (A). Corresponding requirements restricting the applicability of an explainer are denoted by ✗ for hard, and ✘ for soft requirements.

XAI	Method	Explaining Capabilities					Requirements		
		CS	SS	L	E	F	T	D&L	A
Local	Gradient-based [123, 122, 129, 147]	✓	○	✓		✓			
	Mod.-Backpropagation [147, 11, 83, 118, 122]	✓	○	✓		✓			✘
	Perturbation / Surrogates [46, 105, 106, 76]	✓	✓	✓					
Global	Summit [53]	○			✓	○			
	Network Dissection [15]		✓	○	✓			✗	✗
	TCAV [60]	○	○		✓	○		✗	
Glocal	Feature Visualization [36, 94, 95]		○	○	✓	✓			
	TCAV + IG [115]	✓	○		✓	○		✗	
	StylEx [67]	✓	✓	✓	✓	○	✗		
	ProtoPNet [27]	✓	✓	○	✓	○	✗		✗
	<b>Ours</b>	✓	✓	✓	✓	✓			✘

#### A.1.1 Local XAI

Local post-hoc techniques aim to explain the classification of individual samples with no or little assumptions about the model’s architecture or its training procedure. For this purpose, attribution

maps are usually generated in the input domain, highlighting from *where* the model is deriving its inference outcome.

In our view, the current diversity of post-hoc techniques can be categorized as follows: Interpretable Local Surrogates and Perturbation Analysis [46, 105, 106, 76], and Backpropagation-based methods, including Modified Backpropagation [66, 147, 11, 83, 118, 122] and Gradient-based [123, 122, 129, 147] techniques.

Regarding explanations for neurons in the hidden space, (modified) gradient-based methods result in latent attributions as a by-product, which is not the case for methods based on learned explainable surrogate methods or input perturbation. However, (modified) gradient-based methods may require the model to be differentiable or contain particular layers, and thus have a soft requirement regarding the architecture.

**Interpretable Local Surrogates & Perturbation Analysis** Interpretable Local Surrogates replace the black-box model by a local surrogate model (e.g., a linear model) that locally approximates the model function for which an explanation is sought for. Since the surrogate has low complexity, interpretability is facilitated. Prominent methods include LIME [105], LORE [46] and Anchors [106]. While these approaches are model-agnostic, they have a high computational cost in terms of forward passes, since each explanation requires sampling and prediction of several data points as well as fitting a local surrogate. Moreover, explanations are no longer generated on the original model, which is why internal subprocesses and representations of the original model cannot be traced back and explained.

In perturbation analysis, such as Occlusion-based attribution [147], the input features are repeatedly perturbed while the effect on the model output is measured [147, 151, 40]. Some methods form a combination of occlusion and surrogates, such as SHAP [76]. Usually only the input is perturbed to calculate the influence on the output, but it is conceivable that intermediate layers are also perturbed to investigate the influence of single neurons. However, repeated perturbation leads to high computational cost, whereas backpropagation-based methods rely only on modified backward-passes to attribute all neurons.

**Gradient-based & Modified Backpropagation-based Methods** Early works [86, 12] show, that the gradient of the model predictor with respect to the input features can be used to visualize the sensitivity of the model regarding the input features. Specifically, saliency maps can be constructed that show in the input space the attribution of each input feature. In order to stabilize the resulting heatmaps, gradients can be multiplied with the input, thereby approximating the model function in first order Taylor approximation [122, 83]. Integrated Gradients [129] and SmoothGrad [124] further increases robustness against gradient noise by averaging the gradient through multiple attribution steps.

Modified backpropagation-based methods further modify the backpropagation process in order to improve explainability. These methods therefore view calculations made by a DNN as sequences of smaller layer-wise operations. Starting at the output, attributions are assigned layer after layer until the input is reached. These calculations may be implemented efficiently as a (modified) gradient backward pass. Prominent examples are DeepLIFT [122], Deconvolution [147], LRP [11] and Deep Taylor Decomposition [83]. Notably, LRP has been shown to achieve faithful intermediate attribution as can be seen in [18, 144]. These methods have the advantage that they efficiently provide attributions for intermediate neurons “for free” as a by-product, without any additional algorithmic extensions of the aforementioned. However, this by-product has usually been ignored in the literature except for a few works that use this information to directly improve specific aspects of deep models [81, 144, 128, 18], or regard them as proxy representations of explanations for the identification and eradication of systematic Clever Hans behavior [6].

While we assume differentiability as a given for DNNs in context of Table 1, modified backpropagation methods might require particular neural network building blocks to be present in order to be applicable, such as Global Average Pooling layers need to be part of the network for (Grad-)CAM [149, 118] to be applicable.

### A.1.2 Global XAI

Methods of global XAI aim at identifying concepts, visualizing them and making their general interaction within the model comprehensible. Unlike local XAI, global XAI focuses on representing the overall behavior of the model without revealing the exact decision process for individual samples. Note, that all concept discovery and visualization techniques listed here are compatible with the CRP framework proposed in this work.

**Neurons as Elementary Building Blocks for Explanations** It has been observed in numerous works [148, 94, 102, 16, 24, 44] that stable, human-understandable concepts emerge in neurons, although the DNN was not explicitly trained to use them. While low level neurons encode features like textures and edges, high level neurons conceptualize notions from simple objects to abstract emotions [148, 94]. Even the existence of multimodal neurons was reported that respond to a concept regardless whether it is shown as a photograph, a cartoon or just an image of the letters of a concept’s name [44]. Although literature [56] that examines adversarial examples suggests that models might use features imperceptible to humans, practical experience and experiments show that neurons in general convey human understandable concepts. In this regard we highlight the work of [15, 16] where the authors present an analytical framework called “Network Dissection” through which the semantic meaning of a filter kernel in a CNN layer can be identified, given densely labelled input data. In addition, the interested reader is referred to the work of Cammarata et al. [24] where an illustrative discussion of the foregoing topic is given.

**Feature Visualization** A large part of feature visualization techniques relies on Activation Maximization of single neurons or a linear combination thereof [148, 94, 102, 16, 24, 44], where in its simplest form, input images are sought that give rise to the highest activation value of a specific unit. Reference images can be generated synthetically using gradient descent, or alternatively found from a sample dataset by collecting neuron activations during predictions. While conceptually simple, preventing the emergence of adversarial synthetic examples became a main research endeavor. Several priors were proposed to guide optimization into realistic looking images, e.g., Transformation Robustness [87], Frequency Penalization [78], Preconditioning [94], and learning a natural prior from data distribution [90, 145] (more details in Section 2.3.1). However, simply because a stimulus leads to high activation does not necessitate that the stimulus is representative of a neuron’s function — adversarial examples are a prime example of this. The proposed Relevance-based sample (see Section 2.3.3) selection mitigates this issue by taking into account the context in which a neuron preferably activates.

All feature visualization methods such as [36, 94] generate human-understandable images that describe the concept of a neuron, but do not focus on concept interactions, or local analysis.

**Projection-based Visualization & Weight-based Graphs** The Activation Atlas [25] unites dimensionality reduction with feature visualization. Activation vectors for millions of input images are computed and projected onto a low-dimension space via UMAP [79] or t-SNE [134]. Feature visualization is then applied on averaged activation vectors to get a general sense of what concepts the network is utilizing. While t-SNE and UMAP may introduce neighborhood distortions, TopoAct [104] differs by utilizing a tool from topological data analysis. This way, they obtain a topological summary by preserving the clusters as well as relationships between them in the original high-dimensional activation space, revealing branches and loops. Focusing on the image domain, Summit and others [53, 75] draw weight-based graphs that show how features interact in a global, yet class-specific scale, but without the capability to deliver explanations for individual data samples: SUMMIT [53] measures on the one hand, which input samples lead to high activations, and on the other, which class is attributed to that input sample. Therefore, Summit allows to condition explanations on classes. Further, mean interactions between neurons of consecutive layers are found by investigating the activation flow. Thus, Summit allows inspecting the composition of features, but is thereby limited to a global analysis.

**Concept Discovery** Concept discovery methods rely on a priori known stimuli (via labeled data) to find concepts the model is sensitive to or is utilizing [103]. However, the use of labeled data carries

the risk of a human confirmation bias, that is tried to be minimized with the help of statistical calculations. Network Dissection [16] and Net2Vec [39] find concepts by measuring the alignment between upsampled convolutional channel map activation and a ground truth segmentation mask and thus require densely labeled data and a CNN architecture. Moreover, upsampling might result in imprecise localization. While Network Dissection focuses on single channels, concept vectors are searched for in Net2Vec.

Testing With Activation Vectors (TCAV) [60] introduces concept activation vectors that are obtained by training linear classifiers to distinguish between pre-categorized data of a priori known concepts, e.g., encoding conceptual differences. TCAV thus requires concept data and labels. These vectors are subsequently used to compute directional derivatives to measure the model’s prediction sensitivity to a specific class. These sensitivities can be used for a local analysis as well, leading to TCAV explanations being class, sample specific and requiring a differentiable model. The local explainability is however limited, as the sensitivities values are not stable due to the noisy gradient of DNNs. While TCAV relies on human-defined labels, the follow-up work ACE [43] clusters segments of the input image in an unsupervised way to generate proposal concept vectors.

### A.1.3 Glocal XAI

Glocal XAI aims to combine local and global XAI viewpoints in order to further improve explainability by minimizing the observer’s interpretation workload.

**Extending Concept Activation Vectors** Since sensitivity scores only measure the degree of change in output, and not the actual contribution to the final prediction as attribution methods do, Schrouff et al. [115] combine TCAV with Integrated Gradients and hereby enable local attribution, while preserving global explanation capabilities. As far as we understand, no heatmaps are computed for latent features in order to localize the concepts in input space. Moreover, ConceptSHAP [143] improves on the idea of TCAVs by defining a completeness-score with which concept vectors can be selected that contribute the most to a specific class. However, in both cases is the internal interaction between different concepts across layers as well as their localization in the input domain not observable.

**Attributing Internal Subprocesses** To the best of our knowledge, the possibility of using model internal attributions for sample-specific explanations of DNN subprocesses and feature interaction has been outlined first in the description of the Deep Taylor Decomposition Algorithm [83], which serves as the theoretical basis for LRP. Later, Interpretable Basis Decomposition [150] was introduced that decomposes the weight matrix of a higher layer into semantically interpretable basis sets. Multiplying with activation vectors, the individual contribution to the final classification can be computed. Grad-CAM [118], an extension of CAM [149], is used to generate low-resolution heatmaps for individual latent components. However, this approach is limited to an application to the last convolutional layer in connection with a global pooling operation. In addition, basic components are not learned in an unsupervised fashion, but need to be identified via predefined label sets. Finally, Olah et al. [95] have provided an informal proof-of-concept where the interaction between internal subprocesses and the localization of concepts via attribution maps have been demonstrated. However, the attribution algorithm is limited to a linear approximation between the potentially nonlinear hidden representation and input, and the visualization of concepts is restricted to Activation Maximization.

**Learning Generative Explainers** A different glocal approach based on Generative Adversarial Networks (GANs) is presented in the work of StyleEx [67]. Here, the authors propose to train a generative model to specifically explain multiple attributes that underlie classifier decisions in context of a particular input data point. To ensure that the learned GAN-based explainer uses similar representations as the classifier to be explained, the authors propose a training procedure, which tightly incorporates the classifier model. As a result, the features available to the GAN can therefore be manipulated in order to measure and understand their effect on the model’s

decision making. Further, a comparison of the original to the StyleEx-augmented image allows for localization of the manipulated feature in input space.

In summary, for StyleEx to be applied, the training process must be adapted. Manipulating the latent space of the GAN, synthetic images are generated, which capture the change in concepts due to the manipulation. Therefore, explanations are sample-specific and conditioned on a class output of interest. Further, concepts can be localized by the visible change of pixel-values in the input space.

**Analyzing Datasets of Attributions** The work of Chan et al. [26] proposed Melody, which groups similar local explanations together using techniques from information theory, thus generating a global overview of local explanations and consequently systematically learned concepts. The Spectral Relevance Analysis [69, 6] follows a similar idea and is built around the Spectral Clustering [80, 137] of a dataset of attribution maps for any arbitrary layer of representation in the network. Both methods are independent of the choice of local attribution algorithm. Another line of work processes attribution maps with methods from Inductive Logical Programming to identify and define relational concepts from post-hoc attributions [100, 101].

**Self-Explainable Models** In contrast to post-hoc methods that apply to any DNN model irrespective of architecture or training procedure, self-explainable models are specifically built or trained to maximize interpretability. Examples of self-explainable models include deep network architectures with an explicit top-level sum-pooling structure [27, 63, 98, 74], that reduces the attribution to a linear combination, making the reasoning process comprehensible. In particular, ProtoPNet [27] proposes to build a model based on a convolutional architecture and introduces a loss during the training process to force the generation of human-understandable concepts/prototypes. Using activation maps, concepts can be localized — resolution-wise limited by the size of the map. Thereby, single samples can be investigated as well.

Other architectures involve attention mechanisms [70, 13] whose inspection resembles attribution visualizations, or replacing a network’s final linear layer with a decision tree [138], as well as specifically controlling the flow and representation of features throughout the model [107]. Another line of work [38] creates explanation trees for models based on learnable predicate logic, providing access to explanations at different levels of abstraction in the prediction process.

While self-explainable models mitigate the requirement to use of post-hoc methods for gaining insight (for further arguments for explainable models see [109]), these methods can not be applied for explaining the inference of the more widely-spread and heavily used end-to-end trained black-box neural network models due to additional constraints imposed for the architecture or training procedures.

In contrast to aforementioned related work, our proposed method aims at making no additional assumptions about the model architecture, the availability of specific data- or label sets, or the structure of the learned latent space, while simultaneously providing human-aligned multifaceted explanations beyond the current state of the art. Conversely, this means that our contribution should be applicable to most purpose-built self-explaining model variants described in literature: Our method uses modified backpropagation approaches in order to efficiently calculate attributions in the latent space, and is thus weakly restricted to most of the currently used model architectures. For any sample, traditional heatmaps (conditioned on a class of interest) or concept-conditional heatmaps can be computed (localizing the concept in high resolution). Collecting the most relevant or activating samples for latent neurons from a source dataset of choice serves for obtaining visualizations of concepts in the hidden space. By conditioning the relevance flow on (multiple) concepts, concept compositions and superposition of concepts can be analyzed as well.

## A.2 Datasets and Models

**ImageNet** We utilized models pretrained on ImageNet [110] including the VGG-16 [123] architecture with and without BatchNorm layers provided by the PyTorch [97] library.

**Caltech-UCSD Birds 200** We fine-tuned a ResNet34 [50] pretrained on ImageNet on the Caltech-UCSD Birds 200 [140] dataset. Images are normalized with ImageNet values<sup>15</sup>. Further, Gaussian noise (zero mean, standard deviation of 0.05), random horizontal flips (probability of 0.5), random rotation (up to 10 degrees), random translation (up to 20 % in all directions) as well as a random scaling (between 80 and 120 %) is applied for data augmentation. After 100 epochs of training using Stochastic Gradient Descent (SGD) with a value for momentum of 0.9 and weight decay of 1e-4, we achieved 76 % top-1-accuracy on the test set.

**ISIC 2019** We employ the VGG-16 model with pretrained weights on ImageNet from the PyTorch model zoo to train on the ISIC 2019 dataset. The model is trained over 100 epochs, using an SGD optimizer with a learning rate of 0.001, momentum 0.9 and batch size of 32. ISIC 2019 does not offer a pre-defined labeled test set. Therefore, 10% of the original training set is split off in order to evaluate the model’s performance. The model achieves a final test accuracy of 82.15%.

**Adience** We fine-tuned a VGG-16 without BatchNorm layers pretrained on ImageNet on the Adience dataset for age estimation [35]. For training, folds 0,1,2 and 3 were selected and fold 4 was used as a test set. Images are normalized with ImageNet values and linear transformations were applied as augmentation techniques. After training for 10 epochs with the Adam [62] optimizer and a batch size of 32 with a learning rate of 2e-4 and standard hyperparameter values in the PyTorch library, we achieved a top-1-accuracy of 51% on the test set.

**PhysioNet MIT-BIH Arrhythmia** The original training data is provided by PhysioNet MIT-BIH Arrhythmia [85] and consists of ECG recordings from 47 different subjects, where each beat was annotated by at least two cardiologists. The work [58] reordered the dataset by isolating the ECG lead II data, splitting and padding beats into a fixed size of 150 at a sampling rate of 125 Hz and finally grouping all annotations into five different categories in accordance with the *Association for the Advancement of Medical Instrumentation* (AAMI) EC57 standard [41].

Preprocessing steps include subtracting the mean value of 0.2115 and standardizing by dividing with 0.2462. As optimizer, RMSprop [52] with a learning rate of 1e-4 and weight decay of 1e-6 were chosen. Since the data set is unbalanced, we used cross entropy loss with class balancing. We trained the model for 25 epochs and achieved on the test set a top-1-accuracy of 89 %.

The model consists of three feature extraction blocks, each composed of a 1D-Convolutional layer with 64 channels and kernel size 7, followed by a ReLU non-linearity and a 1D-Max-Pooling layer with kernel size 3 and stride 2. After feature extraction, a 1D-Average-Pooling layer with kernel size 7 and a flatten operation direct the activations into a regression head. The regression head consists of two linear layers with 64 and 32 neurons as well as a ReLU non-linearity. Finally, a linear output layer with 5 neurons concludes the architecture.

**Fashion-MNIST** A LeNet-5 [72] was trained on the Fashion-MNIST [141] dataset. Preprocessing included only normalizing the input interval into the range of [0,1]. As optimizer, Adam was chosen with standard PyTorch parameters. After training for 5 epochs, a top-1-accuracy of 88 % on the test set was achieved.

---

<sup>15</sup>Subtraction of mean values [0.485, 0.456, 0.406], followed by a normalization of standard deviation values [0.229, 0.224, 0.225] over the red, green and blue color channels respectively, as per specifications at <https://pytorch.org/vision/stable/models.html>.



### A.3 Computation and Comparison of Relevance Values

**Distribution Rules** In this work, we compute CRP attribution scores for ResNets and VGG-16 models using the recommended [64] composite LRP $_{\varepsilon-z^+-b}$ -rule<sup>16</sup> after model canonization steps applied [55, 47, 88] as implemented in the `zennit` [5] package for PyTorch [96]. The LRP $-\varepsilon$ -rule is defined as

$$R_{i \leftarrow j}^{(l, l+1)} = \frac{z_{ij}}{z_j + \varepsilon \cdot \text{sign}(z_j)} R_j^{l+1} \quad (32)$$

where  $z_{ij} = w_{ij}x_i$  with inputs  $x_i$  from the lower layer and weights  $w_{ij}$  of the linear layer with outputs  $z_j = \sum_i w_{ij}x_i$ . It ensures that each neuron receives the attribution value, that it contributed to the output. The added  $\varepsilon \in \mathbb{R}^+$  stabilizes the division of the denominator. Note that for this purpose, the definition of the sign function is altered such that  $\text{sign}(0) = 1$ . The  $\varepsilon$ -rule is in ReLU networks highly similar to the multiplication of the input times its gradient wrt. the output [64], but not identical, leading to different attribution maps [88]. These attribution values for different predictions can now, in principle, be compared. However, due to its similarity to gradient-based attribution computation, the LRP $-\varepsilon$ -rule may result in noisy attributions in very deep models, where gradient shattering and noisy gradients appear [14]. Thus, the computation of the LRP $-\varepsilon$ -rule may not result in meaningful attributions in models with a high number of layers and ReLU activations. An alternative approach is to combine multiple propagation rules, so-called composite rules, which result in attributions that are less influenced by a noisy gradient: the LRP $_{\varepsilon-z^+-b}$ -rule is an established best practice [64, 82] to keep LRP attribution maps informative, readable and representative while combating gradient shattering effects.

Here, applying the LRP $-b$ -rule to the first convolutional layer smoothes the attribution map in input space and yields an invariance against input normalization effects. The LRP $-z^+$ -rule, on the other hand, operates on the remaining convolutional layers and LRP $-\varepsilon$ -rule is utilized in standard MLP layers. The LRP $-b$ -rule is defined as

$$R_{i \leftarrow j}^{(l, l+1)} = \frac{1}{\sum_i 1} R_j^{l+1} \quad (33)$$

Using the  $b$ -rule, relevance of upper-level neuron  $j$  is equally distributed to all connected lower-level neurons disregarding any influence of learned weights or input features. The LRP $-z^+$ -rule is given as

$$R_{i \leftarrow j}^{(l, l+1)} = \frac{(w_{ij}x_i)^+}{z_j^+} R_j^{l+1} \quad (34)$$

by only taking into account positive contributions  $z_j^+ = \sum_i (w_{ij}x_i)^+$  with  $(\cdot)^+ = \max(0, \cdot)$ .

**Initialization** The calculation of an attribution map starts with an initial relevance value at the output neuron. A meaningful and canonical choice is the model output activation of the neuron representing the class of interest to be explained. All intermediate relevance values are then proportional to the initial relevance value, since LRP is a layer-wise linear distribution process, cf. Equation (5).

We recommend to start propagation with the output values as they are, i.e.,  $R_j^L = f_j(\mathbf{x})$ , for an output (set)  $j$  of choice. Thus, the relevance of all neurons is proportional to the confidence of the model prediction. As a result, when ranking the samples of a dataset for representing the concept of a filter, RelMax will give preference to samples that the model predicted with highest confidence. This behavior is advantageous when calculating class-conditional reference samples or when the original dataset is *not* expanded with additional datasets as demonstrated in (see Section 3.2).

**Canonization** Since rule-based attributions, such as LRP and CRP, are not implementation invariant, canonization restructures a model into a functionally identical equivalent of alternative design to which established attribution rules can be applied in an improved manner. Canonization

<sup>16</sup>read: "epsilon-plus-flat" rule

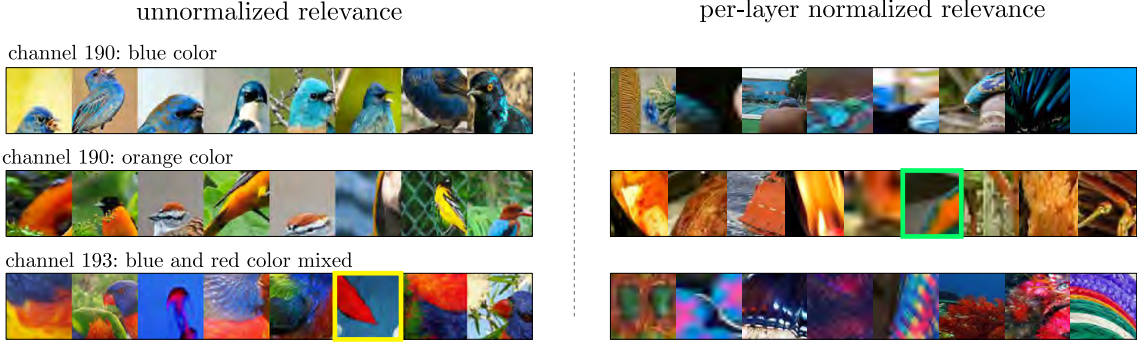


Figure A.1: Reference samples selected using RelMax with different normalization techniques. Depicted are channel 190, 117 and 193 in layer `layer3.0.conv1` of a ResNet34 trained on Caltech-UCSD Birds 200. The  $\mathcal{X}_{\text{g}_{\text{max}}}^{\text{rel}}$  are drawn from the Birds dataset, merged with ImageNet data. (*Left*): Reference Samples selection without layerwise normalization favors samples that the model predicted with high confidence. Samples from ImageNet dataset are marked with a yellow border. (*Right*): Using per-layer relevance normalization, samples outside the training distribution are taken into account more often. Samples from Caltech-UCSD Birds 200 dataset are marked with a green border.

efforts usually concentrate on replacing the BatchNorm layer [55, 47] or the handling of skip connections [19]. By merging BatchNorm layers into a neighboring linear layer, significant improvements in terms of explanations can be achieved [88].

**Per-layer Relevance Normalization** We generally recommend starting the relevance back-propagation process with the output of a network element. However, when reference datasets are extended in order to gain additional perspectives on the concepts to be understood, out-of-distribution data (or data the model has not sufficiently fit to) will produce low output confidences which serve as low initial relevance values. This will result in the added reference data from alternative source to not be ranked highly as meaningful representations for latent concepts. In order to be in this case independent of the model confidence of individual predictions, the relevance attributions  $R^{(l)}(\mathbf{x}|\theta_c)$  with condition  $\theta_c$  can be normalized at each layer  $l$  as

$$R_{\text{norm}}^{(l)}(\mathbf{x}|\theta_c) = \frac{R^{(l)}(\mathbf{x}|\theta_c)}{\sum_k |R_k^{(l)}(\mathbf{x}|\theta_c)|} \quad (35)$$

Thus, individual attributions are first divided by the absolute sum of relevances at layer  $l$  to ensure that each attribution is bounded in  $[-1, 1]$ . The concept importance becomes independent of the output of the model, while maintaining class-specificity. This procedure facilitates the comparison of concept importance for different samples during RelMax, if the original dataset is expanded with additional, external datasets. In our case, ImageNet images are fed into a model trained for bird categorization only. These ImageNet images will then be considered more frequently as representations for latent concepts with per-layer normalization than without layerwise normalization. It is to note, that class conditional relevance computation *without ground truth labels* has to be applied with caution, because the natural filter functionality, that the model confidence provides, is lost via per-layer relevance normalization. However, if (matching) ground truth labels are available, class conditional relevance could be computed for true labels only instead.

The qualitative difference of reference samples selected using RelMax with and without per-layer relevance normalization is illustrated in Figure A.1. Here, layer `layer.3.0.conv1` of a pre-trained ResNet34 model trained on Caltech-UCSD Birds 200 is analyzed. The dataset is extended with additional ImageNet samples to increase reference sample variety. Figure A.1 (*left*) depicts reference samples selected without per-layer relevance normalization, i.e., favoring samples that achieve highest model confidence. As a consequence, samples that belong to the original training data are visualized more often, illustrating how the filter is *actually* utilized. On the other hand, Figure A.1 (*right*) depicts reference samples selected with per-layer relevance normalization, i.e.

selecting samples independent of model confidence. As a result, samples outside the training data are shown more often, providing examples more focused on the concept itself and with less distracting information increasing model output confidence in context of other concepts. The choice of applying layer-wise relevance normalization provides the option for an additional perspective on the visualized concept representations

**Practical Implementation** The library `zennit` [5] was used to perform the experiments. It takes advantage of PyTorch’s autograd module to compute gradients in computational graphs. `zennit` modifies the backpropagated gradient in such a way that they are replaced by attribution values for CRP instead. We provide a `zennit`-based open source package for CRP and RelMax computations for PyTorch and Python at <https://github.com/rachtibat/zennit-crp>.

### A.3.1 How to Read Heatmap Visualizations

In order to interpret heatmaps, it is to note that attributions are bound between  $[-1, 1]$ , by normalizing all attribution scores of the representation layer of choice with the maximum of the absolute value over all dimensions. The thus normalized values can then be visualized using color maps, i.e., in our case the `bwr` (blue white red) colormap available from `matplotlib`, as visualized in Figure A.2. Accordingly, the maximum (positive) value of the color map was set to 1 and the minimum (negative) to -1. Zero-valued attributions, identifying network elements neutral to the analyzed inference processes are shown in (near) white color.

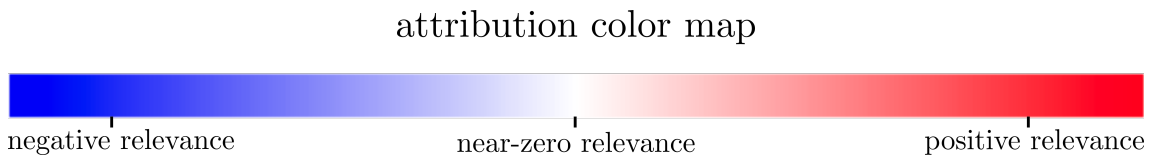


Figure A.2: Color map `bwr` (blue white red) assigns blue color to negative values, white color to near-zero values and red color to positive values.

## A.4 Additional Examples: Concept Localization and Understanding

In the following, additional examples are shown for sections regarding concept localization and understanding.

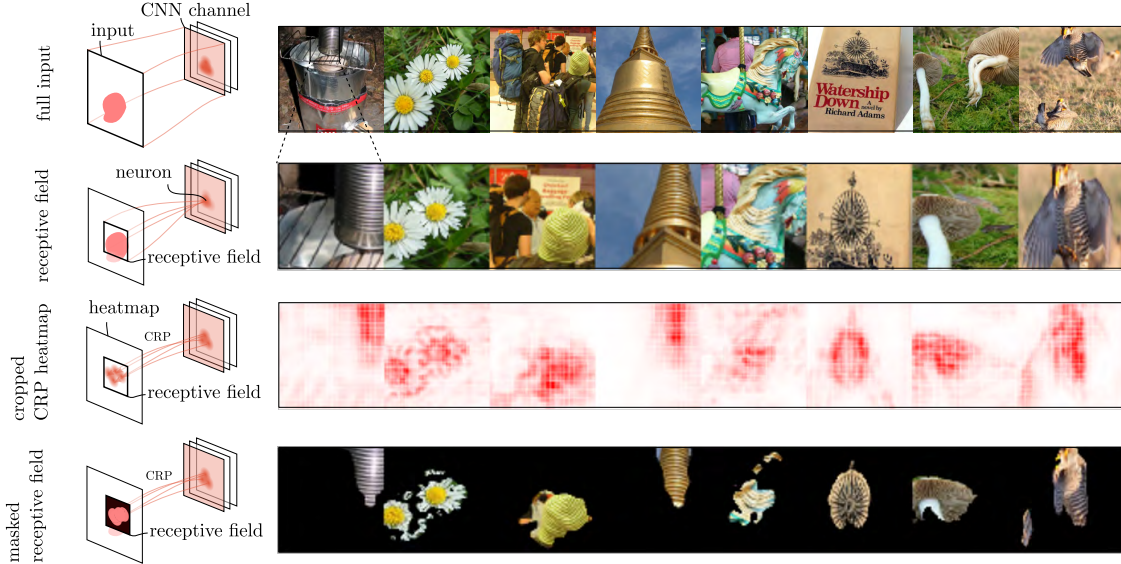


Figure A.3: Improving concept visualization and localization using reference samples. (*Top row*): Full sized reference samples in  $\mathcal{X}_{s_{\max}}^{\text{act}}$  sorted accordingly to their activation. (*2nd row*): The same reference samples cropped to the receptive field of the most activating neuron. (*3rd row*): CRP heatmap for filter output of cropped reference samples. (*Bottom row*): Cropped reference samples masked wrt. CRP heatmap and a threshold  $\tau$  of 40 % of the maximal heatmap value. This figure shows additional results corresponding to Figure 8 in Section 2.3.5.

**From Full-sized Reference Samples to Relevance-Masked Receptive Fields** First, another example of Figure 8 in Section 2.3.5 showing the process of optimizing concept visualization using reference samples is presented in Figure A.3. Here, the process from full-sized input images to the receptive field and eventually to masked reference samples using conditional relevances is depicted.

**Investigating Concepts in Input Regions of Interest** Defining a region of interest in input space, conditional relevances from CRP can be aggregated channel-wise in the region and thereafter sorted regarding their relevance value, as discussed in Section 3.3. Thus, it is possible, to extract the most relevant channels and their concepts for the region. In the following, two further examples besides the one in Figure 16 are presented.

In the first example shown in Figure A.4 a “Lazuli Bunting” is predicted by a ResNet34 model trained on the CUB birds dataset. Here, the channels of layer `layer3.0.conv1` are analyzed. The first analyzed region  $\mathcal{I}_1$  covers the bird’s wing (*left*). Here, “blue color” and concepts for the stripe-like structure of the feathers are most relevant. The second region  $\mathcal{I}_2$  covers the bird’s eyes and beak. Here, again, “blue color” is most important. Further, concepts regarding the round black eye of the Lazuli Bunting are second and third most relevant.

A “Blenheim Spaniel” dog is predicted by a ResNet34 model pretrained on ImageNet in the second example. The analyzed layer is `layer3.0.conv2`. In the first region  $\mathcal{I}_1$ , concepts for the dog’s snout are investigated. Here, color-concepts such as “black and white” capturing the black nose, and “brown and white” describing the fur pattern are most relevant. The second region  $\mathcal{I}_2$  covers part of the dog’s head. Here, the “brown and white” and “long-haired fur” concepts capturing the fur are most relevant. Further, a “blue spot” concept focusing on the eye part is relevant as well.

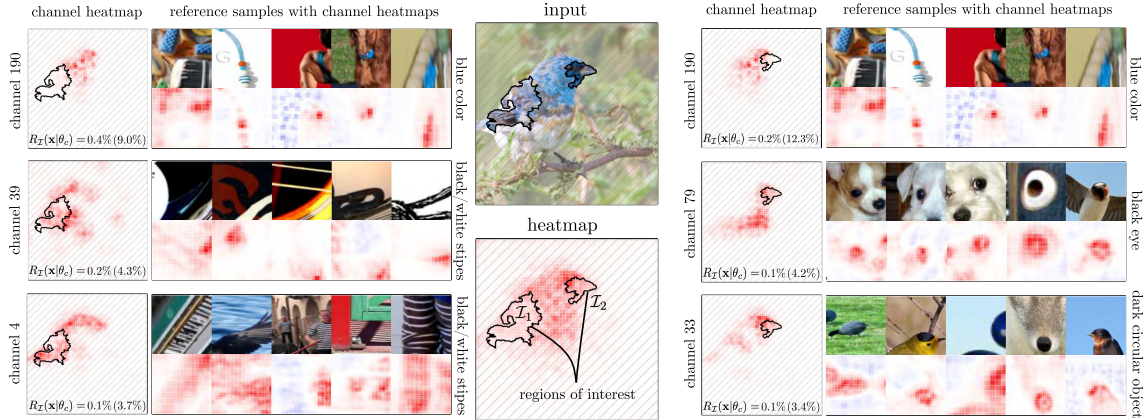


Figure A.4: Relevance aggregation inside superpixels allows investigation of the most relevant channels for chosen regions of interest  $\mathcal{I}_i$ . The top-3 most relevant channels for the prediction of class “Lazuli Bunting” regarding two superpixels are shown with channel heatmaps and reference samples. (*Left*): Region  $\mathcal{I}_1$  covers the bird’s wing. Here, “blue color” and concepts for the stripe-like structure of the feathers are most relevant. For each channel, the relevance relative to the global relevance as well as superpixel relevance (in parentheses) is given. (*Right*): Region  $\mathcal{I}_2$  covers the bird’s eyes and beak. Here, again, “blue color” is most important. Further, concepts regarding the round black eye of the Lazuli Bunting are second and third most relevant. This figure corresponds to Figure 16 in Section 3.3.

**Concept Atlases and Conditional Heatmaps** Three additional examples on how channel-conditional heatmaps and concept atlases can aid in the localization and understanding of channel concepts is shown in Figures A.6, A.7 and A.8.

In the first example, a “Green Lizard” is predicted by a VGG-16 BN model trained on ImageNet. Regarding the channels located in the layer `features_40`, glocal analysis shows, that concepts exist which refer to lizard scales (channel 469 and 161), “green vegetation” (35), “dark spot with bright border” (89) and “object on brown branches” (316).

In the second example shown in Figure A.7, class “swimming trunk” is predicted by the same model as in the previous example. The sample shows a man standing in the water with a surfing board in his hands. Glocal analysis shows here, that concepts regarding the person’s upper body, skin and hair (channels 222, 44 and 389), as well as the water (channels 22 and 187) are primarily used for the prediction. This is a sign of unreliability, as no concepts regarding the swimming trunk directly seem to be used.

In a third example shown in Figure A.8, a pullover is predicted by a LeNet-5 model trained on Fashion MNIST. From the conditional heatmaps and concept atlas it can be seen, that the model has learned concepts for specific spatial parts of the pullover. Channels 4 and 13 activate on the right side of the pullover, whereas channel 2 localizes the left sleeve. Further, channel 14 is used to detect the bottom part of the pullover, and channel 11 for the shoulder region and bottom left.

In the following, an alternative way to compute a concept atlas is discussed. Specifically, a concept atlas can be alternatively computed by calculating the most relevant and second-most relevant channels for each pixel instead of super-pixels. This way, no super-pixels need to be computed beforehand. As is shown in Figure A.9, the single-pixel concept atlases are more fine-grained. However, if too many concepts are used or heatmaps are noisy, this might result in incomprehensible concept atlas visualizations. In these cases, it is more sensible to use the super-pixel for more robust concept rankings through aggregations over regions.

Considering only *relevant* super-pixels for improving visualization clarity, we further introduced a threshold on the relevance density of super-pixels. Specifically, the threshold is set to one tenth of the maximal relevance density. Here the density is calculated for super-pixels as the mean relevance, i.e., the sum of relevance inside a super-pixel divided by the number of pixels. For single pixels, the density is approximated using a Gaussian filter with kernel size of  $29 \times 29$  px and standard deviation of 4.7. The effect on concept atlas readability and clarity is shown in Figure A.9.

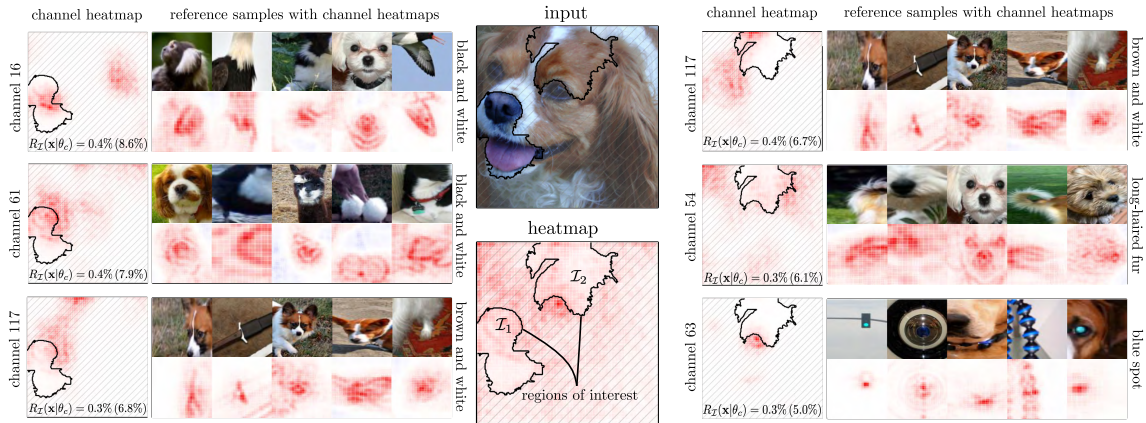


Figure A.5: Relevance aggregation inside superpixels allows investigation of the most relevant channels for chosen regions of interest  $\mathcal{I}_i$ . The top-3 most relevant channels for the prediction of class “Blenheim Spaniel” regarding two superpixels are shown with channel heatmaps and reference samples. (*Left*): Region  $\mathcal{I}_1$  covers the dog’s snout. Here, color-concepts such as “black and white” capturing the black nose, and “brown and white” describing the fur pattern are most relevant. For each channel, the relevance relative to the global relevance as well as superpixel relevance (in parentheses) is given. (*Right*): Region  $\mathcal{I}_2$  covers part of the dog’s head. Here, the “brown and white” and “long-haired fur” concepts capturing the fur are most relevant. Further, a “blue spot” concept focusing on the eye is relevant as well. This Figure corresponds to Figure 16 in Section 3.3.

As can be seen in the figure, the concept atlases with threshold stronger focus on the detected objects, where most relevance is located. It is to note, that densities instead of relevance values are used for the threshold, thereby addressing the issue, that concepts can be similarly important but spatially expanded to different degree. Using relevance values instead of densities, overall relevant, but spatially expanded concepts are more likely to be hidden, as individual relevance scores are lower.

**Attribution Graphs** With the selection of a specific neuron or concept, Concept Relevance Propagation allows to investigate, how relevance flows from and through the chosen network unit to lower-level neurons and concepts, as is discussed in Section 2.2.1. This gives information about which lower-level concepts carry importance for the concept of interest and how it is composed of more elementary conceptual building blocks, which may further improve the understanding of the investigated concept and model as a whole. Alternatively to Figure 17, another graph is shown in Figure A.10 for the classification of a Green Lizard using a VGG-16 BN model pretrained on ImageNet. Please note, that in Figure A.6, the spatial concept composition is investigated for the same sample. As illustrated by the graph, the concept of interest “green lizard scales and legs” in layer `features.40` is dependent on several sub-concepts located in layers `features.37` and `features.34`. Concretely, relevant sub-concepts regarding the lizard’s skin (e.g., “orange peel texture” and “warm color, black spots”) and body parts (e.g., “lizard feet” and “round eye with dark pupil”) can be identified.

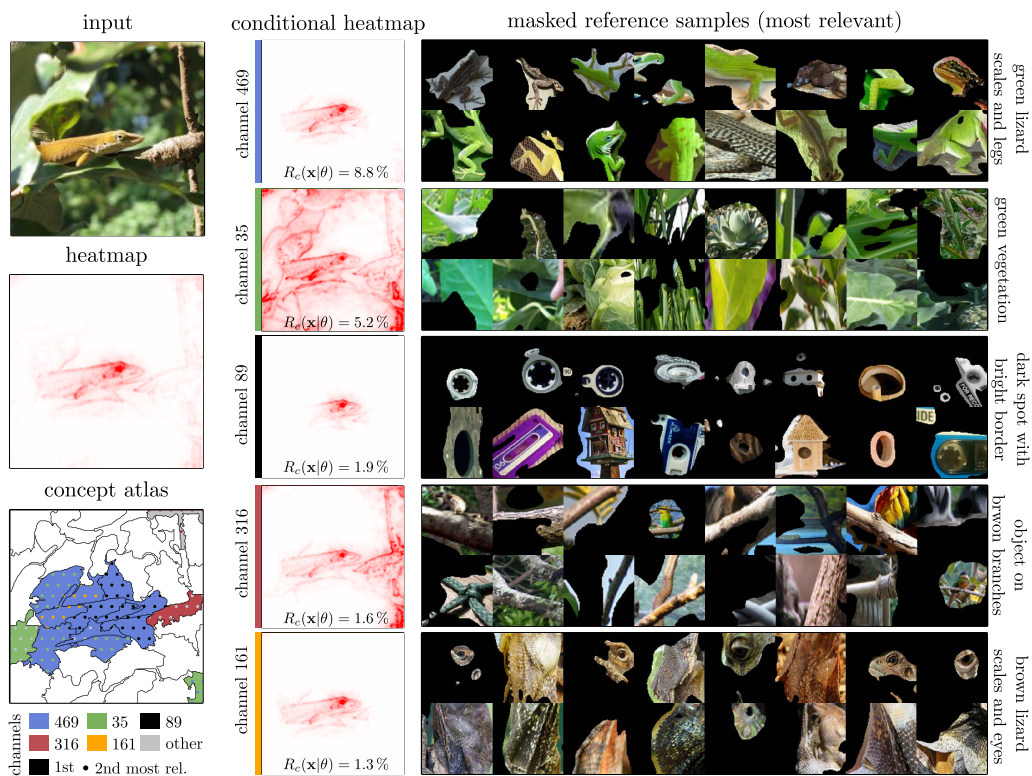


Figure A.6: Channel-conditional heatmaps enable the localization and understanding of channel concepts. CRP relevances can further be used to construct a concept atlas, visualizing which concepts dominate in specific regions in the input image defined by super-pixels. For the prediction of a “Green Lizard” using a VGG-16 model with BatchNorm layers, the most relevant channels can be identified with concepts concerning lizard scales (channel 469 and 161), “green vegetation” (35), “dark spot with bright border” (89) and “object on brown branches” (316). This figure corresponds to Section 3.3.

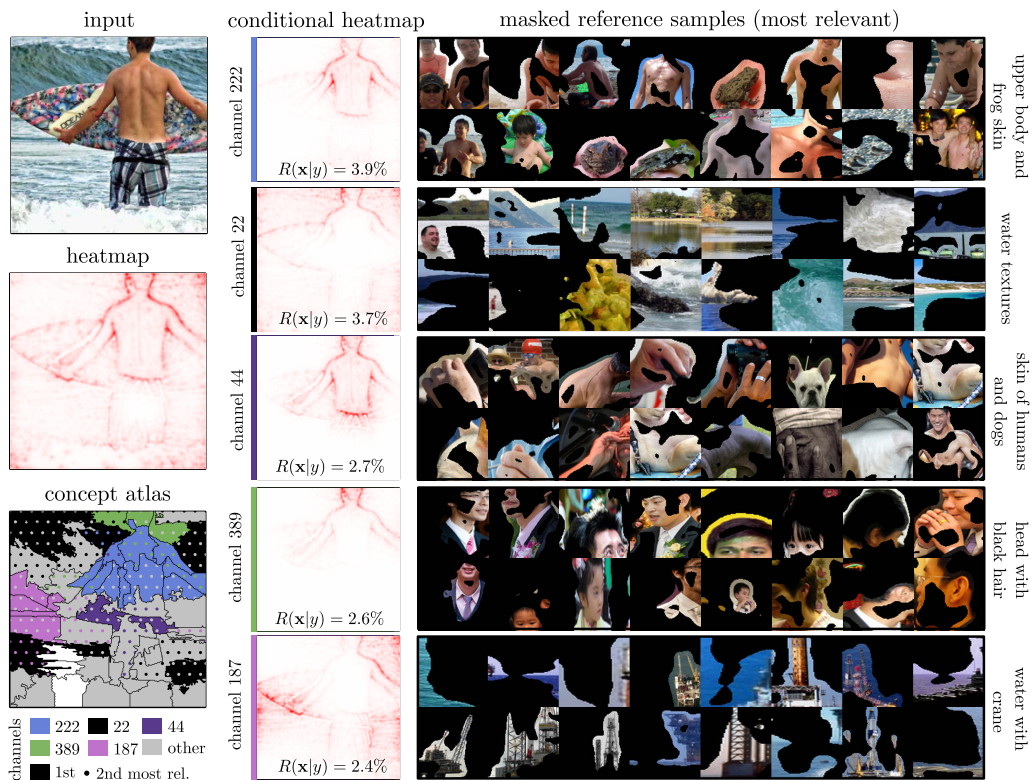


Figure A.7: Illustrating the five most relevant filters in layer `features.28` of VGG-16 trained on ImageNet for the prediction of “swimming trunk” with conditional heatmaps and a concept atlas. The input image shows a man standing in the water with a surfing board in his hands. Concepts regarding the person’s upper body, skin and hair (channels 222, 44 and 389), as well as the water (channels 22 and 187) are primarily used for the prediction — indicating a CH behavior. This figure corresponds to Section 3.3.



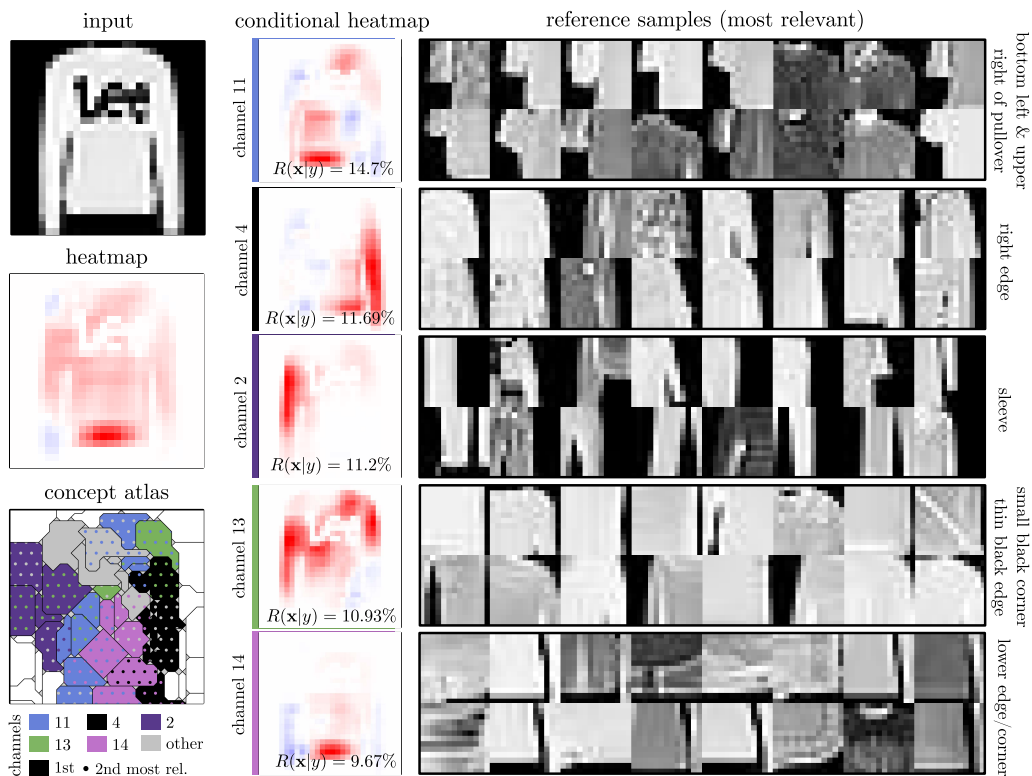


Figure A.8: Illustrating the five most relevant filters in layer 13 of a LeNet model trained on Fashion MNIST for the prediction of class “pullover”. From the conditional heatmaps and concept atlas it can be seen, that the model has learned concepts for specific spatial parts of the pullover. Channels 4 and 13 activate on the right side of the pullover, whereas channel 2 localizes the left sleeve. Further, channel 14 is used to detect the bottom part of the pullover, and channel 11 for the shoulder region and bottom left. This figure corresponds to Section 3.3.

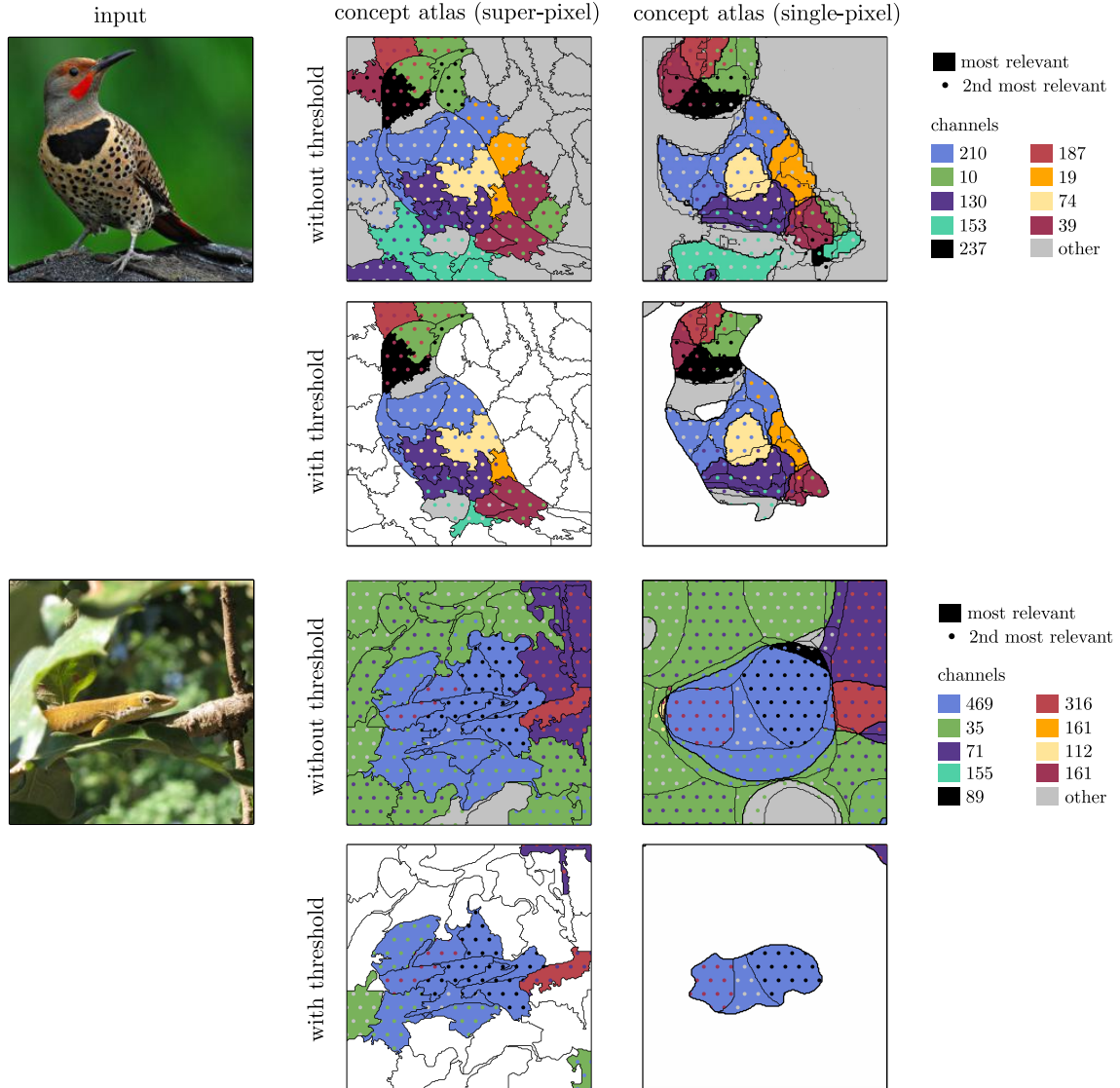


Figure A.9: Alternatively to using super-pixels based on image statistics, a concept atlas can also be constructed from single pixels (i.e., single-pixel sized superpixels). For both cases, concept atlases can be filtered with a threshold targeting relevance density, in order to focus on the most relevant input regions. Shown are concept atlases with super-pixels (*center*) using the same samples as shown in Figures 15 and A.6, but using a higher number of channels (9 compared to 5) and single-pixels as well (*right*). The single-pixel concept atlases can resolve smaller-scale features. This might however result in noisy atlases if a lot of concepts are used or relevance heatmaps are grainy. Furthermore, the difference of applying thresholding is shown. Here, a threshold results in more localized concept atlases, focusing on the detected objects themselves.

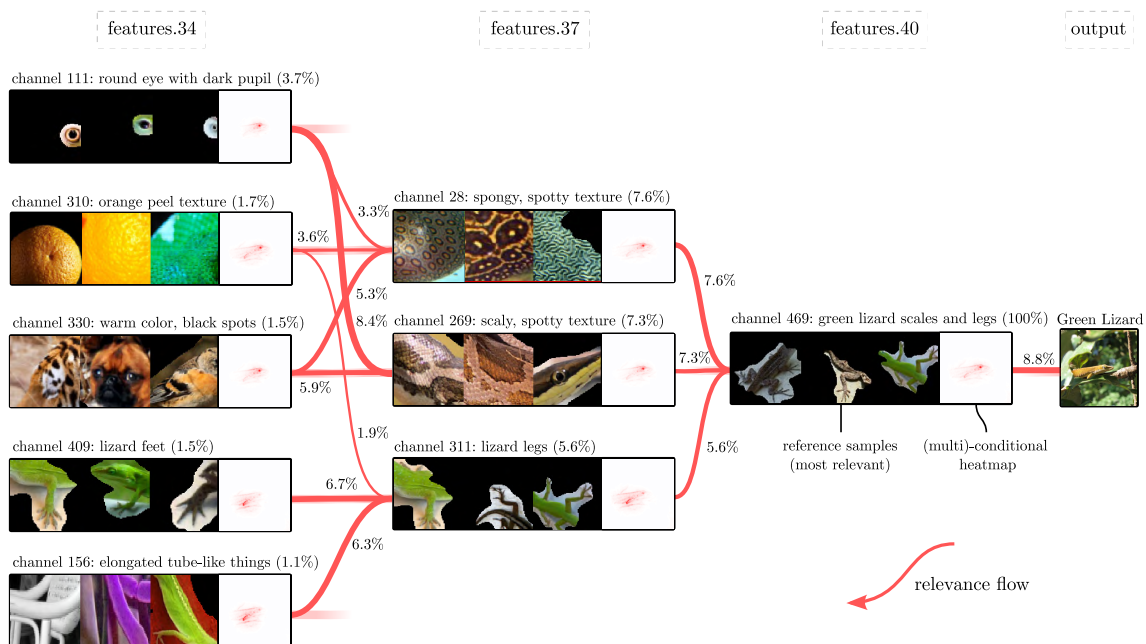


Figure A.10: Attribution Graphs can be used to visualize relevant concepts in lower layers for a concept of interest regarding a particular prediction outcome, and thus improves concept understanding. Shown are relevant (sub)-concepts in **features.34** and **features.37** for concept “green lizard scales and legs” in **features.40** of a VGG-16 BN model trained on ImageNet for the prediction of class “Green Lizard”. See Figure A.6 for a spatial concept composition analysis of the same sample. The relevance flow is highlighted in red, with the relative percentage of relevance given that flows to the lower-level concept. For each concept, the channel is given with the relative overall relevance score (wrt. channel 469 in **features.40**) in parentheses. Following the relevance flow, concept “green lizard scales and legs” is dependent on concepts describing the skin (e.g., “orange peel texture” and “warm color, black spots”) and body parts (e.g., “lizard feet” and “round eye with dark pupil”). This figure corresponds to Figure 17 in Section 3.4.

## A.5 Additional Results: Reference Sample Selection

This section of the appendix shows additional results for the Section 3.1 beginning with more examples illustrating the sensitivity of reference samples regarding the sorting criteria, i.e., activation or relevance. Thereafter, further examples for the class-conditional reference sample selection are shown.

### A.5.1 Maximization Target Sensitivity

In Section 3.1, we have discussed, that reference samples depend on the maximization target. Here, activation-based approaches have shown to be more sensitive, whether the maximization target is computed using the maximum value or channel map sum.

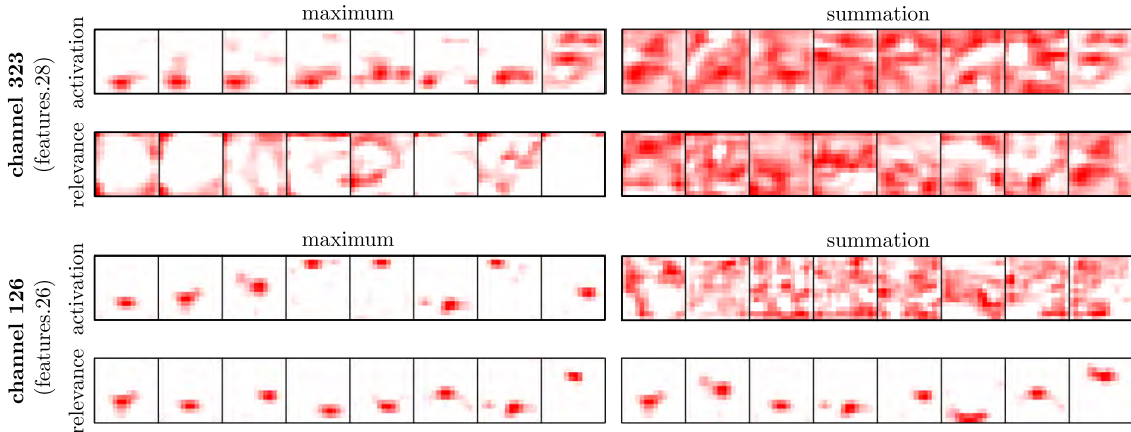


Figure A.11: Extension of Figure 11 showing the distribution of activation scores or relevance inside the channel for samples collected using Relevance Maximization and the activation distribution for samples collected using Activation Maximization, i.e., the quantities serving as respective criteria for reference sample selection. (*Top*): Channel 323 from layer `features.28` is mostly used in a maritime setting based on relevance-sorted reference samples. It can be seen that the concept is hereby spatially extended (covers large parts of the input sample). Sorting regarding maximum activation value, on the other hand, results in edge-case samples. (*Bottom*): Channel 126 from layer `features.26` is most often used to detect bow ties or neck ties based on the relevance-sorted reference samples. It can be seen that the concept is spatially localized (covers small parts of the input sample). Sorting regarding summation activation, on the other hand, results in edge-case samples. This figure corresponds to Section 3.1.

In Figure A.11 we expand upon the example in Figure 11 by additionally showing the activation maps for each reference sample. This further illustrates, that relevance-based criteria are more stable regarding the spatial size of a concept.

A second example is depicted in Figure A.12 showing two channels of a VGG-16 model trained on ImageNet in layer `feature.28`. Channel 265 is used to detect thin lines as found in electric masts or ship ropes, as relevance-based reference samples suggest. Such lines are also found in images of vehicles, as maximum activation-based sorting shows. Here also, activation-based sampling strongly differs qualitatively in the set of reference samples. Channel 245 is used to detect repeating patterns of keys, found in pianos or xylophones. This is shown by relevance-based sorting. The keys in pianos and xylophones are separated by a darker gap (xylophone) or black key (piano). Such a contrastive blending in color is also found in dogs with bright fur, as can be seen in maximum-activation-based samples. All in all, these examples further show, that relevance-based criteria are more stable regarding the spatial size of a concept.

### A.5.2 Class-Conditional Reference Sample Selection

In order to reduce the reference sample set variety and focus on one specific class, reference samples can be conditioned on a class of interest. In the following, additional examples for Figure 13

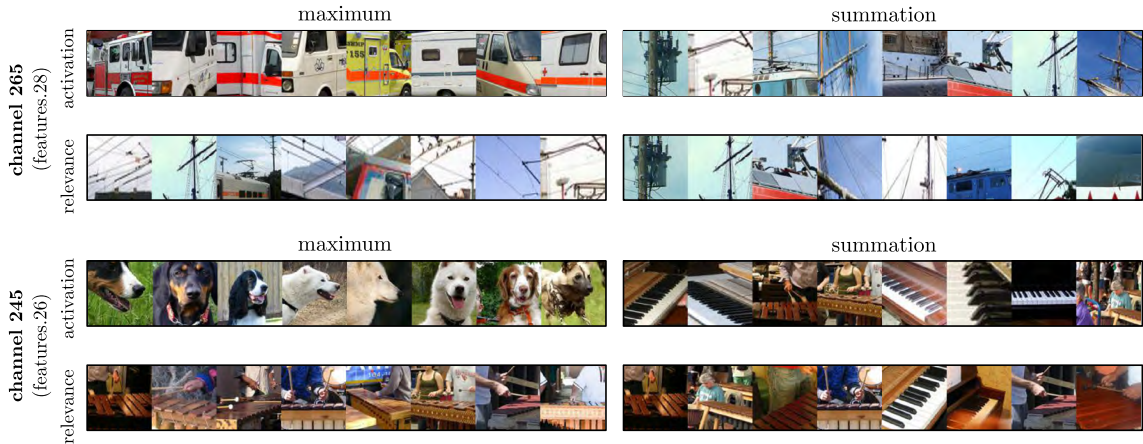


Figure A.12: Reference images collected using Activation Maximization and Relevance Maximization via summation, or taking the maximum activations with additional channel maps. (*Top*): The relevance-based reference samples suggest, that channel 265 is used to detect thin lines as found in electric masts or ship ropes. Such lines are also found in vans, as maximum activation-based sorting shows. (*Bottom*): Channel 245 is used to detect repeating patterns of keys from, e.g., pianos or xylophones. This is shown by relevance-based sorting. The keys in pianos and xylophones are separated by a darker gap (xylophone) or black key (piano). Such a contrastive blending in color is also found in dogs with bright fur, as can be seen in maximum-activation-based samples. This figure corresponds to Section 3.1 and highlights that activation-based sorting is more sensitive in regard to the maximization target. Figure A.13 shows the to these examples corresponding activation- and relevance attribution maps.

discussed in Section 3.2 are shown.

In the first example shown in Figure A.14, we show class-specific relevance-based reference samples for the time series use case in Section 3.5. Here, two different kinds of signal peaks can be identified as concepts. Channel 42 in layer `features.6` is relevant for detecting strong peaks with a period of constant signal before. Channel 23 of `features.3` is relevant for peaks which already start with a signal of about 50%. Conditioning the reference samples on specific classes, the concepts use cases can be further studied. Specifically, the different kinds of peaks for each class can be separated and seen.

In a second example depicted in Figure A.15, class-specific relevance-based reference samples are shown for the custom LeNet trained on Fashion-MNIST. Without specifying any further conditions, reference sample sets contain the maximally relevant samples for the observed concept selected from samples of all classes. Here, channel 1 in layer 13 (*Left column*) is used to detect thin lines and curves. Channel 14 of layer 13 is used to detect spatially extended pieces of clothing with a black line at the bottom. By conditioning reference samples towards specific classes, the use case of the concepts can be further separated. For example, channel 1 is used to detect thin pant legs of trousers or handles of a bag.

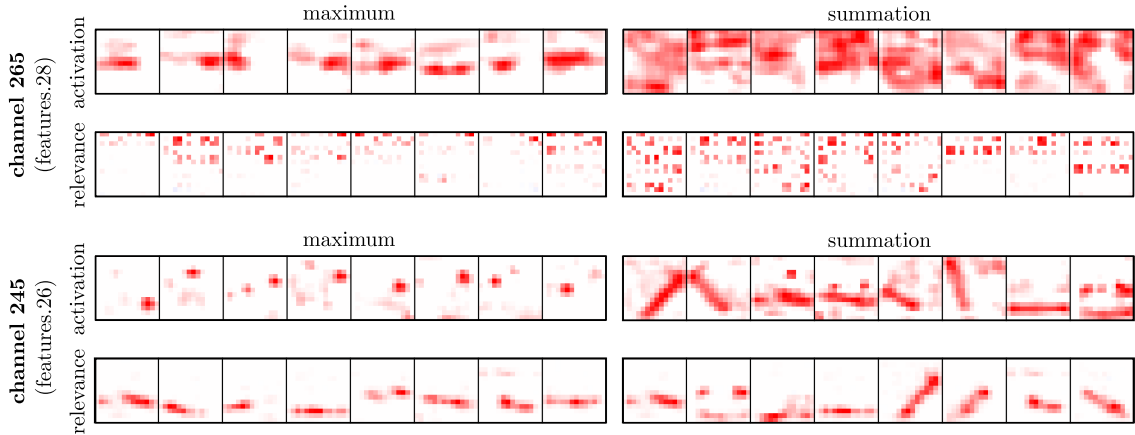


Figure A.13: Extension of Figure A.12 showing the relevance distribution inside the channel for samples collected using Relevance Maximization and the activation distribution for samples collected using Activation Maximization.

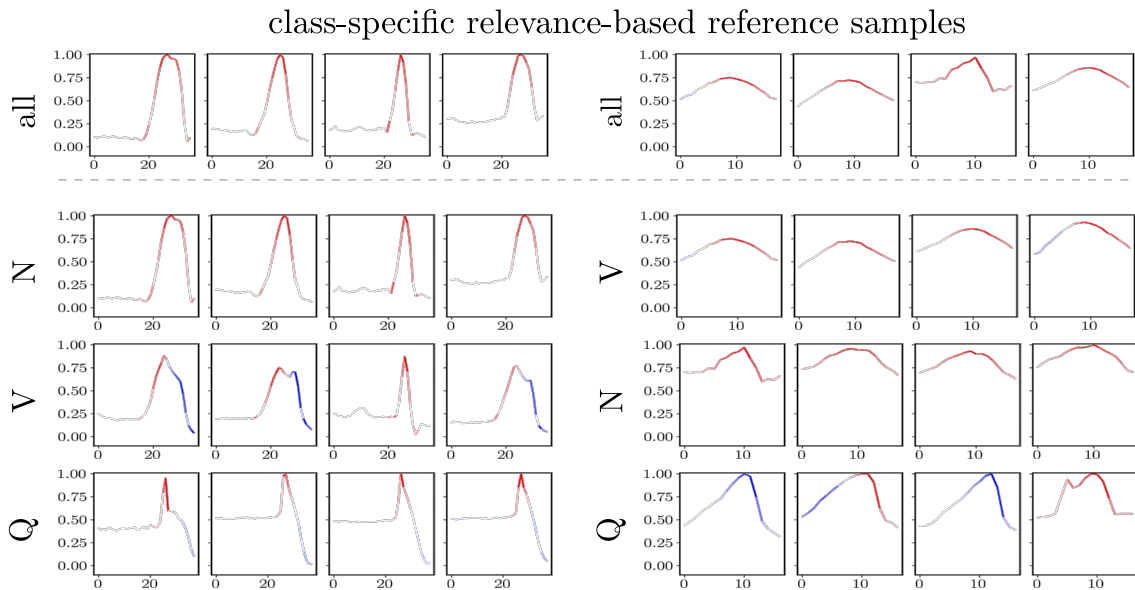


Figure A.14: Reference samples based on relevance-sorting can be conditioned on a class of interest. Shown are reference samples of channel 42 in layer `features.6` (*Left column*) and channel 23 of `features.3` (*Right column*). (*1st row*): Without specifying any further conditions, reference sample sets contain the maximally relevant samples for the observed concept selected from samples of all classes. Here, two different kinds of signal peaks are shown. Channel 42 is relevant for detecting strong peaks with a period of constant signal before. Channel 23 is relevant for peaks which already start with a signal of about 50%. (*2nd to last row*): Reference example sets of the top-3 classes (sorted descendingly) for which the analyzed concept is most relevant on average. Here, the different kinds of peaks for each class can be separated and seen. Note in (*Right column*), the first and second row show the same images. This is due to the fact, that images for category *N* have globally the highest relevance. This figure corresponds to Section 3.2.

class-specific relevance-based reference samples

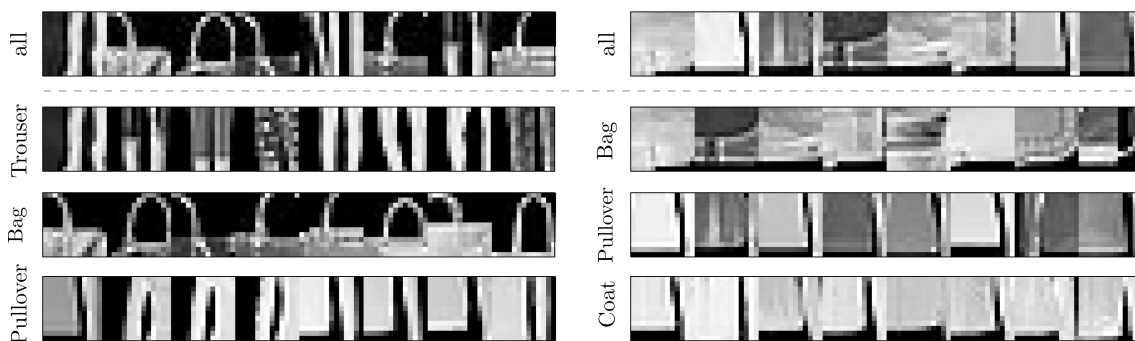


Figure A.15: Reference samples based on relevance-sorting can be conditioned on a class of interest. Shown are reference samples of channel 1 in layer 13 (*Left column*) and channel 14 of 13 (*Right column*) of a LeNet-5 model trained on Fashion-MNIST (details in A.2). (*1st row*): Without specifying any further conditions, reference sample sets contain the maximally relevant samples for the observed concept selected from samples of all classes. Here, channel 1 is used to detect thin vertical lines. Channel 14 is used to detect spatially extended pieces of clothing with a black line at the bottom. (*2nd to last row*): Reference example sets of the top-3 classes (sorted in descending order) for which the analyzed concept is most relevant on average. Here, it can be seen, how the concepts of channel 1 and 14 are used for the respective classes. For example, channel 1 is used to detect thin pant legs of trousers or handles of a bag. This figure corresponds to Section 3.2.

## A.6 Additional Results: Filter Perturbation

This section of the appendix presents additional figures and analysis for the part of our work that focuses on the interaction with the model through feature ablation. First, we will expand upon the analysis shown in Figure 19 and illustrate, how relevances are distributed among channels of the ImageNet-pretrained VGG-16 model. Secondly, interaction is presented in further detail for the model trained on the ISIC dataset.

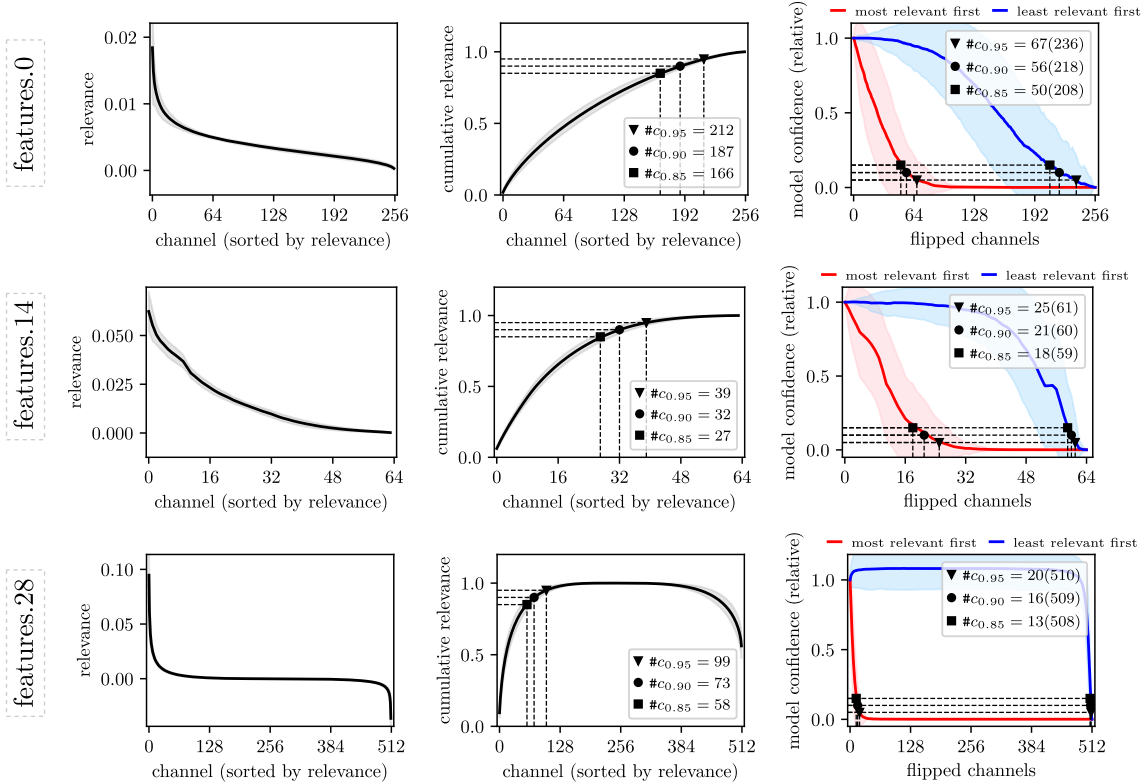


Figure A.16: Only a fraction of all 512 channels is used for classification predictions in different layers of a pretrained VGG-16 model for ImageNet. (Left): Distribution of relevance (relative to sum of positive relevances). (Center): Cumulative relevance distribution with points marked for which channel 85%, 90% and 95%, of relevance is reached, respectively. (Right): Removing (flipping) successively filters with most positive/negative relevance inside the layer. Whereas a larger number of filters are relevant for the prediction, a smaller number of the most relevant filters removed suffices to change the prediction outcome. In contrast, flipping the least relevant channels first, the model remains confident even if the majority of filters are removed. For all plots, the mean curve (of 250 samples) is displayed in opaque color and standard deviation with transparent color. The flipping experiment is restricted to confident predictions (soft-max probability above 50%) in order to limit the variation in the plot. This figure corresponds to Figure 19 in Section 4.1

Investigating individual neurons and their concepts is easiest if a small proportion of neurons are sufficient to explain most of any prediction. In Figure A.16 are the number of channels depicted, that are necessary to explain 85%, 90% or 95% of any prediction, respectively, in terms of sum of relevance and model confidence. The analysis goes beyond Figure 19 by also showing the result for earlier layers `features.0` and `features.14` besides layer `features.28`. It can be seen, that the earlier layers require a higher fraction of channels to analyze — compared to layer `features.28`. However, same as for layer `features.28`, flipping a few of the most relevant channels results in large drops regarding prediction confidence. The generally slower decay in confidence over most relevant flipped channels can be interpreted such that lower level concepts are not as class specific as more abstract representations later in the model, and as simpler features, such as edges or color gradients, are more likely to be shared among classes and exhibit a certain amount of redundancy



and replacability in the lower layers. This is also supported by the earlier confidence decay when the least relevant channels are flipped.

ResNet models have high flexibility in how they allocate concepts within the model due to their short-cut connections. As a consequence, short-cut connections cause an additional non-uniform distribution of relevance between entire layers, not just neurons. This insight is for example exploited in neural network pruning [144]. Note, that the conservation principle of LRP (cf. [11]) inherited by CRP in theory guarantees that the total amount of relevance remains constant across parallel layers. The mean relevance flow throughout the ResNet architecture is shown in Figure A.17. Here, it is visible, that several layers do not contribute strongly to predictions, as they receive low attributions. This is further confirmed by a channel flipping experiment for a layer with high relevance (`layer3.0.conv2` with a mean of over 50% relevance) and one layer with low relevance (`layer3.4.conv1` with a mean of less than 1% relevance). The flipping of channels has a significant impact for `layer3.0.conv2` on the model confidence. For layer `layer3.4.conv1` on the other hand, the confidence is less affected, resulting in a mean confidence of still over 80% after all channels are flipped.

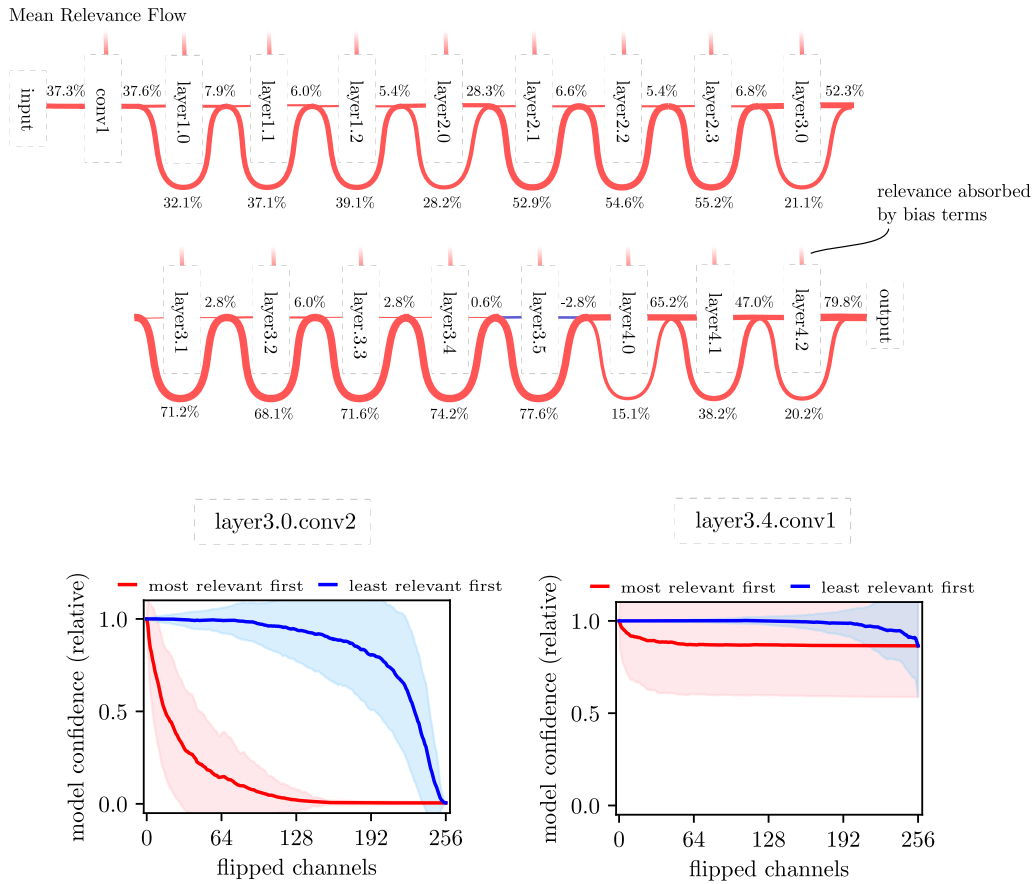


Figure A.17: The ResNet34 model is a feed-forward model with shortcut connections between layers. As is depicted in the top, layers are receiving different amount of relevances during predictions. Most layers receive less than 7% of total relevance. This result suggests, that these layers could be potentially pruned without large accuracy drops. This is further supported, by a pixel-flipping experiment (*Bottom*), showing that flipping channels has no significant impact on the prediction confidence for `layer3.4.conv1` (*Bottom Right*), which receives on average about 0.6% of total relevance. Flipping channels of layer `layer3.0.conv2` (*Bottom Left*) on the other hand has a stronger effect on the model confidence, as it also has a mean relevance of about 52% for predictions. For the plots, the mean curve (of 250 samples) is displayed in opaque color and standard deviation with transparent color. The flipping experiment is restricted to confident predictions (soft-max probability above 50%) in order to limit the variation in the plot.

## A.7 Additional Results: Feature Ablation Study

In the following, more examples are shown for the feature ablation studies of our paper. In the Sections 4.2 and 4.3, the model predictions are probed by manipulating the latent encodings activation space responsible for identified out-of-domain or Clever Hans concepts. First, more detailed experiments for the ISIC use case are shown, followed by an additional example on ImageNet.

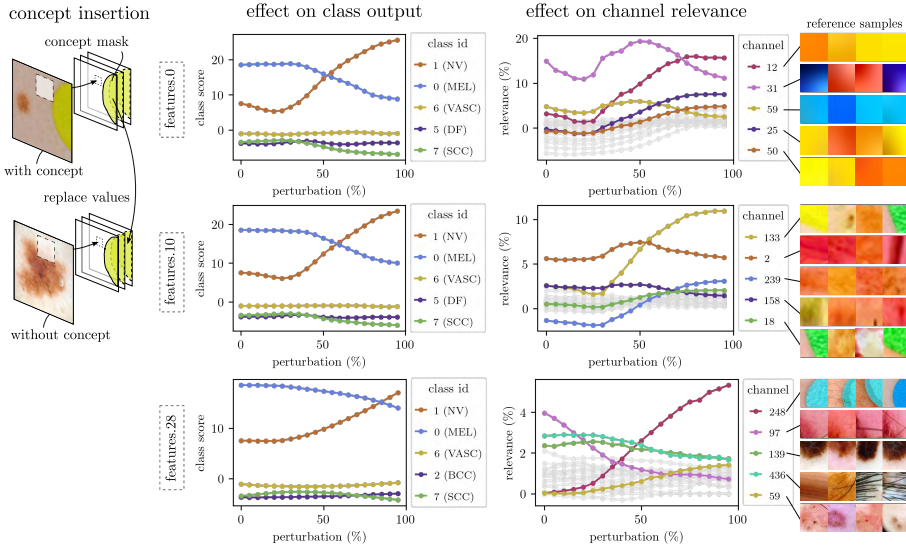


Figure A.18: Manipulating decisions by inserting concept “band-aid” for one exemplary sample at several locations: First layer `features.0` (*top*), intermediate layer `features.10` (*middle*) and higher-level layer `features.28` (*bottom*). For manipulation, the activation tensors are copied from a sample with a band-aid to a sample without band-aid. In order to only copy activations describing the band-aid concept, all activations are masked in the spatial dimension. The manipulation is performed linearly, and the change in class output as well as relevance for the top 5 decreasing/increasing channels is depicted. For each channel, the four most activating samples are shown. The closer the manipulation to the input, the stronger the change in class score. This figure corresponds to Section 4.2.

**ISIC Use Case** In the first ISIC experiment, the Clever Hans, e.g., the “band-aid” concept, is inserted into samples without band-aid. At this point, we want to show one particular sample and how the concept relevances are changing during the perturbation for different locations inside the network. As shown in Figure A.18, “band-aid” is inserted in the prediction process at several locations: first layer `features.0` (*top*), intermediate layer `features.10` (*middle*) and higher-level layer `features.28` (*bottom*). Therefore, the activation tensors are copied from a sample with a band-aid to a sample without a band-aid. In order to only copy activations describing the band-aid concept, all activations are masked to overlap with the band-aid in the spatial dimension.

Performing the perturbation linearly, the change in class output as well as relevance for the top-5 strongest changing channels is depicted in Figure A.18. Note that we report the *relative* relevance score per channel wrt. to a channel relevance sum of 100%, explaining evidence for class 1 (NV). For each channel, the four most activating samples are shown. As is visible in the plots, the insertion of the band-aid changes the prediction output from favoring class 0 to favoring class 1. The closer the manipulation to the input channel, the stronger the change in class score. This is probably the case, as it is harder to define masks and boundaries in higher levels. In higher layers, more and different interactions have taken place layer-wise in the spatial dimension. Tracking relevance values of the individual channels shows, that for each layer, channels with concepts supporting “band-aid” are growing in relevance with increasing perturbation.

In the second example, the “band-aid” concept in a sample with band-aid is replaced with band-aid by a “skin” concept from a sample solely depicting skin. The manipulation is again

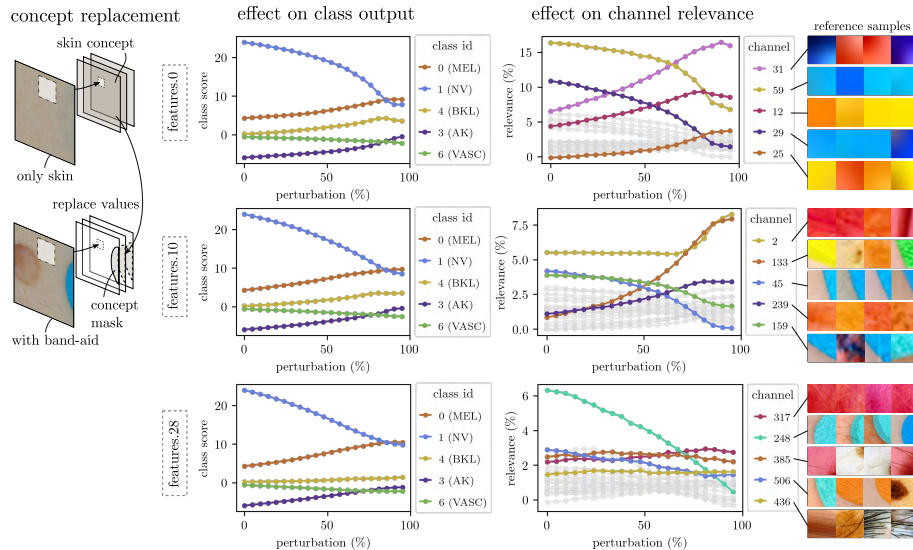


Figure A.19: Manipulating decisions by replacing concept “band-aid” with “skin” at several locations: first layer `features.0` (*top*), intermediate layer `features.10` (*middle*) and higher-level layer `features.28` (*bottom*). Therefore, the activation tensors are copied from a sample only consisting of skin to a sample with a band-aid. For the skin concept, activations are averaged over the spatial dimension and replace activations defined by a mask covering the band-aid. The manipulation is performed linearly, and the change in class output as well as relevance for the top 5 strongest changing channels is depicted. For each channel, the four most activating samples are shown. This figure corresponds to Section 4.2.

performed in the first layer `features.0`, intermediate layer `features.10` and higher-level layer `features.28`, as shown in Figure A.19. For the skin concept, activations are averaged over the spatial dimension and replace the activations defined by a mask covering the band-aid.

As is visible in the plots of Figure A.19, the replacement of the band-aid concept changes the prediction output from favoring class 1 to favoring class 0. A decrease in the score for class 1 is expected, as in the first experiment the opposite happened when concept “band-aid” is inserted. Again, the strongest change in class score is achieved by manipulating earlier layers. Investigating the change in relevance of individual channels, we can see, that channels supporting a “band-aid” concept are decreasing in relevance.

Besides showing additional individual manipulated samples, we show in Figure A.20 the band-aid insertion experiment for 160 randomly drawn samples for earlier layers, i.e. `features.0` and `features.10`. Here, a similar effect as for `features.28` can be seen: Adding the band-aid concept generally has the effect of increasing the output score of class 1. Further, channels corresponding to band-aid (e.g. in color for earlier layers or color and shape for later layers) grow in terms of relevance.

**ImageNet Use Case** In Figure A.7, we have seen, that the model uses several concepts that do not focus directly on the swimming trunks when detecting the respective class. Figure A.21 illustrates how the model confidence changes when setting these Clever Hans artifacts to zero. The filter indices of potential Clever Hans artifacts are found by applying a local analysis on the skin of the surfer. The progressive masking or deactivation of whole latent filter channels encoding bare skin quickly decreases the model’s confidence in predicting class “swimming trunks”, verifying the Clever Hans behavior and its cause.

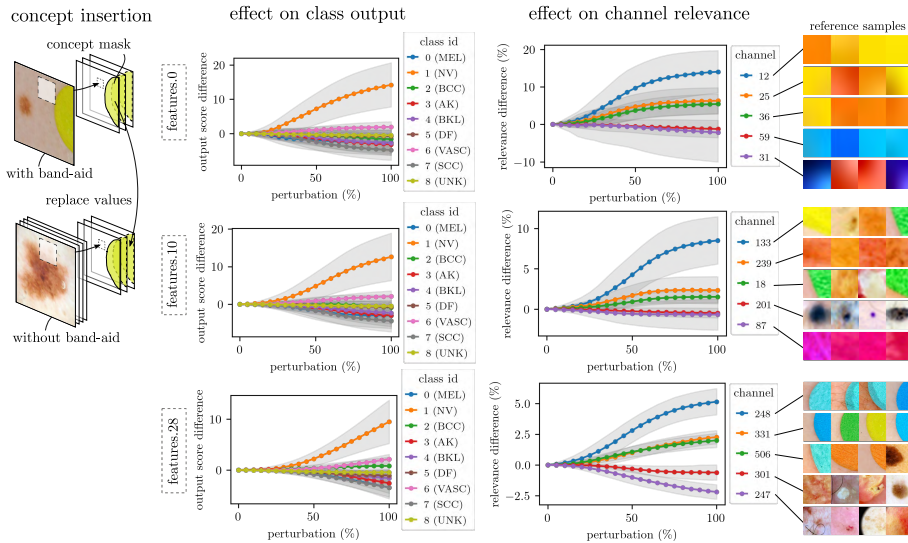


Figure A.20: Manipulating decisions by inserting concept “band-aid” into 160 randomly drawn samples. The band-aid concept is therefore inserted in the prediction process at several locations: first layer `features.0` (*top*), middle layer `features.10` (*middle*) and higher-layer `features.28` (*bottom*). Therefore, the activation tensors are copied from a sample with a band-aid to a sample without band-aid. In order to only copy activations describing the band-aid concept, all activations are masked in the spatial dimension. The manipulation/perturbation is done linearly, and the change in class output for the top 8 classes is depicted on the right. Adding a band-aid generally has the effect of increasing the output score of class 1. Regarding the concepts, it can be seen that channels corresponding to band-aid (e.g. in color for earlier layers or color and shape for later layers) grow in terms of relevance. The standard deviation is highlighted in light-gray color. This figure corresponds to Section 4.2.

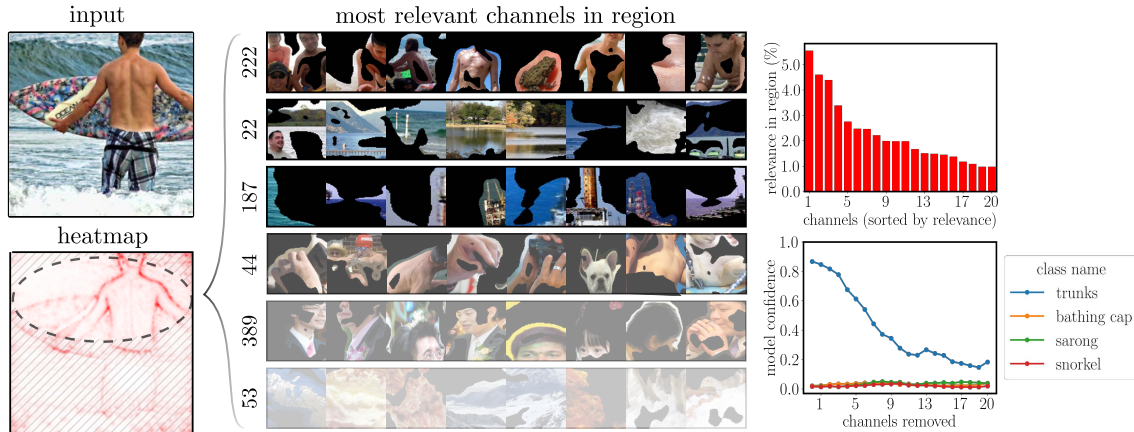


Figure A.21: Feature ablation experiment for the swimming trunk classification shown in Figure A.7. Local analysis of the attribution map reveals several channels (222, 22, 187, 44, 389, 53 and more) in layer `features.28` of a VGG-16 model pretrained on ImageNet that encode for several Clever Hans features exploited by the model to detect the “swimming trunks” class. (*Left*): Input image and heatmap. (*Center*): Reference samples  $\mathcal{X}_{8 \text{ sum}}^{* \text{rel}}$  for the 6 most relevant channels in the selected region in descending order of their relevance contribution. (*Right*): Relevance contribution of 20 most relevant filters inside the region. These filters are successively set to zero and the change in prediction confidence of different classes is recorded. This figure corresponds to Section 4.3.

## A.8 Additional Results: Explanation-based Image Retrieval

In Section 4.3, we have shown that several filters of a VGG-16 BN model are used to detect a watermark sign in images. The filters' function is revealed by investigating their corresponding most relevant reference samples. For further information, the most *activating* samples (ActMax) of the discussed filters are shown in Figure A.22. It is to note, that regarding the most activating samples, no indication of a behavior regarding watermark signs is visible, other than in the RelMax-based examples shown in Figure 22.

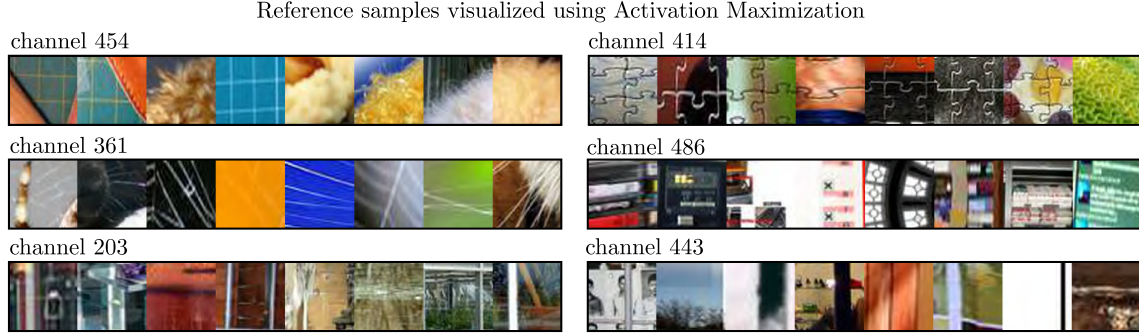


Figure A.22: Reference samples  $\mathcal{X}_{\text{sum}}^{\text{act}}$  for the six most important filters activating on the watermark of the *safe* class discussed in Section 4.3. It is to note, that regarding the most activating samples, no indication of a behavior regarding watermark signs is visible.

## A.9 Additional Results: Assessing Concept Similarity

In Section 4.4, we have shown, that channels with similar concepts form clusters based on the symmetric cosine similarity of their activations, which can be visualized and identified using the t-SNE algorithm.

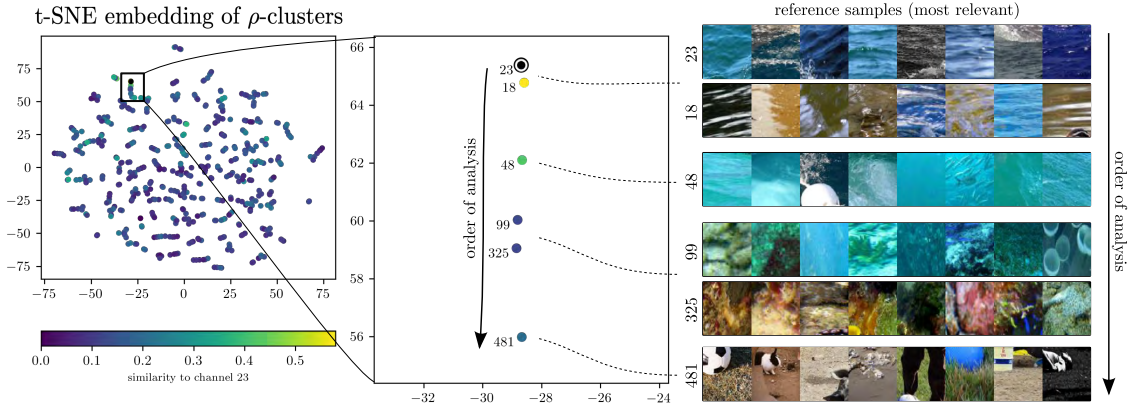


Figure A.23: Channels can be clustered using the symmetric cosine similarity, and visualized using the t-SNE algorithm. (*Left*): Several clusters can be found when layer `features.40` of a VGG-16 with BatchNorm layers trained on ImageNet is analyzed, indicating many distinct groups of simultaneously firing sets of neurons. (*Right*): One particular cluster forming a line in the embedded space is shown in more detail with a total of six channels and their reference images obtained via RelMax. As is visible from the reference images, the over-all concept of the cluster is related to *water*. Starting with channels 23 and 18, which are relevant for waves on the water surface. The next similar channel is channel 48 activating for turquoise water above and below the surface. Thereafter, channel 99 and 325 are characterized by concepts describing corals and stones underwater. Eventually, channel 481 is used for grass and sand textures. This example illustrates how a similarly activating filters may span semantically related topics, and semantic transitions are seemingly possible in related filter sets.

In Figure 24, we have qualitatively investigated the similarity of concepts in the embedded space, as represented by their RelMax-based reference examples. An additional t-SNE cluster example is shown in Figure A.23, similar to Figure 24. Specifically, a total six channels forming a chain in the embedding space are displayed with their most relevant reference samples. Starting with channel 23 relevant for waves on the water surface seen from above, the next similar channel is channel 18 activating for a similar concept with differently colored water. Channel 48 corresponds to turquoise water above and below the surface. Thereafter, channel 99 and 325 are characterized by concepts describing corals and stones underwater. Eventually, channel 481 is used for grass and sand textures. This example illustrates how a semantic transition in terms of concepts can be seen discovered when analyzing the activations of latent neurons based on RelMax reference examples.

Another example of finding channels with similar concepts using t-SNE is shown in Figure A.24, where four channels can be found that are relevant for the recognition of legs of dogs and other animals (and objects). Here, the embedding allows splitting the space into several subspaces: Channels 328 and 282 are relevant for “bright-colored fur”, whereas channels 139 and 359 for “darker-colored fur”. On the other hand, channels 139 and 328 react for “long-haired fur” and channels 359 and 282 for “short-haired fur”. We might have identified a group of channels encoding the common concept of “legs” with degrees of freedom with regard to brightness and “leg volume”. How these similar channels are differently used in predictions is shown in Figure A.25.

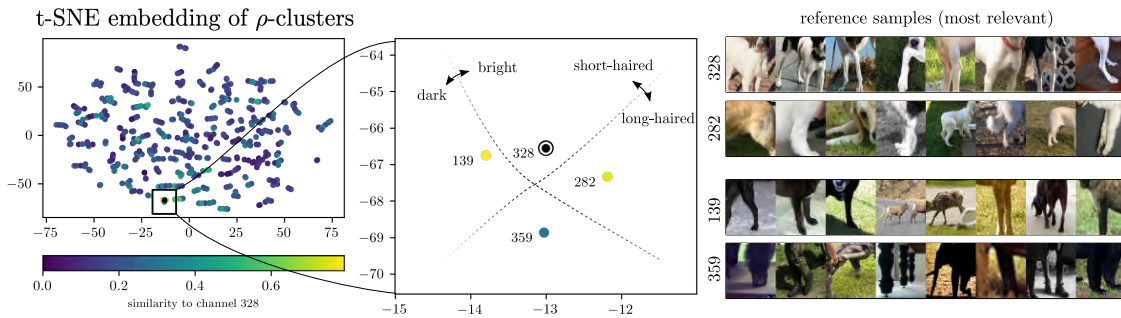


Figure A.24: Channels can be clustered based on their symmetrized cosine similarity using the t-SNE algorithm as described in Section 4.4. (*Left*): Several clusters can be found when layer `features.40` of a VGG-16 with BatchNorm layers trained on ImageNet is analyzed. (*Right*): One particular cluster around channel 328 is shown in more detail with a total of four channels and their reference images obtained via RelMax. As is visible from the reference images, the over-all concept of the cluster is related to “dog legs”. Here, the embedding allows splitting the space into several subspaces: Channels 328 and 282 are relevant for “bright-colored fur”, whereas channels 139 and 359 for “darker-colored fur”. On the other hand, channels 139 and 328 react for “long-haired fur” and channels 359 and 282 for “short-haired fur”.

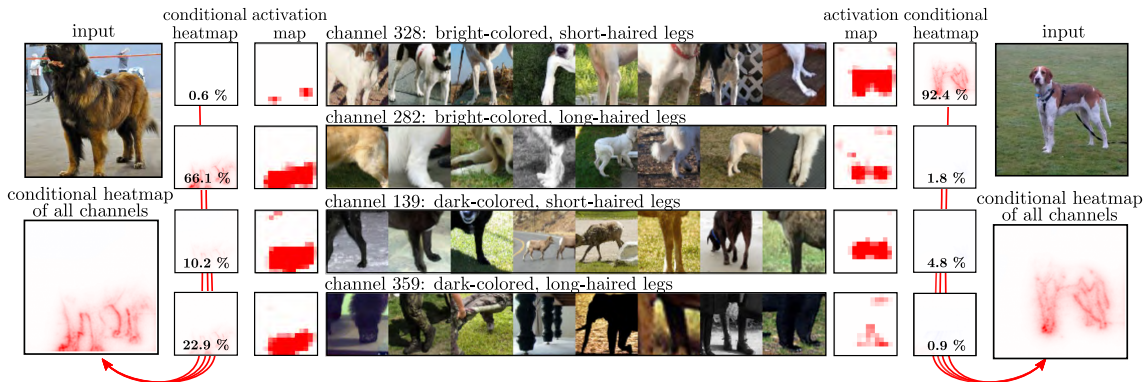


Figure A.25: Several similar filters in layer `features.40` of a VGG-16 BN model trained on *ImageNet* have high symmetrized cosine similarity (see Figure A.24), but are used differently by the model during predictions. These presented filters commonly activate for different kind of dog legs, as is visible on the conditional heatmaps as well as channel maps. Their different function is illustrated by the prediction of two different dog samples. (*Left*): Channels 282 and 259 are strongly used to predict a brown-colored and long-haired dog, as relative relevance scores show. (*Right*): For the other example, channel 328 is strongly used for classifying a short-haired dog. This figure corresponds to Figure 26 in Section 4.4.